



저작자표시-비영리-변경금지 2.0 대한민국

이용자는 아래의 조건을 따르는 경우에 한하여 자유롭게

- 이 저작물을 복제, 배포, 전송, 전시, 공연 및 방송할 수 있습니다.

다음과 같은 조건을 따라야 합니다:



저작자표시. 귀하는 원저작자를 표시하여야 합니다.



비영리. 귀하는 이 저작물을 영리 목적으로 이용할 수 없습니다.



변경금지. 귀하는 이 저작물을 개작, 변형 또는 가공할 수 없습니다.

- 귀하는, 이 저작물의 재이용이나 배포의 경우, 이 저작물에 적용된 이용허락조건을 명확하게 나타내어야 합니다.
- 저작권자로부터 별도의 허가를 받으면 이러한 조건들은 적용되지 않습니다.

저작권법에 따른 이용자의 권리는 위의 내용에 의하여 영향을 받지 않습니다.

이것은 [이용허락규약\(Legal Code\)](#)을 이해하기 쉽게 요약한 것입니다.

[Disclaimer](#)

공학박사학위논문

Fast Time-resolved X-ray Diagnostics for SNU X-pinch

SNU X-pinch를 위한 초고속 엑스선 진단계

2022 년 8 월

서울대학교 대학원

에너지시스템공학부

함 승 기

Fast Time-resolved X-ray Diagnostics for SNU X-pinch

지도 교수 정 경 재

이 논문을 공학박사 학위논문으로 제출함
2022 년 7 월

서울대학교 대학원
에너지시스템공학부
함 승 기

함승기의 공학박사 학위논문을 인준함
2022 년 7 월

위 원 장 _____ 황 용 석 (인)

부위원장 _____ 정 경 재 (인)

위 원 _____ 나 용 수 (인)

위 원 _____ 김 영 철 (인)

위 원 _____ 김 덕 규 (인)

Abstract

Fast Time-resolved X-ray Diagnostics for SNU X-pinch

Seunggi Ham

Department of Energy System Engineering

The Graduate School

Seoul National University

An X-pinch has outstanding advantages as an x-ray source for high temporal and spatial resolutions thanks to its unique characteristics of the hot spot formed at a fixed point. According to conventional X-pinch studies, to emit intense x-ray pulses with low emission time, its current generator should meet a current rise rate of more than 1 kA/ns. However, several studies have confirmed that a slow X-pinch with a current rise rate of less than 1 kA/ns can produce narrow and intense x-ray pulses. Slow X-pinch has advantages as a portable laboratory-scale soft x-ray (SXR) source compared to the conventional X-pinch using a bulky and expensive current generator in that it uses a capacitor bank with a relatively small size, low cost, and simple structure. On the other hand, a slow X-pinch has disadvantages such as more frequent multi bursts, longer x-ray emission time, and larger jitter. An analysis of the x-ray peaks and the X-pinch plasma conditions is needed to improve

these disadvantages. Thus, a filtered absolute extreme ultraviolet (AXUV) diode array is developed, suitable for analyzing multi bursts of the slow X-pinch with an x-ray emission time of about tens to hundreds of ns and a large time jitter. In addition, x-ray spectra are analyzed by FLYCHK code and a plasma parameter estimation for Cu wires X-pinch is attempted. In particular, late-time x-ray peaks contributing to the increase in multi bursts and x-ray emission time are analyzed.

The filtered AXUV diode array is designed to measure the time evolution of the x-ray spectrum in an energy range of 1–10 keV. AXUV-HS5, the detector, has a fast rise time of 0.7 ns, a wide energy detection range, and high accessibility. We use the least-squares (LS) method that reconstructs a discrete spectrum with low spectral resolution directly from virtual channels (VCs). Geant4 simulation is utilized to design an appropriate filter set for flat-and-sharp VCs, where a filter with no spectral edge removes large tails of the response curves. Furthermore, the performance evaluation of VCs is conducted through the reconstruction of reference spectra formed by Geant4 simulation. As a result, it is confirmed that the filtered AXUV diode array reconstructs the x-ray spectrum with an average error of less than 10%.

Plasma parameters can be obtained through x-ray spectrum analysis because plasmas with different parameters emit different x-ray spectra. The FLYCHK code is utilized to obtain synthetic spectra as a spectroscopic modeling tool. Synthetic spectra of Cu plasma with different electron temperatures, electron densities, and fast electron

fractions are calculated by the FLYCHK code; three spectral ranges containing different Cu line radiations and varying differently with each parameter are specified by analyzing the spectra. For quantitative comparison with the measured spectrum, two x-ray power ratios with the spectral ranges are calculated from the synthetic spectra.

25 μm -thick Cu wires X-pinch experiments are conducted on SNU X-pinch with charging voltages of 50 and 55 kV. Three kinds of x-ray bursts are observed and plasma parameter analysis is performed on them. The first burst shows similar characteristics to those observed in the conventional X-pinch. Thermal radiations by HS are observed at the first set and their electron density and electron temperature are estimated to be around 10^{23} cm^{-3} and 1 keV, respectively. At a charging voltage of 55 kV, an x-ray peak by the short electron beam is observed, and the fast electron fraction rises to about 20%. The second and third bursts are both generated by the interaction between cold plasmas and long electron beams. In the second burst, the formation of electron beams is accompanied by an increase in electron density and it is similar to that of HS. While in the third burst, there is no increase in the bulk plasma parameters and the electron density is much lower than that of the second burst. Additionally, thicker Cu wires X-pinch experiments are conducted and the results are compared. As Cu wires become thicker, HS parameters and long electron beam generated x-ray bursts decrease, and pinch times are delayed; 40 μm -thick Cu wires X-pinch release a single x-ray peak.

The use of an insulated wire load also suppresses the emission of x-rays by the long electron beam. The insulated Cu wires X-pinch produce a single intense x-ray peak from which we estimate similar electron density and electron temperature with those of the 25 μm -thick Cu wires X-pinch; multi bursts and emission of HXR are reduced by using the insulated Cu wires load. The results of bare and insulated Cu wires X-pinch are compared. As a result, the generation of x-ray burst by a long electron beam is expected to be related to the pinch time rather than the HS formation process. Furthermore, based on the experimental results and previous studies, we present a possible scenario for the increase of electron density by long electron beams, which involves additional ionization of plasmas by high-energy electron beams and current reconnection.

This study confirms that the generation of long electron beams plays an important role in the x-ray emission of slow X-pinch; thus, its dynamics study will provide clues to the improvement of the slow X-pinch. Accordingly, we suggest the collimated x-ray diode, x-ray and optical imaging system, optical voltage and current sensors as diagnostics for further research. Research using the additional diagnostics is expected to present a new factor for the optimization of slow X-pinch.

Keyword : High-energy-density plasma, x-ray source, slow X-pinch, fast-time resolved x-ray diagnostics, plasma parameter estimation, electron beam.

Student Number : 2016-21312

Table of Contents

Abstract	i
Table of Contents	v
List of Figures.....	vii
List of Tables	xvi
Chapter 1. Introduction.....	1
1.1. X–pinch	1
1.2. Time–resolved x–ray spectroscopy for slow X–pinch	5
1.3. Previous works and Motivation.....	9
Chapter 2. SNU X–pinch.....	1 2
2.1. SNU X–pinch.....	1 2
2.2. Pulse generator	1 5
Chapter 3. Development of fast time–resolved x–ray diagnostics.....	1 8
3.1. Development of a filtered AXUV diode array	1 8
3.1.1. Ten–channel filtered AXUV diode array.....	1 8
3.1.2. LS method	2 1
3.1.3. Filter set design using Geant4 simulation	2 2
3.1.4. Compensation factors	2 8
3.1.5. Test cases by Geant4 simulation	3 1

3.2. Plasma parameter estimation method	3 5
3.2.1. Cu plasma emitted x-ray spectrum analysis by FLYCHK code and x-ray power ratios	3 5
3.2.2. X-ray power ratios with fast electrons	4 3
3.2.3. Plasma parameter estimation and the process of analyzing x-ray data	5 6
Chapter 4. Time-resolved x-ray spectrum measurement.....	6 1
4.1. Two copper wires slow X-pinch	6 1
4.1.1. The results of the first burst.....	6 5
4.1.2. The results of the second burst	7 1
4.1.3. The results of the third burst.....	7 5
4.2. Thicker Cu wires slow X-pinch	8 2
4.3. Insulated Cu wires X-pinch.....	8 8
4.4. Summary and Discussion	9 2
Chapter 5. Conclusions and Future work.....	9 8
5.1. Conclusions.....	9 8
5.2. Future work	1 0 1
Bibliography	1 0 4
Abstract in Korean	1 1 1

List of Figures

Figure 2.1 (a) The schematic view of the SNU X–pinch, (b) Capacitor bank of the SNU X–pinch [43]	1 3
Figure 2.2 (a) Side view and (b) top view of the chamber of the SNU X–pinch and 10–channel filtered AXUV diode array in the chamber. Two diode arrays are installed in two opposite ports at a distance of 464.8mm from the crossing point of the wires. (c) Each module of the array is arranged at an angle to focus on the crossing point.....	1 4
Figure 2.3 The results of short circuit test. Black, red, and blue lines are generated currents with charging voltages of 50, 55, and 60 kV, respectively.	1 6
Figure 3.1 a) AXUV–HS5 and (b) aluminum casing for half of the AXUV diode array. The width and length of AXUV–HS5 are 9.5 and 22.12 mm, respectively, and the active area is 1 mm ² . The aluminum casing consists of five modules, each containing a set of AXUV–HS5 and filters. Two aluminum casings are built; their size is 100 × 20 mm ²	2 0
Figure 3.2 Setup of Geant4 simulations for filter set design. Vacuum, window, filters, and AXUV–HS5 are included in the setup. A square–shaped x–ray beam, uniformly distributed from 0.02 to 20 keV, is simulated to obtain response curves.	2 3
Figure 3.3 Response curve of AXUV–HS5 obtained by Geant4	

simulations. The response curve is matched with the known AXUV-HS5 response curve.	2 3
Figure 3.4 Response curves of the channels. Channel 1 (yellow area) has no spectral edge. The other channels divide the energy range for nine VCs.	2 6
Figure 3.5 (a) VCs without a continuum channel and (b) VCs with a continuum channel (channel 1). Without a continuum channel, there are problems with formatting VCs 1 and 5.	2 7
Figure 3.6 Two major defects of VCs. The first defect is low sensitivity (magenta) and the second defect is sensitivity out of the VC (yellow). E_H and E_L are the maximum and minimum energy of reconstruction, respectively. $E_{\min,n}$ and $E_{\max,n}$ are the maximum and minimum energy of the n -th virtual channel, respectively. ΔE_n is its interval.	2 9
Figure 3.7 Compensated VCs. The n -th virtual channel is compensated by the first compensation factor ($w_{1,n}$). ...	3 0
Figure 3.8 Reconstruction results of the LS method. (a) Uniform spectrum, (b) 1 keV blackbody radiation spectrum, (c) 1.5 keV blackbody radiation spectrum, and (d) 1.5 keV blackbody radiation spectrum with a Gaussian peak at 8 keV. Blue line, input spectrum; blue dashed line, histogram of the input spectrum. Black line, reconstruction results of the VCs; red line, reconstruction results of compensated VCs. Black and red dashed lines with square symbols, channel errors of reconstruction results of VCs and	

compensated VCs, respectively.....	3 3
Figure 3.9 Eight VCs. VCs 1 and 2 are combined into the first channel of eight VCs.....	3 4
Figure 3.10 Reconstruction results of a 1.5 keV blackbody radiation spectrum with a Gaussian peak at 8 keV by new eight VCs. The errors of the eight VCs are less than 10% and much smaller than the error of VC ₁	3 4
Figure 3.11 Opacity spectra of Cu plasma with an electron temperature of 1.0 keV and an electron density of $4.642 \times 10^{22} \text{ cm}^{-3}$ produced by FLYCHK (black) and ATOMIC (red) codes.....	3 6
Figure 3.12 Synthetic spectra with electron temperatures of 0.8 (black) and 1.5 keV (red) and an electron density of 10^{21} cm^{-3}	3 9
Figure 3.13 Synthetic spectra with electron densities of 10^{21} (black) and 10^{23} cm^{-3} (red) and an electron temperature of 0.8 keV	3 9
Figure 3.14 The x-ray power ratios with different electron temperatures and electron densities obtained from the FLYCHK code. (a) and (b) are the first and second ratios	4 2
Figure 3.15 Synthetic spectra with different characteristic energies of 10 (red), 20 (blue), and 30 (magenta) keV. (a) to (c) show the spectra with different electron temperatures, electron densities, and fast electron fractions, and represent ones of HS plasma.	4 4

Figure 3.16 Synthetic spectra with different characteristic energies of 10 (red), 20 (blue), and 30 (magenta) keV. (a) to (c) show the spectra with different electron temperatures, electron densities, and fast electron fractions.....	4 4
Figure 3.17 Synthetic spectra with the fast electron fractions of 0% (black) and 5% (red). An electron temperature is 0.8 keV and electron density is 10^{21} cm^{-3}	4 5
Figure 3.18 The x-ray power ratios with a fast electron fraction of 1% obtained from the FLYCHK code. (a) and (b) are the first and second ratios.	4 7
Figure 3.19 The x-ray power ratios with a fast electron fraction of 5% obtained from the FLYCHK code. (a) and (b) are the first and second ratios.	4 8
Figure 3.20 The x-ray power ratios with a fast electron fraction of 12% obtained from the FLYCHK code. (a) and (b) are the first and second ratios.	4 9
Figure 3.21 The x-ray power ratios with a fast electron fraction of 30% obtained from the FLYCHK code. (a) and (b) are the first and second ratios.	5 0
Figure 3.22 Synthetic spectra with the fast electron fractions of (a) 1% and (b) 5%. A electron density is 10^{18} cm^{-3} and electron temperatures are 0.1 (black line), 0.2 (red line), 0.5 (orange line), and 1.0 keV (green line).....	5 2
Figure 3.23 Synthetic spectra with electron densities of (a) 10^{21} cm^{-3} and (b) 10^{23} cm^{-3} . Fast electron fraction is 1% and electron temperatures are 0.1 (black line), 0.2 (red	

line), 0.5 (orange line), and 1.0 keV (green line).....	5 4
Figure 3.24 Synthetic spectra with an electron density of 10^{23} cm^{-3} . Fast electron fraction is 5% and electron temperatures are 0.1 (black line), 0.2 (red line), 0.5 (orange line), and 1.0 keV (green line).....	5 5
Figure 3.25 Reconstructed (solid) and synthetic spectra (dotted) with various plasma parameters. (a) electron temperatures are 1.0 (black) and 1.5 keV (red) with an electron density of 10^{23} cm^{-3} , (b) electron densities are 10^{22} cm^{-3} (black) and 10^{23} cm^{-3} (red) with electron temperature of 1.5 keV, (c) electron densities and temperatures of 10^{22} cm^{-3} and 0.1 keV (black) and 10^{23} cm^{-3} and 1.0 keV (red) with fast electron fraction of 1%, (d) electron temperatures and fast electron fractions of 0.1 keV and 30% (black) and 1.0 keV and 20% (red) with an electron density of 10^{23} cm^{-3}	5 9
Figure 3.26 A schematic diagram of the process of analyzing x-ray data.....	6 0
Figure 4.1 Typical x-ray signals of two Cu wires X-pinches with charging voltages of (a) 50 and (b) 55 kV. The yellow areas indicate ranges of three bursts of x-rays, (1), (2), and (3).....	6 2
Figure 4.2 An example of a comparison of the x-ray power ratios from the first peak of 50 kV case. (a) and (b) show plasma parameters of the first and the second ratios with errors less than 10%, respectively.	6 4

Figure 4.3 An example of a comparison of the x-ray power ratios from the first peak of 50 kV case. It shows plasma parameters with averaged errors of the x-ray power ratios less than 10%.....	6 4
Figure 4.4 The signals of channels 1, 2, and 10 and the time evolution of estimated electron densities, electron temperatures, and fast electron fractions for the first burst of the 50 kV case. Estimated plasma parameters of three x-ray peaks from peak-integrated x-ray powers are plotted together.	6 7
Figure 4.5 The signals of channels 1, 2, and 10 and the time evolution of estimated electron densities, electron temperatures, and fast electron fractions for the first burst of the 55 kV case. Estimated plasma parameters of two x-ray peaks from peak-integrated x-ray powers are plotted together.	6 9
Figure 4.6 The signals of channels 1, 2, and 10 and the time evolution of estimated electron densities, electron temperatures, fast electron fractions, and electron beam densities for the second burst of the 50 kV case.	7 3
Figure 4.7 The signals of channels 1, 2, and 10 and the time evolution of estimated electron densities, electron temperatures, fast electron fractions, and electron beam densities for the second burst of the 55 kV case.	7 4
Figure 4.8 The signals of channels 1, 2, and 10 and the time evolution of estimated electron densities, electron temperatures,	

fast electron fractions, and electron beam densities for the third burst of the 50 kV case.	7 7
Figure 4.9 The signals of channels 1, 2, and 10 and the time evolution of estimated electron densities, electron temperatures, fast electron fractions, and electron beam densities for the third burst of the 55 kV case.	7 8
Figure 4.10 An example of a comparison of the x-ray power ratios from the second burst of 50 kV case. (a) and (b) show plasma parameters of the first and the second ratios with errors less than 15%, respectively.	7 9
Figure 4.11 An example of a comparison of the x-ray power ratios from the second burst of 50 kV case. It shows plasma parameters with averaged errors of the x-ray power ratios less than 15%.	7 9
Figure 4.12 An example of a comparison of the x-ray power ratios from the third burst of 50 kV case. (a) and (b) show plasma parameters of the first and the second ratios with errors less than 15%, respectively.	8 0
Figure 4.13 An example of a comparison of the x-ray power ratios from the third burst of 50 kV case. It shows plasma parameters with averaged errors of the x-ray power ratios less than 15%.	8 0
Figure 4.14 Typical x-ray signals of two (a) 30 and (b) 40 μm - thick Cu wires X-pinch with a charging voltage of 55 kV	8 2
Figure 4.15 The signals of channels 1, 2, and 10 and the time	

evolution of estimated electron densities, electron temperatures, and fast electron fractions for the first burst of the 30 μm -thick Cu wires X-pinch. Estimated plasma parameters of two x-ray peaks from peak-integrated x-ray powers are plotted together	8 4
Figure 4.16 The signals of channels 1, 2, and 10 and the time evolution of estimated electron densities, electron temperatures, fast electron fractions, and electron beam densities for the second burst of the 30 μm -thick Cu wires X-pinch.....	8 5
Figure 4.17 The signals of channels 1, 2, and 10 and the time evolution of estimated electron densities, electron temperatures, and fast electron fractions for the first burst of the 40 μm -thick Cu wires X-pinch. Estimated plasma parameters of two x-ray peaks from peak-integrated x-ray powers are plotted together	8 7
Figure 4.18 Typical x-ray signals of the two insulated Cu wires X-pinch with a charging voltage of 55 kV. The yellow area indicates a range of the first burst.	9 0
Figure 4.19 The signals of channels 1, 2, and 10 and the time evolution of estimated electron densities, electron temperatures, and fast electron fractions for the first burst of the insulated Cu wires X-pinch. Estimated plasma parameters of the x-ray peak from peak-integrated x-ray powers are plotted together.	9 1

Figure 4.20 Current signals of the 50 (black line) and 55 kV (red line) charging voltage cases. Dash and solid arrows mark the second and the third bursts of the 50 and 55 kV cases, respectively.....	9 7
Figure 5.1 Schematic view of a configuration of diagnostics for future work	1 0 3

List of Tables

Table 1.1 Researches of the slow X-pinch and diagnostics	8
Table 2.1 Specifications of pulse generators of SNU X-pinch and other slow X-pinchs	1 7
Table 3.1 Filter material and its spectral band edge of each channel.	2 6
Table 4.1 Estimated electron densities, electron temperatures, and fast electron fractions of the first bursts of the 50 kV and the 55 kV cases.....	6 5
Table 4.2 Estimated electron densities, electron temperatures, and fast electron fractions from peak-integrated x-ray powers of the first burst of 50 kV case.....	6 6
Table 4.3 Estimated electron densities, electron temperatures, and fast electron fractions from peak-integrated x-ray powers of the first bursts of the 55 kV case	7 0
Table 4.4 Emission time, estimated electron densities, electron temperatures, electron beam densities, and fast electron fractions of the second bursts of the 50 kV and the 55 kV cases.....	7 2
Table 4.5 Emission time, estimated electron densities, electron temperatures, electron beam densities, and fast electron fractions of the third bursts of the 50 kV and the 55 kV cases.....	7 6
Table 4.6 HS parameters, pinch times, and kinds of x-ray bursts	

from different Cu wire loads with the charging voltage of 55 kV.....	9 5
Table 5.1 Conversion efficiencies from a total input energy to x-ray energy with different energy ranges.....	1 0 0

Chapter 1. Introduction

1.1. X-pinch

An X-pinch is a pulsed power device consisting of two or more fine wires crossed at a point and a fast-rise high current generator. The X-pinch has been studied for research on high-energy-density plasma and as a source of intense x-rays. The general process of the X-pinch is as follows. By fast-rise high current flowing to the wires placed between electrodes, wire materials are ablated and form corona plasmas. At the wire crossing point where the current in each wire is merged, the plasmas are pinched inward by strong $J \times B$ force, forming a neck structure. In the neck structure, an ultra-small high-density plasma called hot spot (HS) is formed by the sausage instability, which is referred to as “HS formation phase” in this paper. At the HS formation phase, the HS emits short-lived, powerful soft x-ray (SXR) radiation. The SXR from the X-pinch is spatially localized at a micrometer scale and has a short emission time of nanosecond scale.[1–5] In addition to the thermal radiation by HS, x-rays are emitted by fast electrons (so-called electron beam) in the X-pinch.[6–11] Fast electrons are accelerated by the induced electric field after the formation of HS and disruption of the neck, so-called “neck disruption phase”. The fast electrons are produced after 1–2 ns from the HS burst and maintained for 1–2 ns in the 0.1–1 mm region. In addition, electron beams are also formed by an electric field between plasma electrodes (minidiodes) after the neck

structure is depleted (“minidiode depletion phase”). At the minidiode depletion phase, electron beams are formed in several ns to several tens of ns and maintained for a much longer time in the several mm region. The two kinds of electron beams were introduced as “short electron beam” and “long electron beam” in the previous study [6], respectively. Characteristic lines are radiated by an interaction between electron beams and dense plasma electrodes and bremsstrahlung continuum radiations are also emitted by electron beams.[1, 6–8]

The X-pinch has strength over other point SXR sources thanks to its fixed hot spot position. These characteristics make X-pinch an excellent SXR source for point projection radiography to study biological objects and rapidly varying objects such as high-energy-density plasma.[12, 13] On the other hand, generally two or four wires X-pinch had several problems as an SXR source such as x-ray timing jitter, multi burst, and electron beam generated x-rays, etc. Thus, several studies about various load configurations have been conducted to improve the problems and obtain a specific x-ray spectrum.[1, 5, 14] However, the electron beam-generated x-rays can also be utilized as a hard x-ray (HXR) source for applications that require energetic x-rays.[13]

Previous studies on the X-pinch have suggested that a current rise rate of $> 1 \text{ kA/ns}$ is required to form HS and emit strong and narrow x-ray pulses. Therefore, to satisfy this condition, bulky and expensive pulse generators such as Marx generators and pulse forming lines have been used mainly. On the contrary, several

research institutes[15–21] have reported that short-lived x-rays are also produced at X-pinchs with a slow current rise rate of < 1 kA/ns (so-called slow X-pinch). Most slow X-pinchs use a capacitor bank composed of low inductance capacitors as a current generator. Because the capacitor bank features a small size, low cost, and simple structure, the slow X-pinch has advantages over conventional X-pinch as a compact x-ray source. Despite its relatively low power, it produced a strong soft x-ray. It also emits less HXR than a conventional X-pinch, which is an advantage as an SXR source. It has the disadvantage of a relatively long x-ray emission time of tens to hundreds of nanoseconds, large time jitter of a hundred nanoseconds, and large variation of x-ray energy. However, except for applications that require extremely high temporal resolution, it is valuable as a portable SXR source. [15–21]

Several studies have been conducted on the slow X-pinch with the various research subject, as shown in Table. 1.1. Diagnostics used in the studies include an optical camera, schlieren, shadowgraphy, interferometer, x-ray diode (XRD), diamond photo-conducting detector, x-ray pinhole camera, and time-integrated flat crystal spectrograph. The studies have found that the general dynamics of the slow X-pinch are similar to those of conventional X-pinchs; however, there are differences in x-ray emission characteristics, such as longer x-ray emission time and more frequent multi bursts.[15–21] Currently, little research has been conducted on why multi bursts are emitted in the slow X-pinch and what properties the plasmas that emit multi bursts have. In particular,

there is a lack of analysis of late-time x-ray peaks assumed to be emitted by electron beams. These questions are important in studying the dynamics of the slow X-pinch and improving its weaknesses.

1.2. Time-resolved x-ray spectroscopy for slow X-pinch

To analyze x-ray peaks of the slow X-pinch, it is important to measure the properties of plasmas emitting x-rays; x-ray spectroscopy is a notable way to measure X-pinch plasma parameters.[22] However, previous studies have focused on X-pinch images and XRD signals. Although there is a result measured by time-integrated x-ray spectroscopy[18], this is difficult to regard as an accurate result. A result of time-integrated x-ray spectroscopy is usually considered to represent the most intense x-ray peak. However, this consideration makes incorrect results as the ratio of the energy of the most powerful x-ray peak to total energy decreases. Because most X-pinch produce multiple x-ray peaks, the time-integrated x-ray spectroscopy often leads to incorrect results with mixed plasma states. Several studies have highlighted this point through measurements using time-resolved x-ray spectroscopy on the X-pinch.[22–27] In particular, time-resolved spectroscopy is even more important in the slow X-pinch, which features frequent multi bursts. The studies have also emphasized that the time evolution of X-pinch plasma parameters is significant for X-pinch dynamics study. Thus, we expect that time-resolved x-ray spectroscopy can provide important parameters for the study of the x-ray emission properties and dynamics of the slow X-pinch.

Two methods have been largely used as time-resolved x-ray spectroscopy for the X-pinch. The first is a crystal spectrometer using a streak camera and the second is a filtered XRD array. The

former measures spectra with high spectral resolution in a relatively narrow spectral range. Therefore, detailed spectral analysis is possible and different settings are generally required depending on the target material. Because streak cameras are used, spectral measurements are possible with a fast temporal resolution of the picosecond scale in a narrow time window.[22–27] In the latter case, on the contrary, the spectrum is measured at a low spectral resolution in a wide spectral range. The filtered XRD array can measure spectra with a relatively slow temporal resolution of nanosecond scale. However, unlike the former, measurements can be conducted in the full-time window. Thus, the full-time behavior of the entire x-ray burst can be measured. In particular, because the time jitter of the slow X-pinch is large, the former requiring a precise camera trigger may have difficulty capturing the x-ray peak, whereas in the latter case, all x-ray peaks can be measured regardless of the time jitter. Moreover, filter XRD arrays are simple and relatively inexpensive, so it is a suitable device in terms of laboratory-scale research.[28–36] In conclusion, considering the long emission time, multi bursts, and large time jitter of the slow X-pinch, we determine that the filtered XRD array is more suitable for studying the dynamics of the slow X-pinch.

A filtered XRD array is a combination of foil filters and XRDs with different spectral edges. Researchers widely used one for research in inertial confinement fusion (Omega laser facility [31, 33], National ignition facility [32], and Shenguang-III prototype laser facility [30, 37]) and Z-pinch (Z accelerator [29, 38] and Yang accelerator [39]).

Filtered XRD arrays consist of 5–19 channels and discrete x-ray spectra are reconstructed from x-ray signals measured by channels and x-ray flux and power are calculated from the x-ray spectrum. To reconstruct an x-ray spectrum, a reconstruction process based on response curves of channels is required. Thus, the design of the filter set determines the accuracy of the spectral reconstruction. In other words, a properly designed filter set is the most important part of developing a filtered XRD array.

X-ray spectrum analysis is required to obtain plasma parameters from an x-ray spectrum. It is necessary to compare a measured spectrum with synthetic spectra during the analysis process. Plasma parameters can be estimated by finding the closest case to a measured spectrum in synthetic spectra with different plasma parameters. Therefore, time-resolved spectroscopy as well as spectroscopic modeling is required to obtain plasma parameters. In this study, the FLYCHK code [40] is used for spectroscopic modeling.

Table 1.1 Researches of the slow X-pinch and diagnostics

	Imperial College	Florida A&M University	University of California	Comisión Chilena de Energía Nuclear	Bhabha Atomic Research Centre
Research	1. Characterization of X-pinch[16]	1. Investigation of the X-pinch[18] 2. Investigation of X-ray[19] 3. Plasma jet[20]	1. X-pinch dynamics[15]	1. The behavior of a low impedance generator[41] 2. Coronal plasma[42] 3. Energetic x-ray[21]	1. Point projection radiography[17]
Diagnostics	1. Si PIN diode 2. GaAs PCD 3. Optical emission image 4. Schlieren 5. Multiple aperture x-ray pinhole camera	1. Si photodiodes 2. Diamond PCD 3. Time-integrated optical camera 4. Gated optical camera 5. Interferometer 6. Schlieren 7. Filtered X-ray pinhole camera 8. Slit-wire camera 9. Flat crystal spectrograph	1. PIN diodes 2. Interferometer	1. PIN diode 2. Diamond PCD 3. Shadow diagnostic 4. dark field Schlieren 5. Interferometer 6. Gated VUV/SXR pinhole camera 7. Time-integrated filtered pinhole camera 8. Time-integrated aperture images	1. Si-PIN diodes 2. Time-integrated pinhole camera 3. Slit-wire camera

1.3. Previous works and Motivation

The slow X-pinch has the advantages of small size, simple structure, low cost, and low HXR emission compared to the conventional X-pinch. Thanks to these advantages, it is valuable as a compact point x-ray source for laboratory-scale research. However, it has disadvantages of frequent multi bursts and long x-ray emission time compared to the conventional X-pinch. Identifying the cause of more frequent multi bursts in slow x-pinch will provide important information in improving slow X-pinch. To analyze multi bursts, it is necessary to understand the properties of the plasma that releases them. However, few studies have been conducted to obtain time-resolved plasma parameters in the slow X-pinch.

Therefore, we intend to analyze x-ray peaks of slow X-pinch and plasmas emitting them using a filtered XRD array, as described in Sec. 1.2. However, there are problems with plasma parameter estimation using filtered XRD arrays in previous studies. [16, 35, 36] They inferred electron temperature from continuum spectra such as the recombination spectrum[35, 36] and the bremsstrahlung spectrum.[16] However, plasma parameter estimation using only continuum has problems. It is impossible to estimate electron density because only regions that are not affected by electron density should be used. Also, the presence of intense line radiations can reduce the accuracy of estimation. Previous studies[35, 36] have committed the error of obtaining the slope of the recombination spectrum by using spectral ranges with line radiations. That may cause electron

temperatures to be underestimated. In conclusion, the problems can be solved by plasma parameter estimation considering line radiations. There is another problem that the electron beam generated in the X-pinch was not considered. Electron beams that have higher energy change the x-ray spectrum. Electron beams should be considered to estimate more accurate plasma parameters.[24] Furthermore, electron beams were also predicted to play an important role in the x-ray emission of slow x-pinch.[15, 16, 18, 19] Therefore, the electron beam component should be included as a parameter in the spectrum analysis. To solve the problems, we consider line radiations in the process of plasma parameter estimation to obtain both electron density and electron temperature and include electron beams in the process to more accurately estimate the parameters. Furthermore, the filtered XRD array is delicately designed through a simulation to minimize errors in the spectrum measurement and reconstruction process.

In this study, we develop a diagnostic system including a filtered XRD array and spectroscopic modeling to estimate time-resolved plasma parameters in a slow X-pinch and analyze x-ray peaks from SNU X-pinch[43], which is a slow X-pinch device. The approaches of the study are as follows. First, we delicately design the filter set for the accuracy of the filtered XRD array and validate the accuracy of the spectrum reconstruction method using Geant4 simulation. In addition, channels can be easily simulated by using a commercial detector with a known response curve. Second, synthetic spectra are collected from the FLYCHK code and analyzed for plasma parameter

estimation. X-ray power ratios by spectral ranges are calculated to compare the synthetic spectrum and the measured spectrum. In the process, by considering line radiations and electron beams that were not considered in the spectral analysis using filtered XRD arrays, we make it possible to estimate electron density, fast electron fraction, as well as electron temperature. Finally, we present the time evolution of plasma parameters for the research of slow x-pinch dynamics and try to understand the characteristics of x-ray peaks. In particular, we try to figure up the characteristics of plasmas that emit late-time x-ray peaks that cause multi-bursts and a long emission time.

Chapter 2. SNU X-pinch

2.1. SNU X-pinch[43]

SNU X-pinch is a laboratory-scale versatile X-pinch developed at Seoul National University.[43] Its objectives are a study of X-pinch plasma dynamics, a test for the development of laser-based diagnostics, cooperation with the numerical study [44], and utilization as an x-ray source. The schematic view of the SNU X-pinch is shown in Fig. 2.1. The SNU X-pinch consists of a vacuum chamber for wire load and diagnostics and pulse generator, as shown in Fig. 2.1(a). The vacuum chamber has 12 windows for diagnostics and a vacuum system, and has optical breadboards attached to its bottom, making it easy to install diagnostics, as shown in Fig. 2.2. It is also precisely machined with aluminum mono-block to help align diagnostics. Electrodes are made of brass and installed in the center of the vacuum chamber. The lower electrode is a cathode and connected to the switch; the upper Electrode is an anode and is connected to the chamber ground. The crossing point of the X-pinch load is centered on the windows. The height and width of the X-pinch load are 10 mm and 8 mm, respectively, and it is designed to allow for the installation of 2-12 wires. In this study, only two wires load are used.

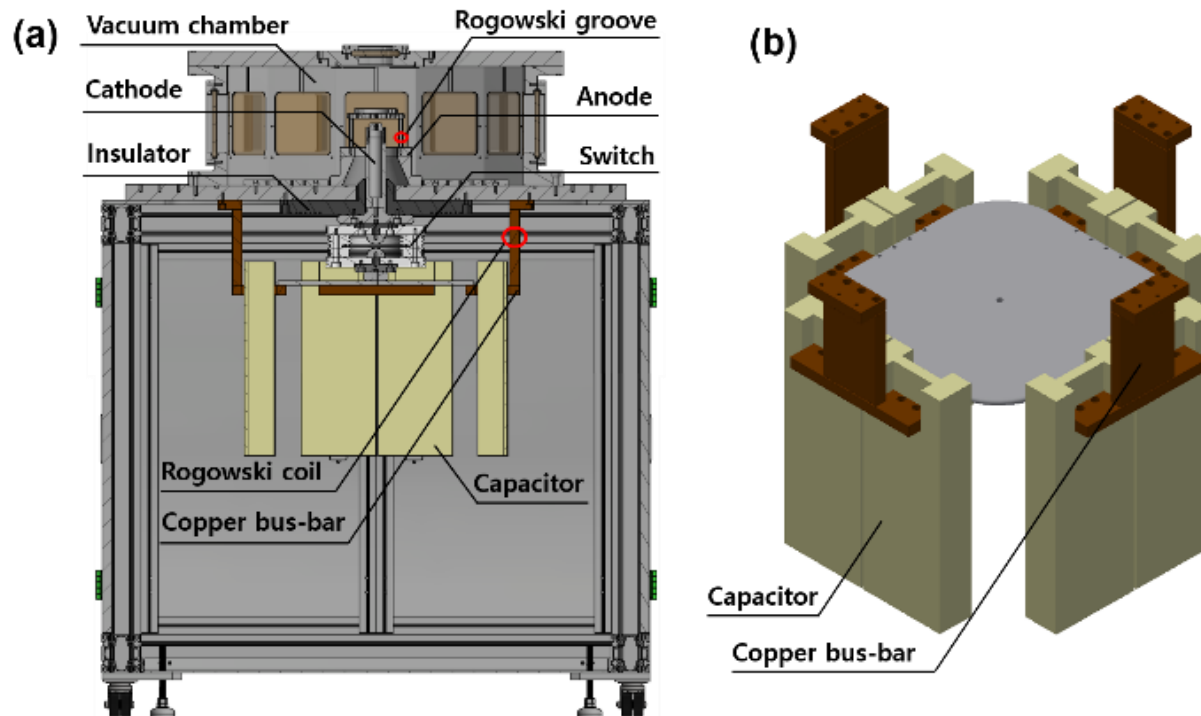


Figure 2.1 (a) The schematic view of the SNU X-pinch, (b) Capacitor bank of the SNU X-pinch [43]

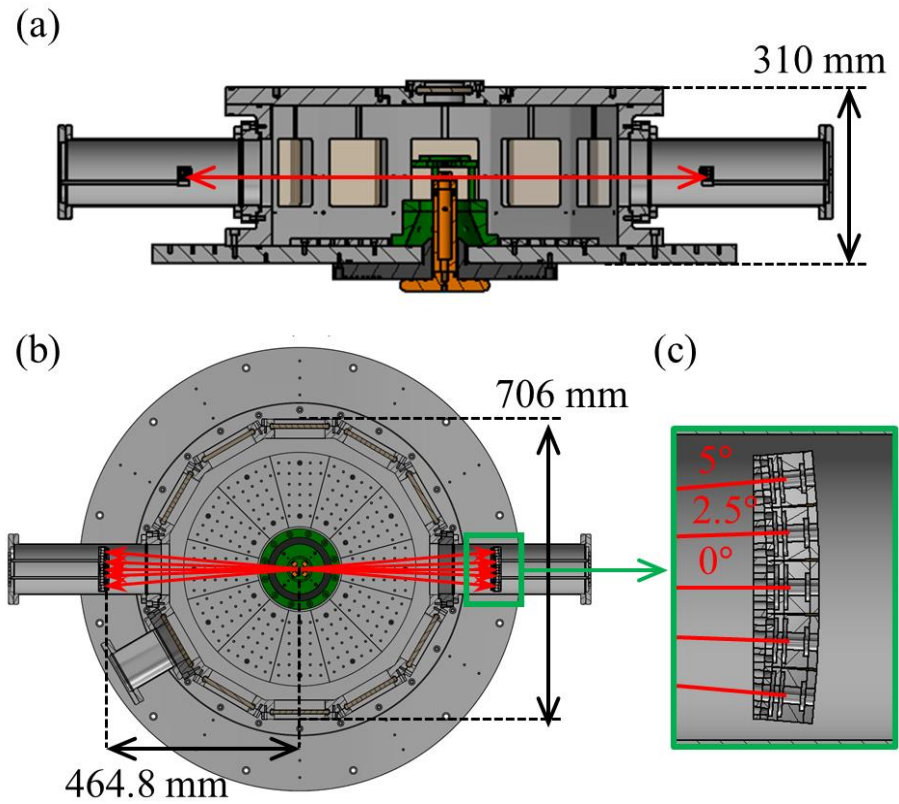


Figure 2.2 (a) Side view and (b) top view of the chamber of the SNU X-pinch and 10-channel filtered AXUV diode array in the chamber. Two diode arrays are installed in two opposite ports at a distance of 464.8mm from the crossing point of the wires. (c) Each module of the array is arranged at an angle to focus on the crossing point.

2.2. Pulse generator[43]

The pulse generator of the SNU X-pinch is a slow-rise current generator, consisting of a capacitor bank and a triggered spark-gap switch, as shown in Figure 2.1 (b). For the capacitor bank, eight capacitors are connected in parallel. The triggered spark-gap switch is filled with N_2 or SF_6 gas for insulation and operated at 30–80 kV depending on the gas pressure. Figure 2.3 shows the results of the pulse generator short circuit test. The current and voltage are measured by Rogowski coil and high-voltage probe which are commercially available on copper bus-bar connected to the capacitor, as shown in Fig. 2.1. Currents of about 100–120 kA are generated with charging voltages of 50–60 kV; Current rise times (0–100%) are approximately 523 ns. Thus, current rise rates are about 0.197–0.234 kA/ns. In this study, experiments are conducted with charging voltages of 50 and 55 kV. A comparison with pulse generators of other slow X-pinch devices is shown in Table 2.1.

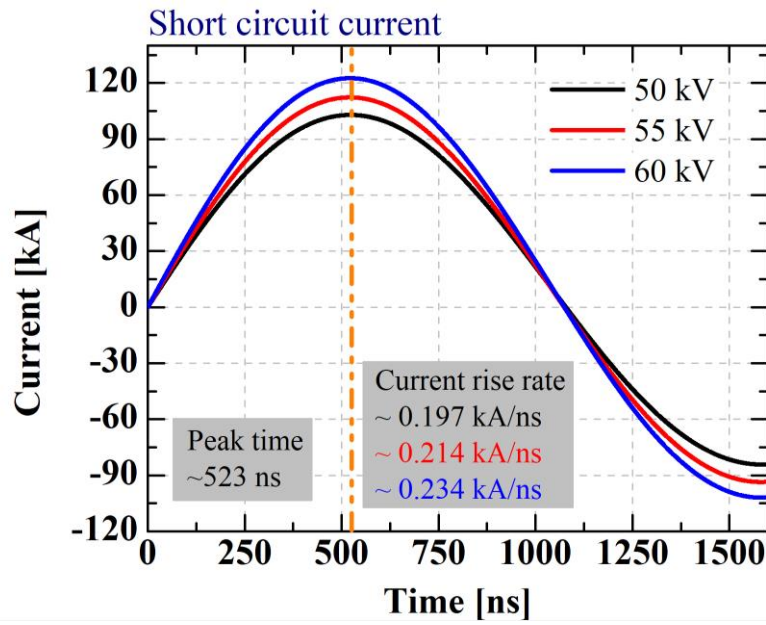


Figure 2.3 The results of short circuit test. Black, red, and blue lines are generated currents with charging voltages of 50, 55, and 60 kV, respectively.

Table 2.1 Specifications of pulse generators of SNU X–pinch and other slow X–pinches

	SNU X–pinch [43]	Imperial College [16]	Florida A&M University [18–20]	University of California [15]	Comisión Chilena de Energía Nuclear [21, 41, 42]	Bhabha Atomic Research Centre [17]
Charging voltage [kV]	50–55	30	35–40	–	24	38
Peak current [kA]	100–110	320	320–350	25	122	110
Rise time [ns]	523 [0–100%]	1200	1000	400	500	1000
dI/dt [kA/ns]	0.197–0.214	0.25	0.3–0.35	0.06	0.244	0.11

Chapter 3. Development of fast time-resolved x-ray diagnostics

3.1. Development of a filtered AXUV diode array

3.1.1. Ten-channel filtered AXUV diode array

Absolute extreme ultraviolet (AXUV) diodes are widely used to measure x-rays in X-pinch experiments.[1] Using these as XRDs, we develop a 10-channel filtered AXUV diode array with a spectral range of 1–10 keV to measure x-rays for the SNU X-pinch device. Because the temperature of the X-pinch plasma is in the sub-kiloelectron volts to several kiloelectron volts range, one would expect x-rays of 1–10 keV to be emitted, and their line radiations are usually in this energy range.[15, 17, 45] Thus, one can obtain important information on hot plasmas from x-ray measurements in this range.[1] Ten channels are selected as the number of diodes due to the lack of resources and installation space. We choose a single kind of detector, AXUV-HS5 (Opto diode, 100 μm thick silicon diode); its active area is 1 mm^2 [Fig. 3.1(a)]. AXUV-HS5 has several features suitable for x-ray measurements in the X-pinch. First, its rise time of 0.7 ns is sufficiently fast for X-pinch measurements and its wide energy range can cover more than 10 keV. Second, its calibrated response function is widely known such that one can design all the channels of the detector array by simulation without absolute calibration.[1, 15, 46] Third, AXUV-HS5 is advantageous for a multi-channel configuration because it is relatively cheap, has a simple structure, and has high accessibility. By using this detector,

one can design cost-effective and simple-structured x-ray diagnostics for the X-pinch. However, there can be quality problems in the fabrication of AXUV-HS5; thus, we have tested the detectors by using a small soft x-ray tube and X-pinch generated x-rays. Signals from the channels are compared, and problematic channels are replaced.

Two sets for AXUV-HS5s and filters are encased by an aluminum casing to shield the detectors against external noise. Each set contains five modules [Fig. 3.1(b)]; thus, two sets contain 10 channels and are installed face-to-face in two opposite ports at a distance of 464.8mm from the crossing point of the wires (Fig. 2.2). Each module contains a set of AXUV-HS5 and foil filters, and one can separately detach them from the housing, rendering it easier to maintain the foil filters and detectors. The modules are arranged at an angle to focus their detectors on the crossing point of the X-pinch [Fig. 2.2(c)]. We use simple circuits of bias tees for direct current bias to the AXUV and signal transmission. The bias tees are in the form of a 50- Ω micro-strip configuration to reduce signal distortion and are encased by an aluminum box to block external noise. Oscilloscopes (1-GHz bandwidth and 6.25-GS/s MSO58LP, Tektronix) record data from the AXUVs.

For the filtered AXUV diode array design, it is important to find an optimized combination of foil filters. We use Geant4 simulations to design and test foil filter sets. Because the foil filter combination is closely related to the x-ray spectrum reconstruction methods, the next section introduces details on the reconstruction methods.

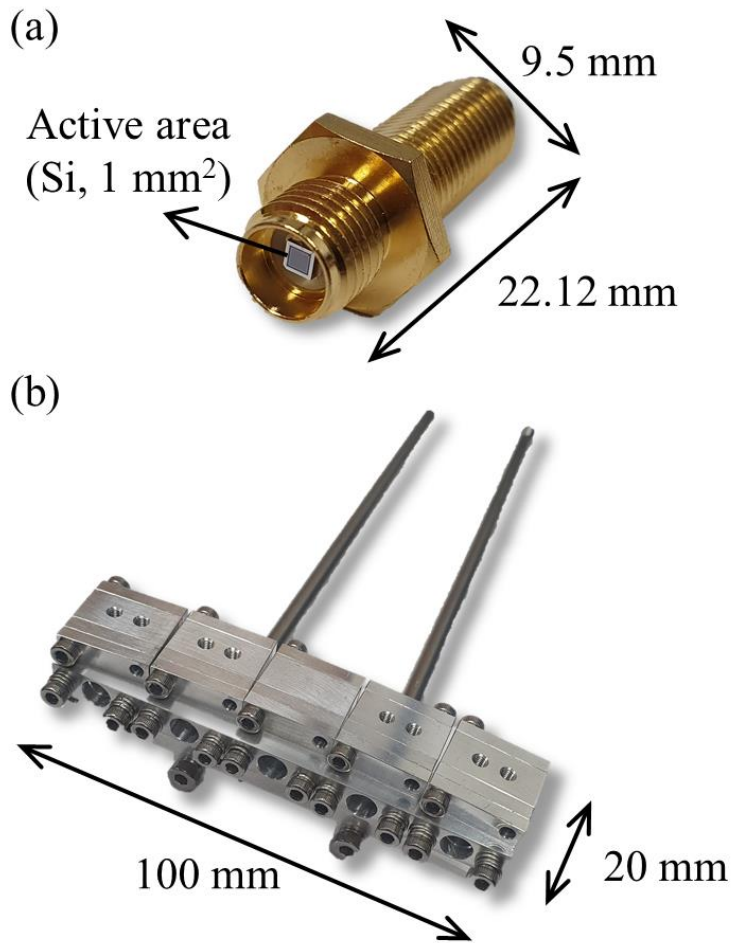


Figure 3.1 a) AXUV-HS5 and (b) aluminum casing for half of the AXUV diode array. The width and length of AXUV-HS5 are 9.5 and 22.12 mm, respectively, and the active area is 1 mm². The aluminum casing consists of five modules, each containing a set of AXUV-HS5 and filters. Two aluminum casings are built; their size is **100 × 20 mm²**

3.1.2. LS method

Least-squares (LS) [29, 30] method is well-known for spectrum reconstruction. One can obtain an x-ray spectrum from pre-calculated virtual channels (VCs) as per the LS method. Because VCs are linear combinations of the response curves of the channels, a combination of the foil filters determines the accuracy of spectrum reconstruction. Thus, we design a filter set and test its quality with the LS method by using Geant4 simulations. Before describing the filter set design, we briefly introduce the LS method. Refer to the work of Tianming et al.[30] and Fehl et al.[29] for more details on the LS method.

The n -th ideal VC H_n is

$$H_n(E) = \begin{cases} 1 & E_{min,n} \leq E \leq E_{max,n}, \\ 0 & \text{otherwise} \end{cases}, \quad (3.1)$$

where H_n is a narrow bandpass channel. We can approximate H_n to a linear combination of response functions of the detector channels, virtual channel VC_n :

$$VC_n(E) = \sum_{i=1}^K a_{n,i} R_i(E) \approx H_n(E) \quad n = 1, \dots, N, \quad (3.2)$$

where $a_{n,i}$ is the coefficient of the i -th channel for n -th VC, R_i is the response function of the i -th channel, K is the number of the filtered detector channels, and N is the number of VCs. Before spectrum reconstruction, the coefficients are predetermined by Eq. (3.2). By Eqs. (3.1) and (3.2), the radiation flux in the energy interval of the n -th VC $\Delta E_n [E_{min,n}, E_{max,n}]$ can be expressed as:

$$\begin{aligned} F_{\Delta E_n} &= \int S(E, t) H(E) dE \approx \int S(E, t) VC(E) dE \\ &= \sum_{i=1}^K a_{n,i} \int S(E, t) R_i(E) dE = \sum_{i=1}^K a_{n,i} V_i(t), \end{aligned} \quad (3.3)$$

where S is the spectrum of the incident x-ray and V_i is the signal from the i -th channel. Finally, we obtain the radiation flux from the pre-calculated coefficients and measured data by the LS method.

The number of channels and the energy range to be measured determine the spectral resolution. In our case, 10 channels are made to measure x-rays of 1–10 keV; thus, the array has a relatively low resolution of ~ 1 keV. Although it has a low spectral resolution, if the VCs are properly composed, one can calculate the discrete spectrum and x-ray power with only small errors. Therefore, we utilize Geant4 simulations to design a filter set and test this method and devise two additional compensation factors to reduce errors generated by the composed VCs.

3.1.3. Filter set design using Geant4 simulation

To accurately reconstruct the spectrum, one should carefully design the filter set, which has a specific response curve for each channel. The response curves should have sharp edges that divide the boundaries of the VCs and be properly combined such that the VCs are flat. Thus, we use Geant4 simulations for the appropriate design of the filter set and have found a proper combination of filters. The matter in the path of the x-ray and detector determines the response curve of each channel. The simulation setup includes the transmission curves of the vacuum, foil filters, and x-ray window (Mylar 1.0 μm), as shown in Fig. 3.2. We simulate AXUV-HS5 as 100- μm thick silicon; Fig. 3.3 shows its simulated response curve.

Its spectral sensitivity (arbitrary units) is matched with the widely known AXUV-HS5 response value of 0.273 A/W.[1, 46]

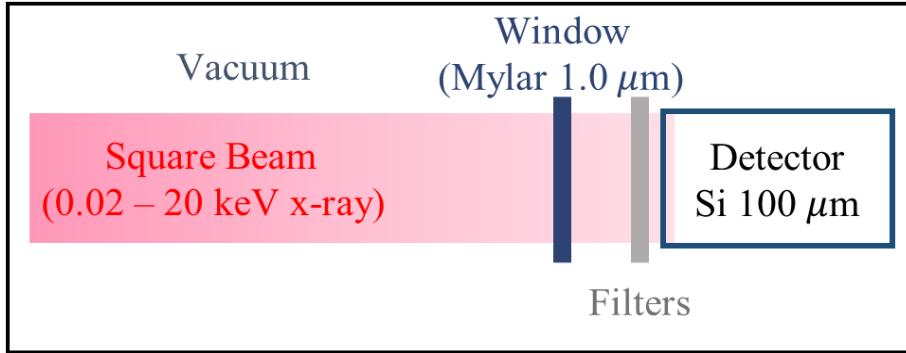


Figure 3.2 Setup of Geant4 simulations for filter set design. Vacuum, window, filters, and AXUV-HS5 are included in the setup. A square-shaped x-ray beam, uniformly distributed from 0.02 to 20 keV, is simulated to obtain response curves.

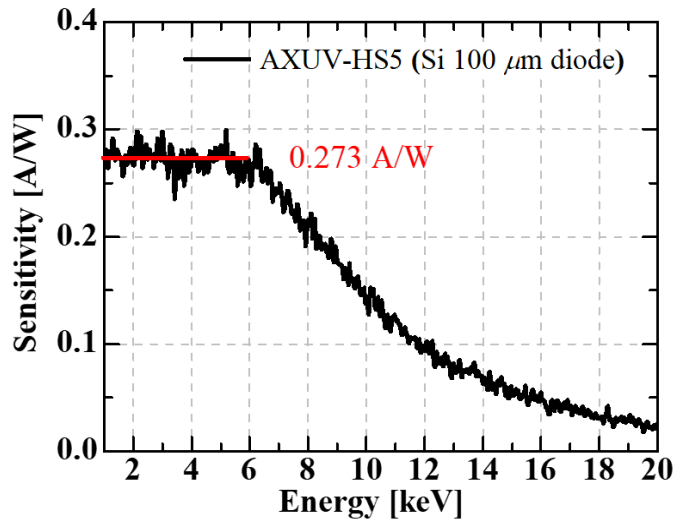


Figure 3.3 Response curve of AXUV-HS5 obtained by Geant4 simulations. The response curve is matched with the known AXUV-HS5 response curve.

We select foil filters with several criteria. First, the transmission curves of the foil filters should have a clear spectral edge in the spectral range of 1–10 keV. Second, the gap between the spectral edges should be ~ 1 keV. Third, the transmittance at the spectral edge of the channel should not be appreciably different from that of the front and rear channels. We combine and simulate the selected candidates by changing the thickness to render the VCs as close to the ideal shape as possible. Table 3.1 shows the filter set designed by Geant4 simulations and its spectral band edges, a lower energy edge (10% of maximum sensitivity) to a spectral edge of the filter; [33] Fig. 3.4 shows the response curves of the filter set.

We use a single kind of detector, AXUV–HS5, which has a wide detectable energy range. It makes large tails beyond the edge in the response curves; these tails must be eliminated to make flat–and sharp VCs. We use the continuum channel (channel 1 in Fig. 3.4) with no spectral edge to mathematically remove the large tails in the process of forming VCs. The continuum channel is included in the linear combination of the response curves for the VC formation, yet does not divide the boundaries of the VCs. The other nine channels (channels 2–10) divide the energy range of 1–10 keV into nine regions; i.e., 10 channels ($K = 10$) make nine VCs ($N = 9$). Figures 3.5(a) and 3.5(b) show the VCs without and with the continuum channel. The quality of the VCs, especially VC_1 and VC_5 , is improved by including the continuum channel. Both VCs are difficult to form compared with other VCs. In the case of VC_1 , there is no channel in the energy range lower than channel 2; thus, it is difficult to render

VC_1 an ideal shape. In the case of VC_5 , it is also difficult to render VC_5 an ideal shape due to the large difference in the tails of the response curves for channels 5 and 6. Therefore, in both cases, the addition of the continuum channel helps to remove the tails of the response curves and increase the quality of the VCs.

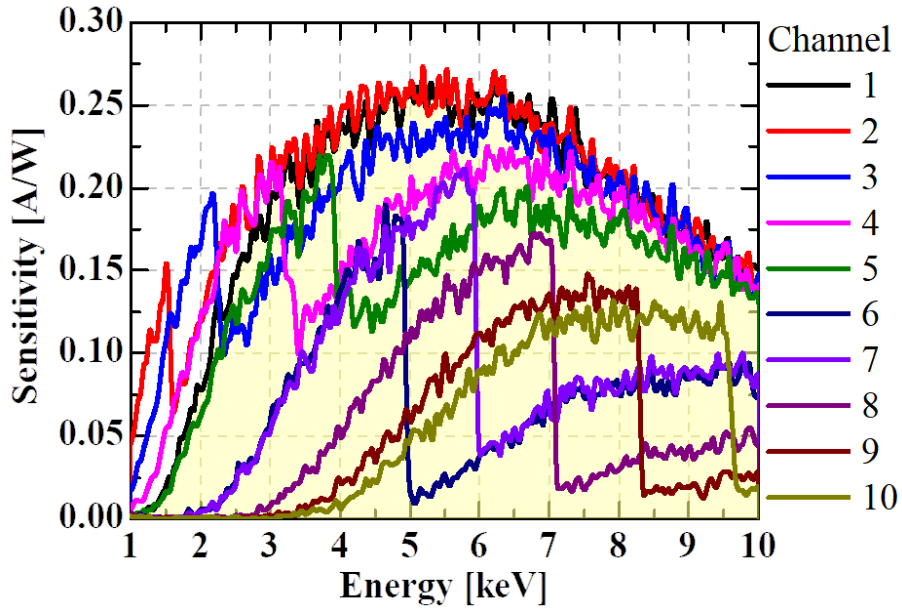


Figure 3.4 Response curves of the channels. Channel 1 (yellow area) has no spectral edge. The other channels divide the energy range for nine VCs.

Table 3.1 Filter material and its spectral band edge of each channel.

Channel	Filter material (μm)	Spectral band edge (keV)
1	Teflon (6) + Be (10)	1.60–Continuum
2	Al (1) + Be (10)	0.86–1.58
3	Zr (0.5) + Be (10)	1.02–2.30
4	Pd (0.4) + Be (10)	1.30–3.38
5	Sn (1) + Be (10)	1.58–3.98
6	Ti (10)	2.50–5.02
7	Cr (5)	2.50–5.98
8	Fe (8)	3.22–7.14
9	Ni (9)	3.94–8.34
10	Zn (12)	4.30–9.70

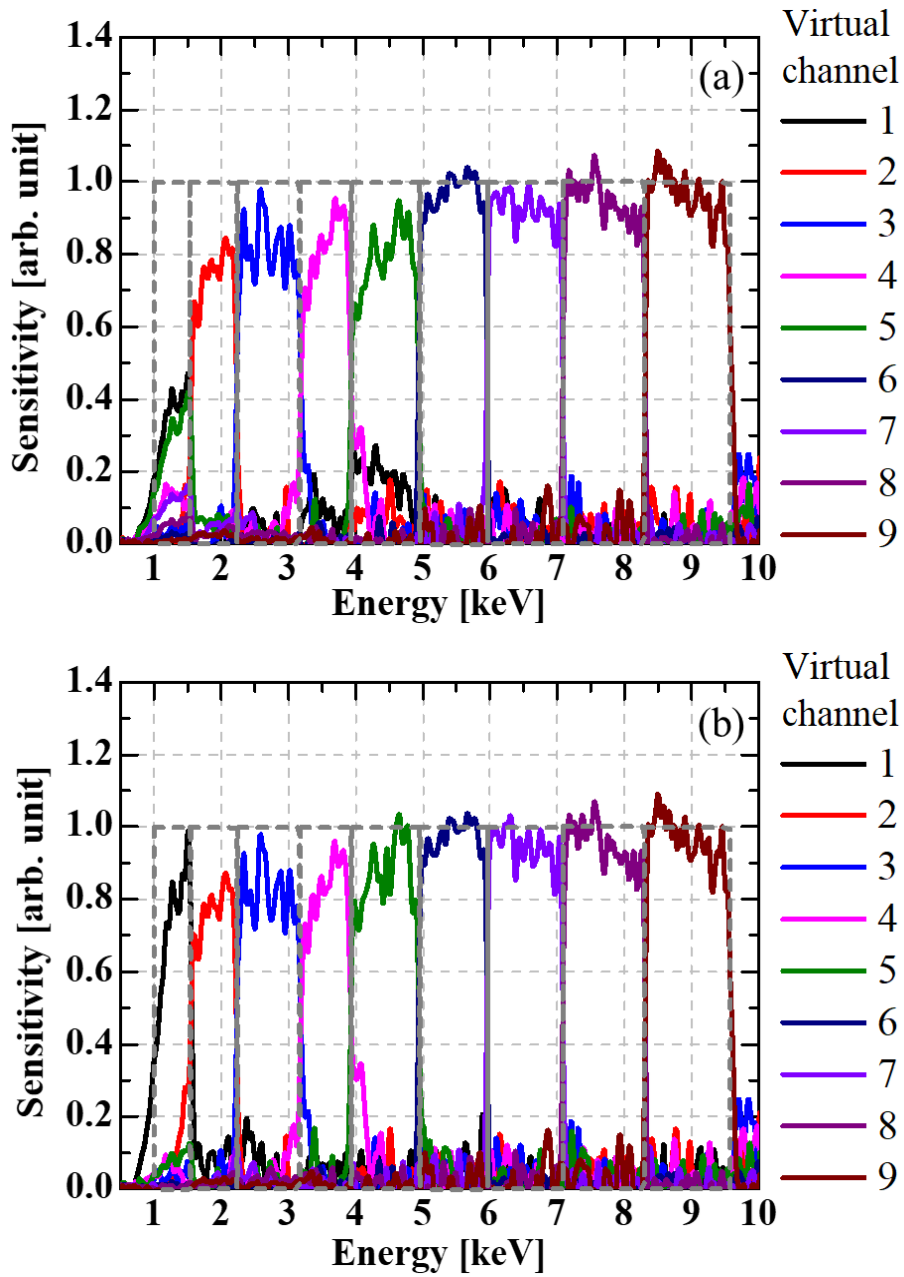


Figure 3.5 (a) VCs without a continuum channel and (b) VCs with a continuum channel (channel 1). Without a continuum channel, there are problems with formatting VCs 1 and 5.

3.1.4. Compensation factors

When the VCs deviate from a flat shape, the VCs generate reconstruction errors. Despite the addition of the continuum channel to remove the large tail of AXUV-HS5's response curve, the VCs (especially VC₁–VC₅) are still imperfect. To reduce the errors that are attributable to the imperfection of the VCs, we introduce two additional compensation factors. There are two major defects of the VCs: (1) lower and uneven sensitivity of the VCs compared with ideal VCs, and (2) sensitivity beyond each VC (Fig. 3.6). The first defect causes one to underestimate the reconstruction results of the VCs. Thus, the first compensation factor ($w_{1,n}$) of VC_{*n*} adjusts the average sensitivity of each VC to 1 to correct the first defect (Fig. 3.7). The second defect is caused by the failure to make sensitivity completely zero outside of each VC's energy range ΔE_n and produces unwanted signals that should be excluded from spectrum reconstruction. It is not clearly distinguished from the noise and is small compared with the first defect; however, it should be considered for reconstruction accuracy. Accordingly, we make the second compensation factor ($w_{2,n}$) of VC_{*n*}, which is the ratio of the signal in each VC's energy range (ΔE_n) to the signal in the entire energy range (E_L to E_H) as described in Fig. 3.6. The $w_{2,n}$ compensates the reconstructed spectrum. However, the errors of the initial spectrum reconstruction should not be too large, because one calculates $w_{2,n}$ based on the initially reconstructed spectrum (S_{LS}) from the VCs adjusted by w_1 :

$$w_{1,n} = \Delta E_n / \int_{E_{min,n}}^{E_{max,n}} VC_n(E) dE, \quad (3.4)$$

$$w_{2,n} = \int_{E_{min,n}}^{E_{max,n}} S_{LS}(E, t) w_{1,n} VC_n(E) dE / \int_{E_L}^{E_H} S_{LS}(E, t) w_{1,n} VC_n(E) dE. \quad (3.5)$$

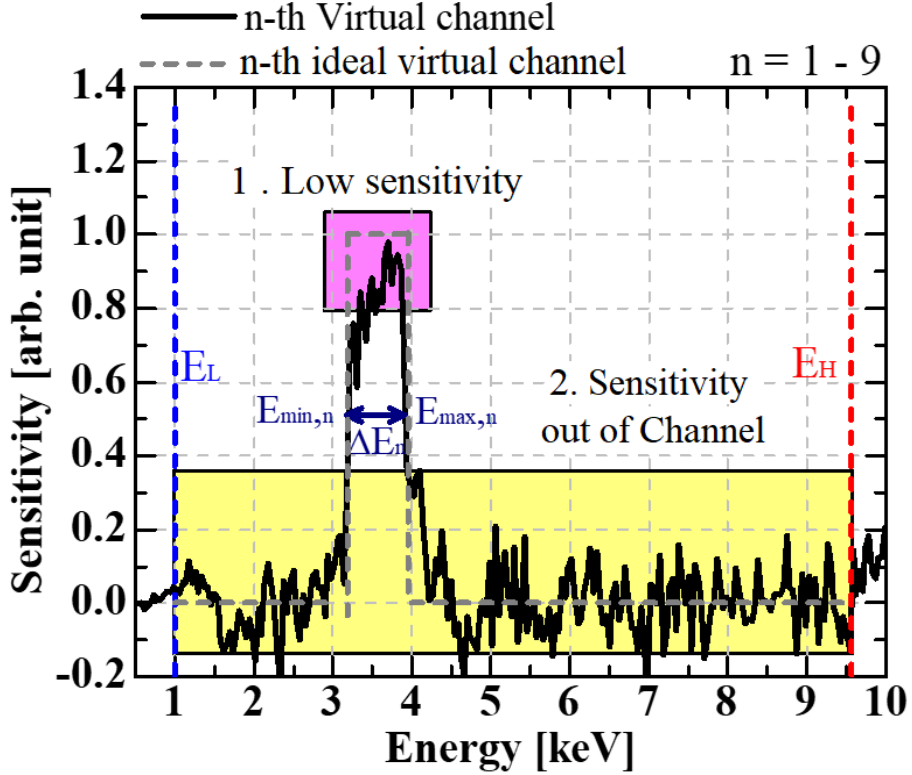


Figure 3.6 Two major defects of VCs. The first defect is low sensitivity (magenta) and the second defect is sensitivity out of the VC (yellow). E_H and E_L are the maximum and minimum energy of reconstruction, respectively. $E_{min,n}$ and $E_{max,n}$ are the maximum and minimum energy of the n -th virtual channel, respectively. ΔE_n is its interval.

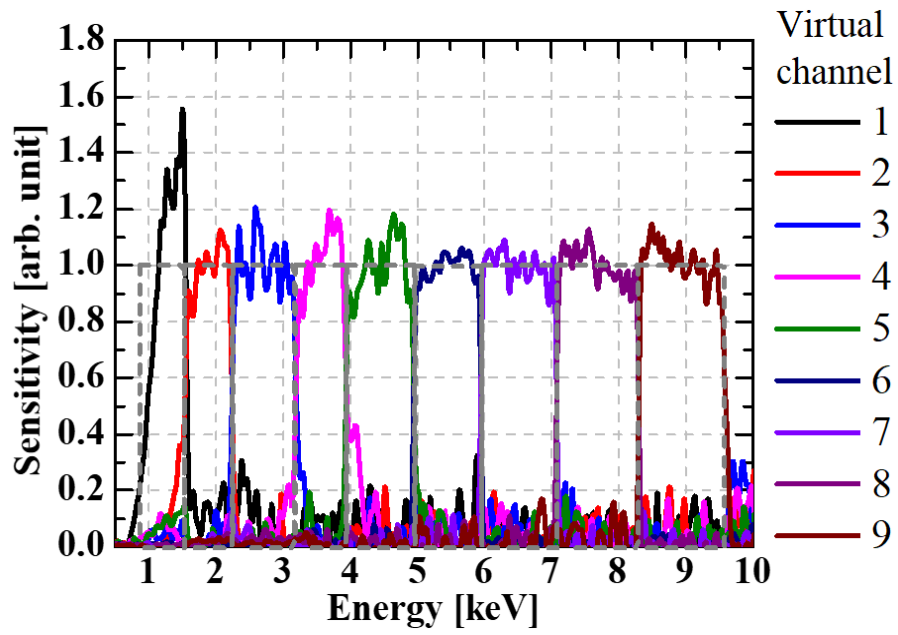


Figure 3.7 Compensated VCs. The n -th virtual channel is compensated by the first compensation factor ($w_{1,n}$).

3.1.5. Test cases by Geant4 simulation

We prepare a uniformly distributed spectrum, blackbody radiation, and blackbody radiation with a Gaussian peak spectrum as reference spectra of test cases by Geant4 simulations, and reconstruct them by the LS method (Fig. 3.8). The errors are reduced considerably after applying two compensation factors in all cases, resulting in an improved quality of the reconstructed spectrum. Especially, in the case of 1 keV blackbody radiation, the errors on VC_8 and VC_9 with small intensities are reduced considerably after the compensation. However, the signal intensity from VC_1 is still overestimated in all spectra, which is due to the non-flat response curve of VC_1 . Because the compensated response curve of VC_1 is not flat, it has a positive slope with a large sensitivity for higher energy toward the second channel (Fig. 3.7). When the spectrum in the VC_1 range has a positive slope for blackbody radiation [Figs. 3.8(b)–3.8(d)], the positive slope of the response curve amplifies the large intensity. This overestimates the reconstruction of VC_1 .

To mitigate this overestimation, we need to render VC_1 flat by combining VC_1 and VC_2 , reducing the number of VCs from nine to eight (Fig. 3.9). VC_1 of the new eight-VC array has a flatter response curve compared with that of VC_1 . Figure 3.10 shows that the reconstruction results are improved; the error of VC_1 is less than 10%. However, for the eight-VC case, the energy resolution lessens in the low-energy region where one would expect the intensity of the spectrum to be the strongest. For low radiation temperature cases at which the spectrum has a negative slope in VC_1 , one would

expect VCs to have low errors; thus, we utilize both eight and nine VCs.

Although the LS method has relatively low energy resolution, one can still use it to calculate the x-ray power in a manner that does not require an accurate spectrum shape. The Geant4 simulation results indicate that one can calculate the x-ray power with an error of less than 10%. We utilize the results of the LS method to estimate plasma parameters by comparing them with synthetic spectra.

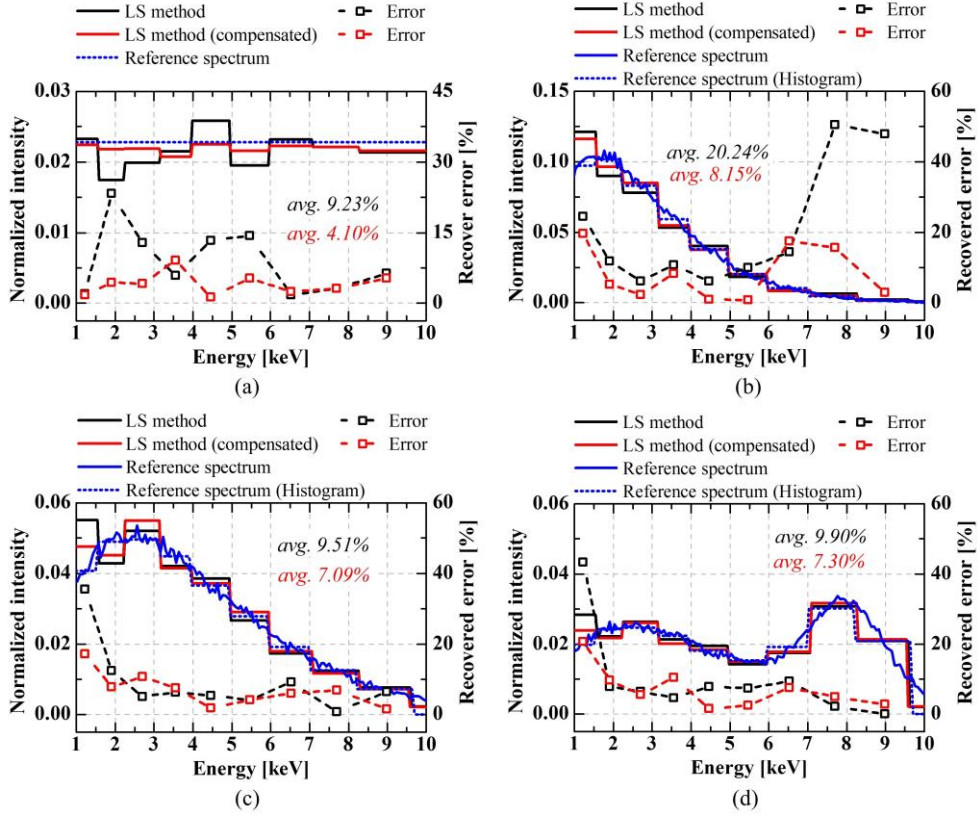


Figure 3.8 Reconstruction results of the LS method. (a) Uniform spectrum, (b) 1 keV blackbody radiation spectrum, (c) 1.5 keV blackbody radiation spectrum, and (d) 1.5 keV blackbody radiation spectrum with a Gaussian peak at 8 keV. Blue line, input spectrum; blue dashed line, histogram of the input spectrum. Black line, reconstruction results of the VCs; red line, reconstruction results of compensated VCs. Black and red dashed lines with square symbols, channel errors of reconstruction results of VCs and compensated VCs, respectively.

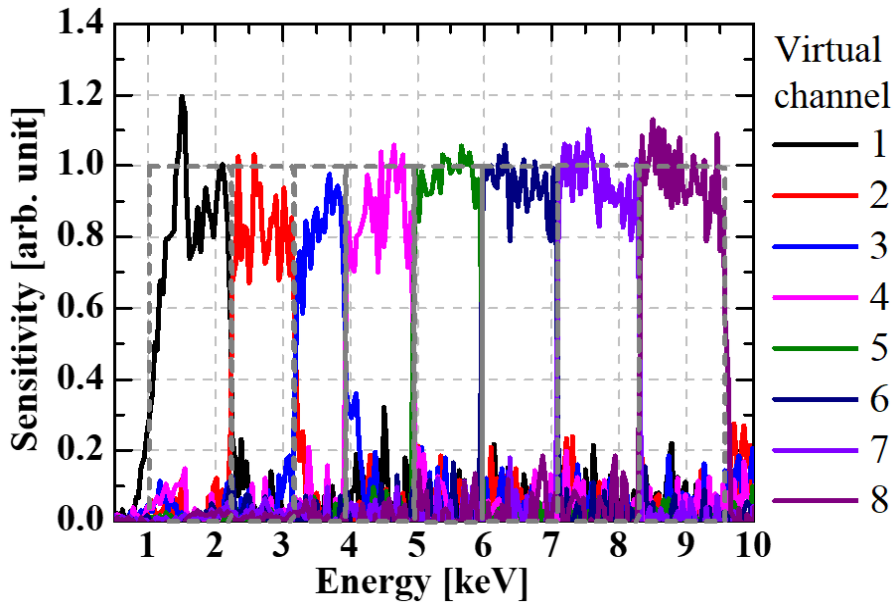


Figure 3.9 Eight VCs. VCs 1 and 2 are combined into the first channel of eight VCs.

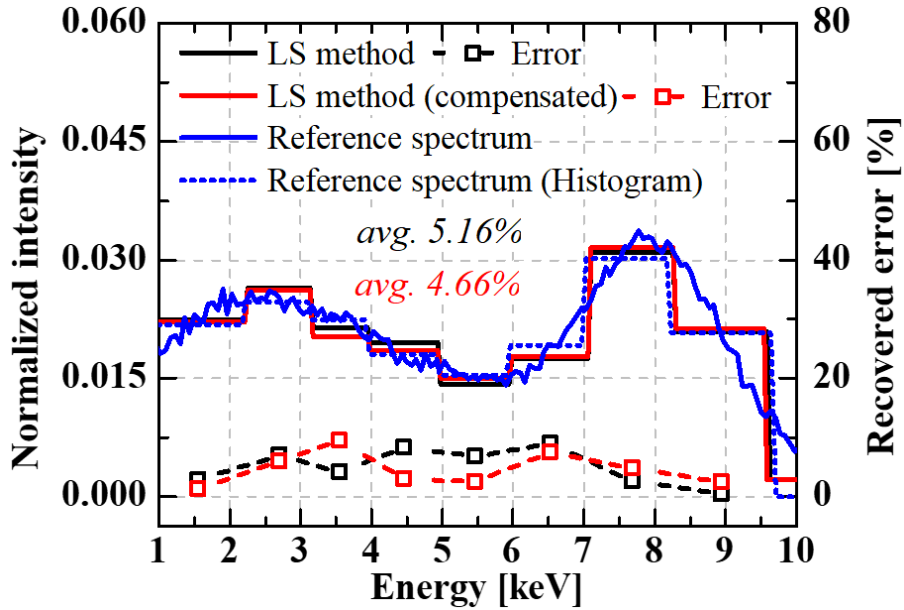


Figure 3.10 Reconstruction results of a 1.5 keV blackbody radiation spectrum with a Gaussian peak at 8 keV by new eight VCs. The errors of the eight VCs are less than 10% and much smaller than the error of VC₁.

3.2. Plasma parameter estimation method

3.2.1. Cu plasma emitted x-ray spectrum analysis by FLYCHK code and x-ray power ratios

Cu plasmas generated by the X-pinch emit x-rays with different spectra depending on the electron temperature, electron density, and existence of fast electrons. The plasma parameters can be estimated by comparing measured x-ray data with spectroscopic modeling. We used the FLYCHK code as a tool for spectroscopic modeling. The FLYCHK code is a simple collisional-radiative code that can quickly calculate reasonable spectra. It can also be applied to most laboratory plasma. In particular, considering that most of the atomic data of high-Z elements are classified, that is an advantage in laboratory-scale research. However, due to the simplicity of FLYCHK, we have to check its feasibility for X-pinch plasma. The spectra obtained from the FLYCHK code were compared with the spectra measured in several plasmas and confirmed to be reasonable.[40] However, the range in which the FLYCHK code can calculate reasonable results is limited. A previous study[47] conducted a study comparing the results of ATOMIC code and FLYCHK code for copper plasma which is our target plasma. As a result, the FLYCHK code showed inaccurate results for strongly coupled plasma (coupling parameter $\Gamma > 1$). The parameter range of plasmas we are interested in, 0.1–3 keV and $10^{18} - 10^{24} \text{ cm}^{-3}$, does not correspond to strongly coupled plasma; Γ for HS is ~ 0.01 and for cold dense plasma (10^{23} cm^{-3} , 0.1 keV) ~ 0.1 . However, it should be noted that errors can occur with

lower temperatures and higher densities

Since the study was conducted on the mean opacity and mean charge, we further compare the results of the opacity spectrum calculation of the two codes. The results obtained from the two codes are similar overall; however, there are differences in the range where K -shell radiations are produced, as shown in Fig 3.11. However, previous studies [48–50] show that the FLYCHK code can calculate Cu K -shell radiations well. Therefore, we conclude that it is feasible to simulate the spectrum produced by Cu X-pinch using the FLYCHK code.

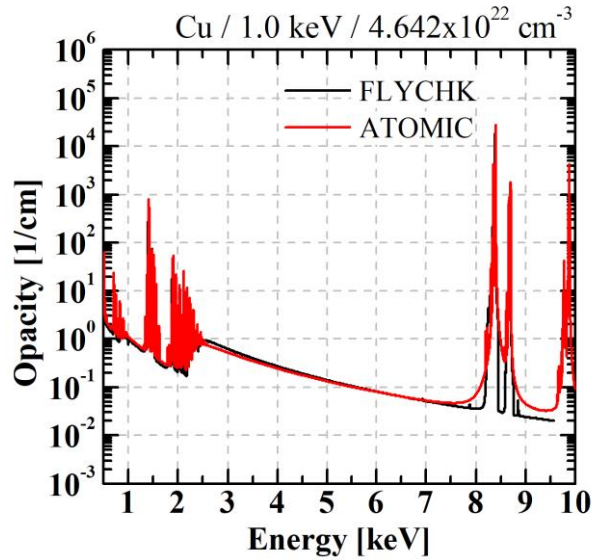


Figure 3.11 Opacity spectra of Cu plasma with an electron temperature of 1.0 keV and an electron density of $4.642 \times 10^{22} \text{ cm}^{-3}$ produced by FLYCHK (black) and ATOMIC (red) codes.

The spectrum can be directly obtained by an x-ray spectrometer using a crystal. The ratios between line radiations vary depending on the electron temperature and electron density; from the ratios, they can be estimated. This method is applied to both relatively low-energy L -shell radiations[23, 24] and relatively high-energy K -shell radiations.[22, 23] Unfortunately, since the spectral resolution of the filtered AXUV diode array is about 1 keV, it is difficult to estimate plasma parameters by comparing each line radiation with one of the synthetic spectra. However, we can obtain a board spectrum in the 0.9 to 9.6 keV range containing both L -shell and K -shell line radiations. If L -shell, K -shell radiation, and continuum radiation change differently depending on the plasma parameters, they can be estimated from an x-ray spectrum measured by the filtered AXUV diode array.

To confirm whether plasma parameter estimation using the filtered AXUV diode array is possible, the synthetic spectrum of Cu plasma is analyzed. The normalized synthetic spectra are obtained from the FLYCHK code with different electron temperatures and electron densities.[40] Figure 3.12 shows spectra with different electron temperatures and an electron density of 10^{21} cm^{-3} . As the temperature increases, the slope of continuum radiation increases, and some L -shell radiations and K -shell radiations are slightly enhanced. Since the slope of the spectrum of continuum radiation (recombination spectrum) is inversely proportional to the electron temperature, the temperature can be calculated directly from that. [35, 36] However, the intensity of continuum radiation is very weak

compared to line radiation and the measured continuum spectrum is greatly affected by the measurement errors and electrical noises; therefore, we do not use the slope for temperature prediction. On the other hand, as the density increases, the L -shell radiations and the continuum radiation increase significantly as shown in Fig. 3.13.

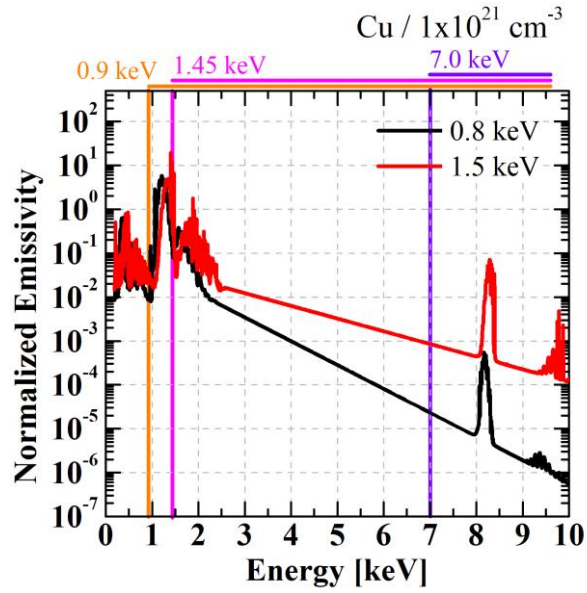


Figure 3.12 Synthetic spectra with electron temperatures of 0.8 (black) and 1.5 keV (red) and an electron density of 10^{21} cm^{-3}

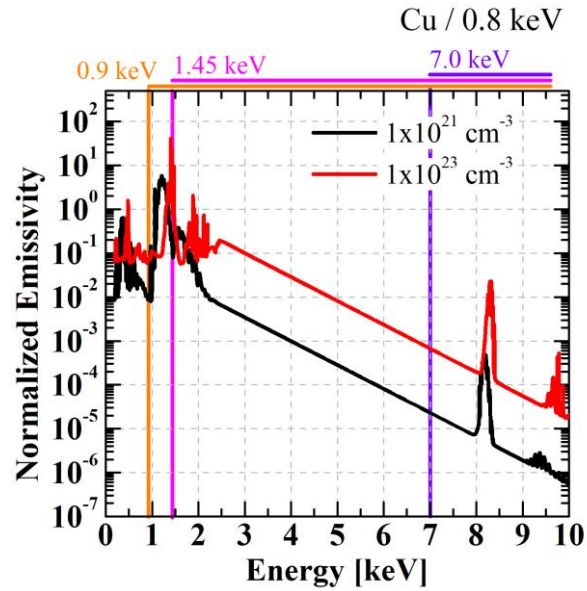


Figure 3.13 Synthetic spectra with electron densities of 10^{21} (black) and 10^{23} cm^{-3} (red) and an electron temperature of 0.8 keV

To quantify the change in spectrum according to each parameter, we set three regions considering the spectral edge of the AXUV array; the first region (R_1) is the full range of the AXUV array, 0.9 to 9.6 keV, the second region (R_2) cover 1.45 to 9.6 keV, and the third region (R_3) cover 7.0 to 9.6 keV. Because of the small intensity of continuum radiation, some L -shell radiations, which are intensified with the rise of the temperature and density, are included in the R_2 to make a clear difference from the third region. The third region mainly includes K -shell radiations. The integrated values of each region are proportional to the power of the x-rays from each energy region. To compare the three regions of the synthetic spectra with those of measured ones, x-ray power ratios of the second region and the first region and one of the third region and the first region are calculated; we call the ratios the first (r_1) and second (r_2) ratios. To take into account errors from the spectrum reconstruction process of the filtered AXUV diode array, the synthetic spectra are reconstructed by the LS method, and the x-ray power ratios are calculated from the reconstructed spectrum (S).

$$r_1 = \left(\int_{R_2} S(E) dE \right) / \left(\int_{R_1} S(E) dE \right) \quad (3.6)$$

$$r_2 = \left(\int_{R_3} S(E) dE \right) / \left(\int_{R_1} S(E) dE \right) \quad (3.7)$$

The x-ray power ratios are pre-calculated under the following conditions and the results are shown in Fig. 3.14. The electron densities are set from 10^{18} to 10^{24} cm^{-3} and the electron temperatures are set from 0.1 to 3 keV. Overall, the ratios increase as electron temperature and electron density increase; however,

when the electron density is larger than 10^{23} cm^{-3} , there is a range in which r_2 decreases. In this range, r_1 continues to increase, which will help determine the electron density of more than 10^{23} cm^{-3} . When the electron density is less than 10^{21} cm^{-3} , there is little change in the ratios according to the electron density; therefore it is difficult to determine the electron density from 10^{18} to 10^{20} cm^{-3} . The first ratio is the most important in determining the temperature because it is the only one dependent on the temperature below 1.5 keV. For much the lower temperature of 0.1 keV, it is difficult to accurately determine the density due to the low dependence on electron density.

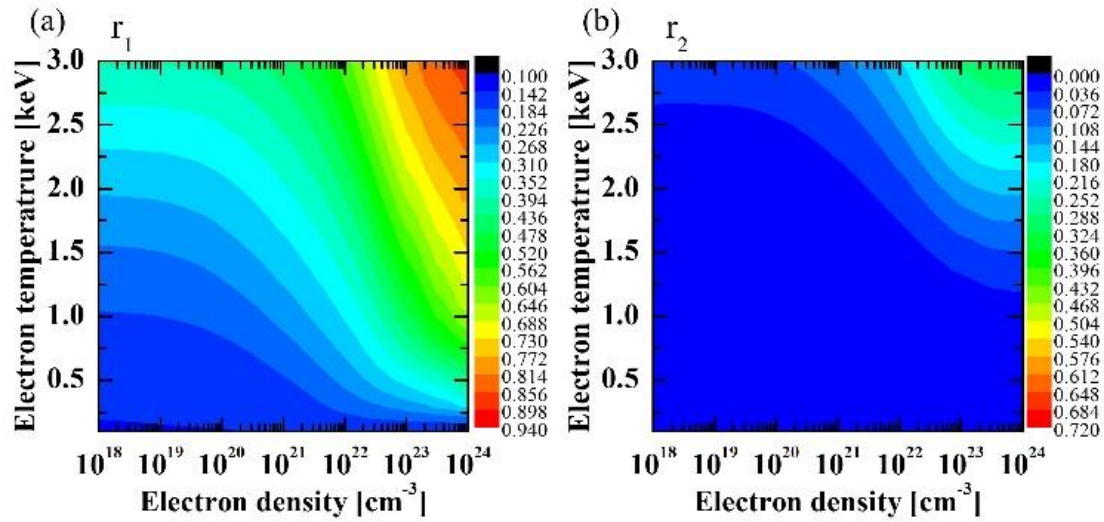


Figure 3.14 The x-ray power ratios with different electron temperatures and electron densities obtained from the FLYCHK code. (a) and (b) are the first and second ratios

3.2.2. X-ray power ratios with fast electrons

The x-ray spectrum is also changed by fast electrons. According to the previous studies, the relative ratios of line radiations are changed and especially the cold K -shell radiation and the high-energy continuum radiation are strengthened by fast electrons.[5, 24, 51] In the X-pinch, fast electrons are generated in the form of electron beams, so it is necessary to consider them for more accurate plasma parameter estimation. The FLYCHK code has a function to add a second electron component with Maxwellian or non-Maxwellian distribution to calculation, thus we utilize the function.

The important factors in modeling fast electrons in the X-pinch are the distribution function of the fast electrons, its characteristic energy, and its fraction. The fast electrons have been simulated using Gaussian, Maxwellian, and power-law distributions. The effect on the spectrum varies depending on the distributions of the fast electrons, but an exact distribution of the fast electrons is unknown.[51] Since figuring out the exact distribution of the fast electrons is beyond our research objective, we model them using Maxwellian distribution following the previous study.[5] Nevertheless, to minimize the influence of the distribution function, the characteristic energy is set to 10 keV, which is greater than the maximum value of the spectral range we measure. On the other hand, a characteristic energy can also affect the spectrum. The x-ray spectrum emitted by the HS with high electron temperature is hardly affected by the characteristic energy, as shown in Figs. 3.15. However, if plasma temperature is low, x-ray spectra vary

depending on the characteristic energy, as shown in Figs. 3.16. This is because, there are fewer high-energy electrons in the bulk plasma with low electron temperature, increasing the influence of the fast electron component. Unfortunately, the exact distribution of fast electrons produced in the X-pinch is unknown. Therefore, this becomes the uncertainty of plasma parameter estimation.

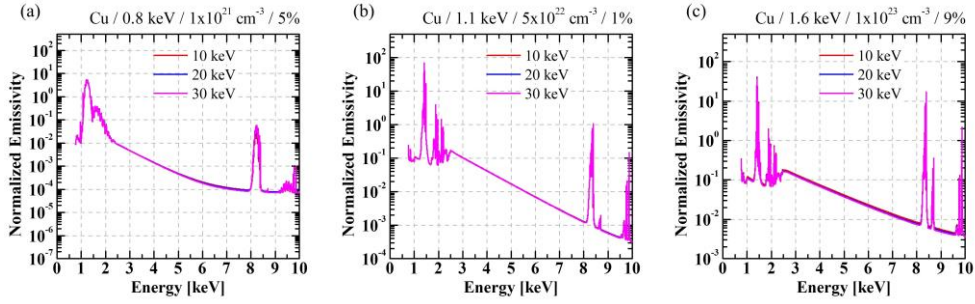


Figure 3.15 Synthetic spectra with different characteristic energies of 10 (red), 20 (blue), and 30 (magenta) keV. (a) to (c) show the spectra with different electron temperatures, electron densities, and fast electron fractions, and represent ones of HS plasma.

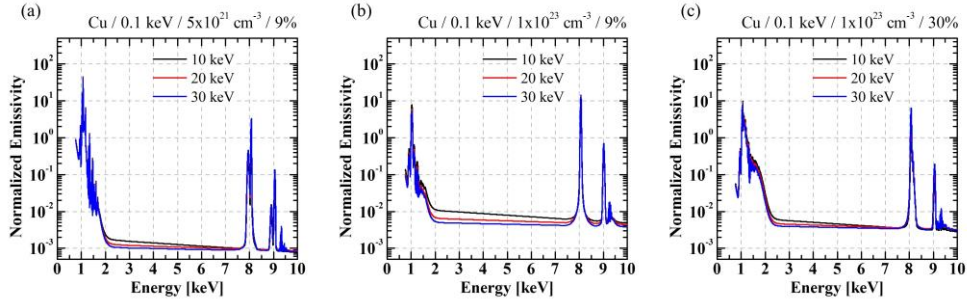


Figure 3.16 Synthetic spectra with different characteristic energies of 10 (red), 20 (blue), and 30 (magenta) keV. (a) to (c) show the spectra with different electron temperatures, electron densities, and fast electron fractions.

Spectra with different fractions of fast electrons to total electrons are obtained from the FLYCHK code. Figure 3.17 shows the spectra with 0% and 5% of fast electrons in plasmas of which electron temperature of 0.8 keV and electron density of 10^{21} cm^{-3} . As the results of previous studies[5, 51], high-energy continuum radiations and K -shell radiations are strengthened.

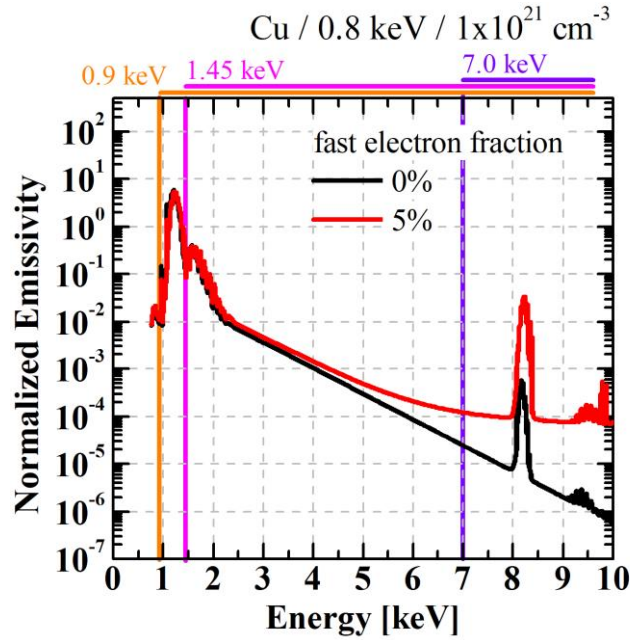


Figure 3.17 Synthetic spectra with the fast electron fractions of 0% (black) and 5% (red). An electron temperature is 0.8 keV and electron density is 10^{21} cm^{-3}

The x-ray power ratios are pre-calculated with the fast electron fractions of 1, 3, 5, 7, 9, 12, 15, 20, 30, 40, and 50%; the electron temperature and the electron density are set as in the previous case. Figure 3.18 shows the x-ray power ratios with the fast electron fraction of 1%. The ratios change more with electron temperature and electron density compared with those of 0% fast electron fraction. When the electron temperature is low, the ratios tend to increase as opposed to the previous case. In particular, increases in the ratio are noticeable at densities of less than 10^{20} and more than 10^{22} cm^{-3} . The increase in the ratios at low temperatures will increase the discrimination of plasma parameters in the presence of fast electrons, unlike the 0% fast electron fraction case.

Higher fast electron fraction cases are illustrated in Figs. 3.19 – 3.21. As the fast electron fractions increase, overall ratios increase, and the dependence of the ratios on the electron temperature and the electron density gradually increases. However, the ratios of the low-temperature range, which rise sharply at 1% fast electron fraction case, rather decrease, especially below 10^{20} cm^{-3} .

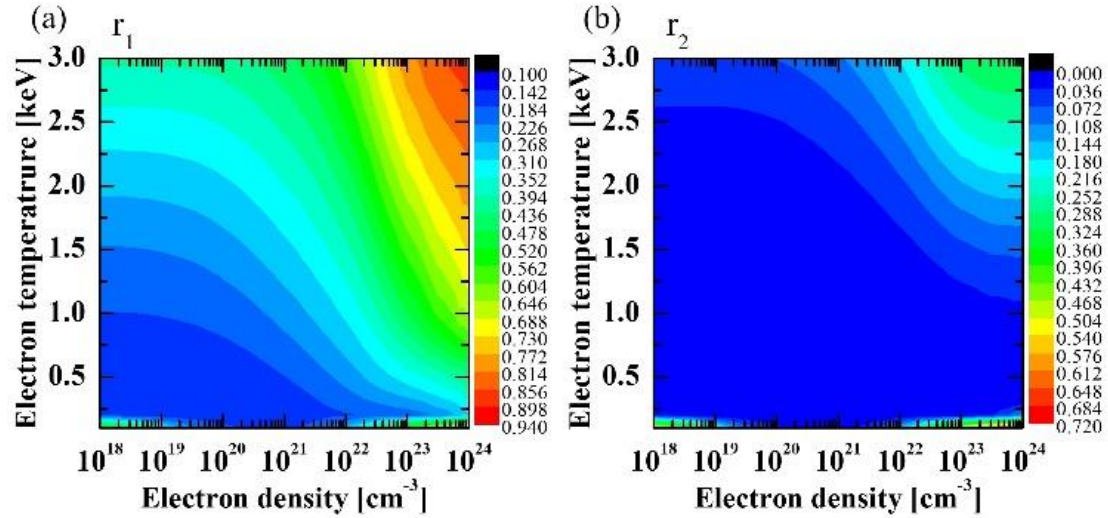


Figure 3.18 The x-ray power ratios with a fast electron fraction of 1% obtained from the FLYCHK code. (a) and (b) are the first and second ratios.

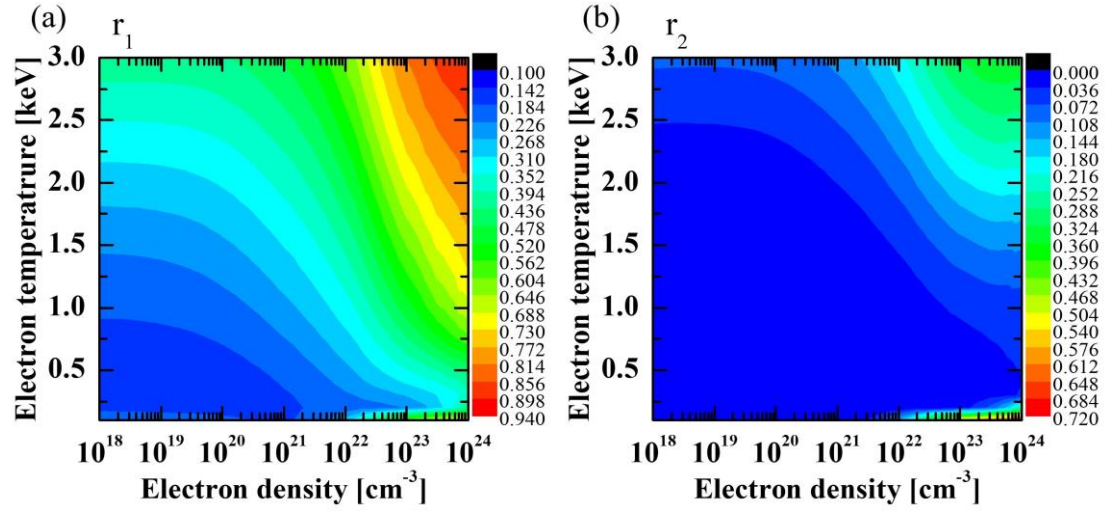


Figure 3.19 The x-ray power ratios with a fast electron fraction of 5% obtained from the FLYCHK code. (a) and (b) are the first and second ratios.

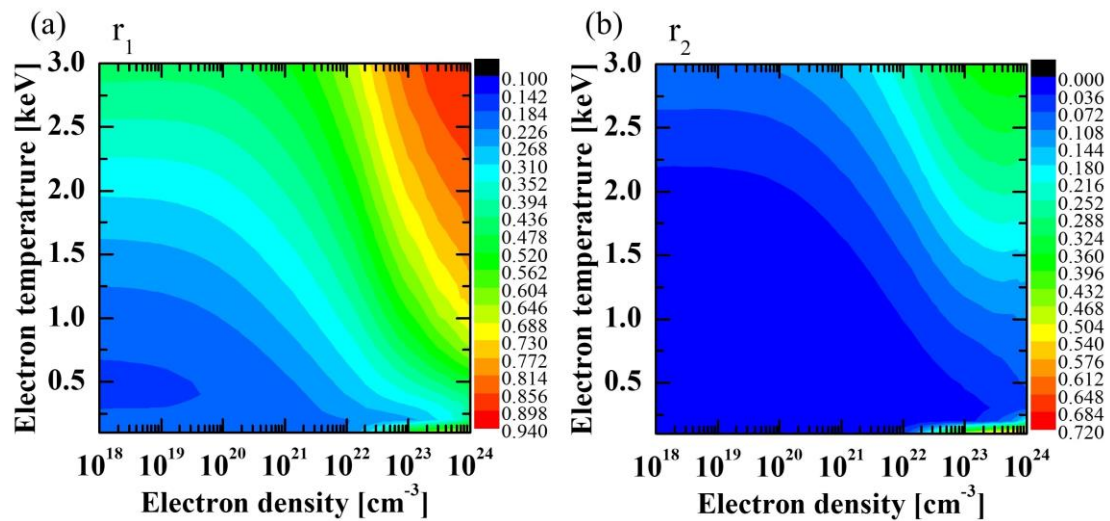


Figure 3.20 The x-ray power ratios with a fast electron fraction of 12% obtained from the FLYCHK code. (a) and (b) are the first and second ratios.

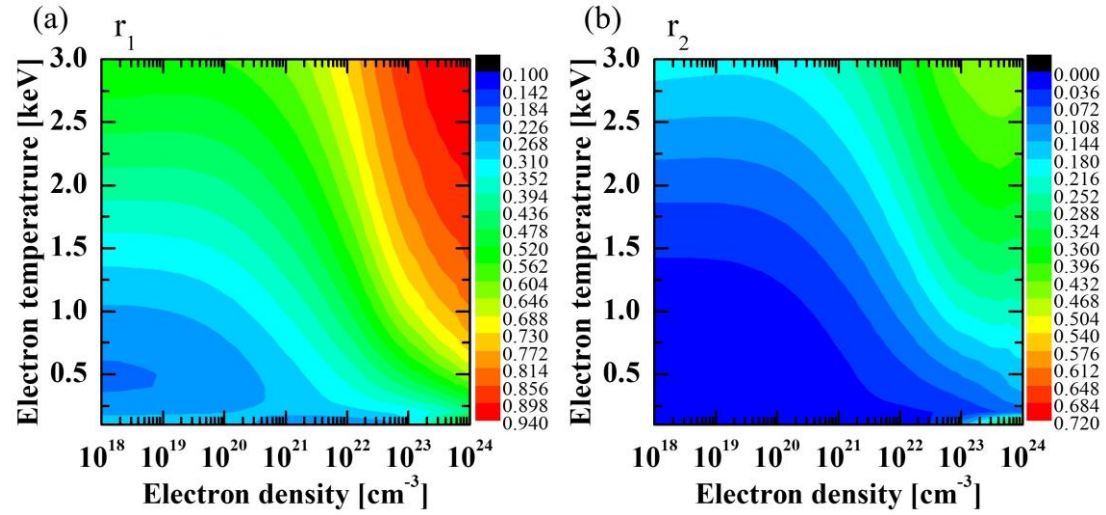


Figure 3.21 The x-ray power ratios with a fast electron fraction of 30% obtained from the FLYCHK code. (a) and (b) are the first and second ratios.

The reason for the change in the low-temperature range can be found in x-ray spectra. Figures 3.22 show the spectra with fast electron fractions of 1% and 5% when the electron density is 10^{18} cm^{-3} . When the fast electron fraction is 1%, the continuum and K -shell radiations are relatively intense when electron temperatures are 0.1 and 0.2 keV, as shown in Fig. 3.22(a). Due to the low electron temperature, there are few high-energy electrons in bulk plasma to generate high-energy continuum and K -shell radiations. Therefore, the influence in the spectrum by the fast electrons is relatively large and decreases as the high-energy electrons of the bulk plasma increase by rising the electron temperature. On the other hand, higher fast electron fractions rather enhance L -shell radiation, resulting in relatively weaker high-energy radiations, as shown in Fig. 3.22(b).

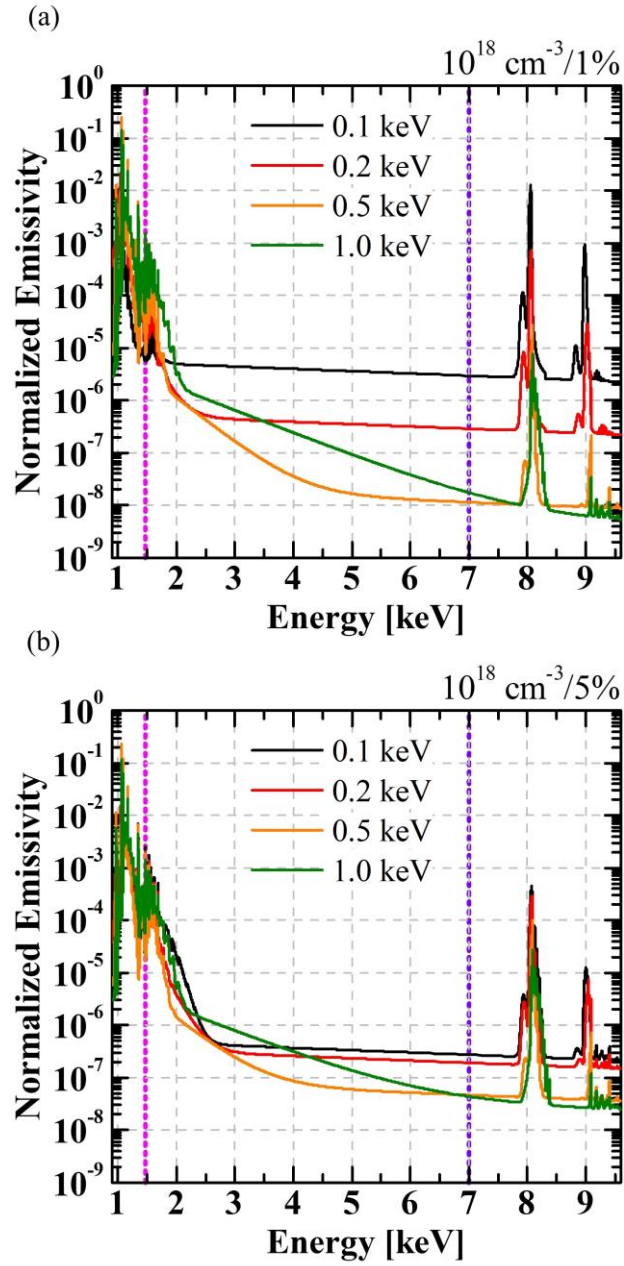


Figure 3.22 Synthetic spectra with the fast electron fractions of (a) 1% and (b) 5%. A electron density is 10^{18} cm^{-3} and electron temperatures are 0.1 (black line), 0.2 (red line), 0.5 (orange line), and 1.0 keV (green line).

As the electron density of the bulk plasma increases, the change in the spectrum tends to be different. When the electron density is 10^{21} cm^{-3} , the L -shell radiations become stronger due to the increased density, relatively reducing the effect of fast electrons; thus, the ratios at low temperature are smaller than those of the lower electron density case, as shown in Fig. 3.23(a). when the electron density increases to 10^{23} cm^{-3} , the continuum radiations become stronger and the ratios increase again, as shown in Fig. 3.23(b). In addition, as in the case of electron density of 10^{18} cm^{-3} , the higher the fast electron fraction, the slower the rapid increase in the ratios at the low temperature, as shown in Fig. 3.18 to 3.21 and Fig. 3.24. The complicated changes in x-ray power ratios allow fast electron fractions to be determined by the plasma parameter estimation process.

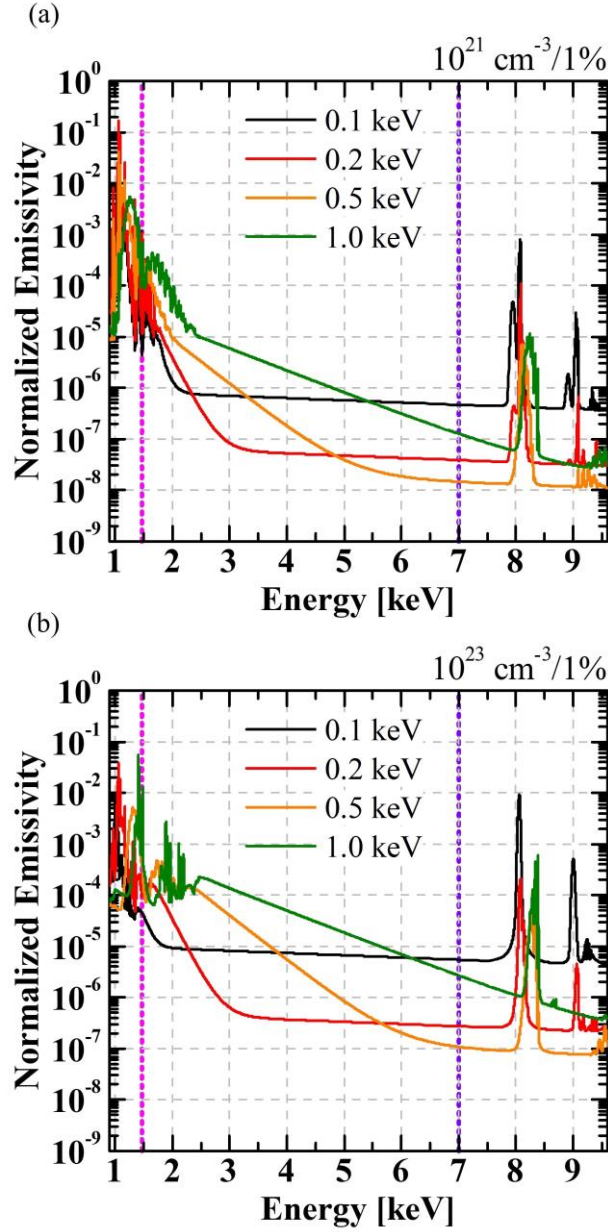


Figure 3.23 Synthetic spectra with electron densities of (a) 10^{21} cm^{-3} and (b) 10^{23} cm^{-3} . Fast electron fraction is 1% and electron temperatures are 0.1 (black line), 0.2 (red line), 0.5 (orange line), and 1.0 keV (green line).

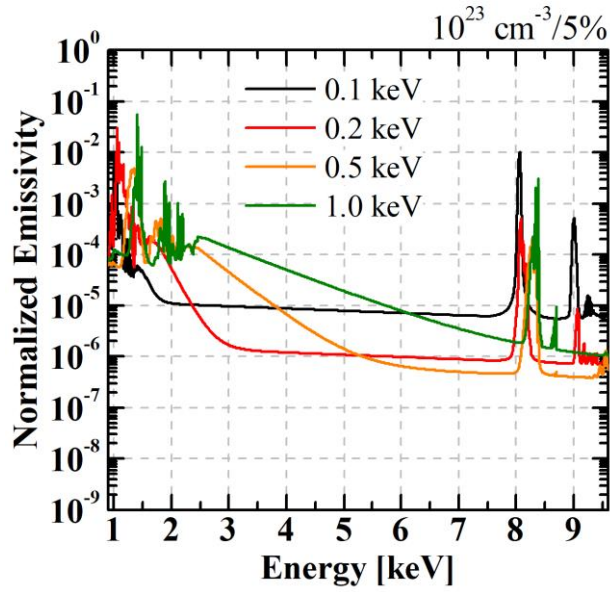


Figure 3.24 Synthetic spectra with an electron density of 10^{23} cm^{-3} . Fast electron fraction is 5% and electron temperatures are 0.1 (black line), 0.2 (red line), 0.5 (orange line), and 1.0 keV (green line).

3.2.3. Plasma parameter estimation and the process of analyzing x-ray data

We analyze the changes in the x-ray power ratios according to the plasma parameters. In the absence of fast electrons, the ratios increased according to the electron temperature and the electron density. Since each ratio has a different rate of increase, we can infer the electron temperature and the electron density from the difference in these ratios. The presence of the fast electrons increases the x-ray power ratio and makes more complex changes in the low-temperature range. These changes in the ratios by the fast electrons allow us to determine its fractions as well.

From the reconstructed spectra of synthetic ones by the LS method, the differences between the spectra with different parameters are also clearly observed, as shown in Fig. 3.25. Figure 3.25 (a) shows an increase in the K -shell radiation by electron temperatures at the same electron density; Figure 3.25 (b) shows an increase in the L -shell and K -shell radiations by electron densities at the same electron temperature. However, in both cases, the increase in the continuum radiation is not clearly shown, which is believed to be because the intensity of the continuum radiation is too small compared to the intensity of line radiation. Figures 3.25 (c) and (d) are spectra with fast electrons, and these are similar ones with results estimated from experimental results to be introduced later. Figure 3.25 (c) shows spectra of low electron density and electron temperature and high electron density and electron temperature with a fast electron fraction of 1%. the L -shell and K -shell radiations are

reconstructed similarly to those of the synthetic spectrum. There are errors in the reconstruction of the continuum radiations with low electron density and electron temperature, whereas the reconstruction results of the continuum radiations with high electron density and electron temperature are similar to those in the synthetic spectrum. Figure 3.25 (d) shows the spectra with the electron density of 10^{23}cm^{-3} and a high fast electron fraction. As in the previous case, the line radiations are reconstructed similar to those of the synthetic spectrum, and there are errors in the reconstruction of continuum radiations. In conclusion, the reconstruction of the line radiations is successfully performed; however, there are errors in the reconstruction of the continuum radiation. This is due to the small intensity of the continuum radiation, thus if the continuum is intense, the reconstruction is successfully performed. On the other hand, as the continuum is weak, the effect on the x-ray power ratios decreases, so the errors in the reconstruction of the continuum do not significantly affect the plasma parameter estimation. Therefore, the plasma parameters can be estimated by comparing the measured spectrum with the calculated one, even if the reconstruction of the continuum radiation is not accurate.

However, it should be clear that although there are several factors to be considered in constructing the synthetic x-ray data and measuring x-rays, we only take into account the simple situation; thus, we estimate possible plasma parameters, not the exact values. For example, the size and spatial distribution of plasma affect the spectrum and several plasmas can be present simultaneously for a

short time.[5, 8, 24] However, we measure an integrated spectrum for space. Therefore, we can say that we estimate effective plasma parameters. In addition, we assume the distribution of fast electrons as Maxwellian; since the fast electron distribution in the X-pinch is unknown, that makes uncertainty in plasma parameter estimation.

As a result, we construct a process of x-ray data analysis by combining x-ray measurement using the filtered AXUV diode array introduced in Section 3.1 and the plasma parameter estimation from the pre-calculated x-ray database. A schematic diagram of the process is shown in Fig. 3.26.

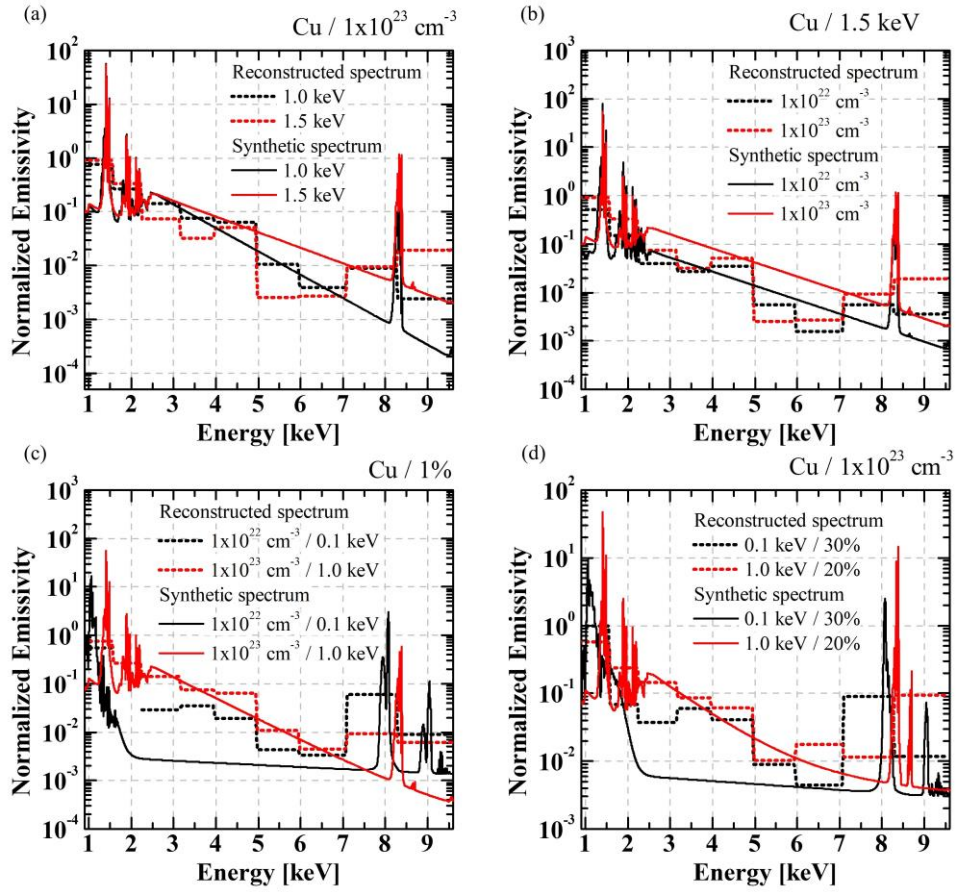


Figure 3.25 Reconstructed (solid) and synthetic spectra (dotted) with various plasma parameters. (a) electron temperatures are 1.0 (black) and 1.5 keV (red) with an electron density of 10^{23} cm^{-3} , (b) electron densities are 10^{22} cm^{-3} (black) and 10^{23} cm^{-3} (red) with electron temperature of 1.5 keV, (c) electron densities and temperatures of 10^{22} cm^{-3} and 0.1 keV (black) and 10^{23} cm^{-3} and 1.0 keV (red) with fast electron fraction of 1%, (d) electron temperatures and fast electron fractions of 0.1 keV and 30% (black) and 1.0 keV and 20% (red) with an electron density of 10^{23} cm^{-3}

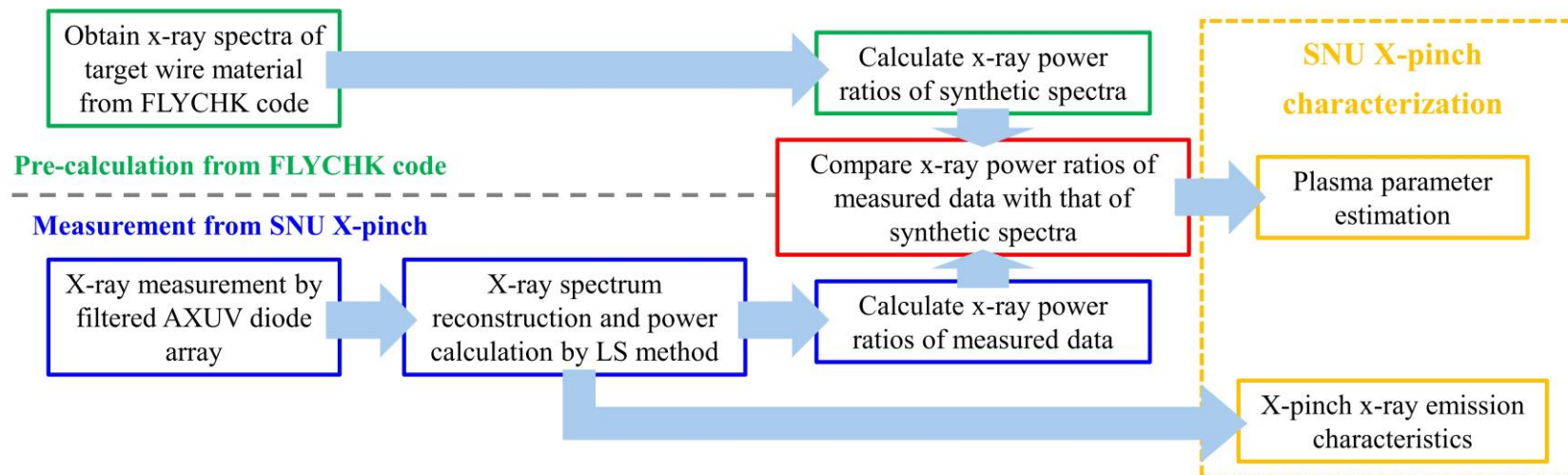


Figure 3.26 A schematic diagram of the process of analyzing x-ray data

Chapter 4. Time-resolved x-ray spectrum measurement

4.1. Two copper wires slow X-pinch

The Cu wires X-pinch experiments are conducted on SNU X-pinch. Cu wires with thicknesses of 25, 30, and 40 μm are used for a two-wire X-pinch load. The results of 25 μm -thick Cu wire load are introduced in this section, and the results of thicker wires loads are introduced in the following section. The capacitor bank is charged up to 50 and 55 kV; the maximum currents are 100 and 110 kA and the current rise rates are 0.197 and 0.214 kA/ns at each charging voltage. Figures 4.1 show typical x-ray signals of Cu wires X-pinch at each charging voltage. Multi x-ray peaks are generated in all shots and x-ray emission times of 50 and 55 kV cases are 69 and 87 ns, respectively. The results follow the typical x-ray emission properties of the slow X-pinch mentioned above. We divide the x-ray peaks into three bursts, (1), (2), and (3), as shown in Figs. 4.1. The first bursts rise quickly and are maintained for a relatively short time; the second bursts rise relatively slowly and are maintained for a long time, and the third bursts are relatively weak, releasing successively after the second bursts. Analysis of the x-ray peaks and plasma parameter estimation are performed for these three bursts.

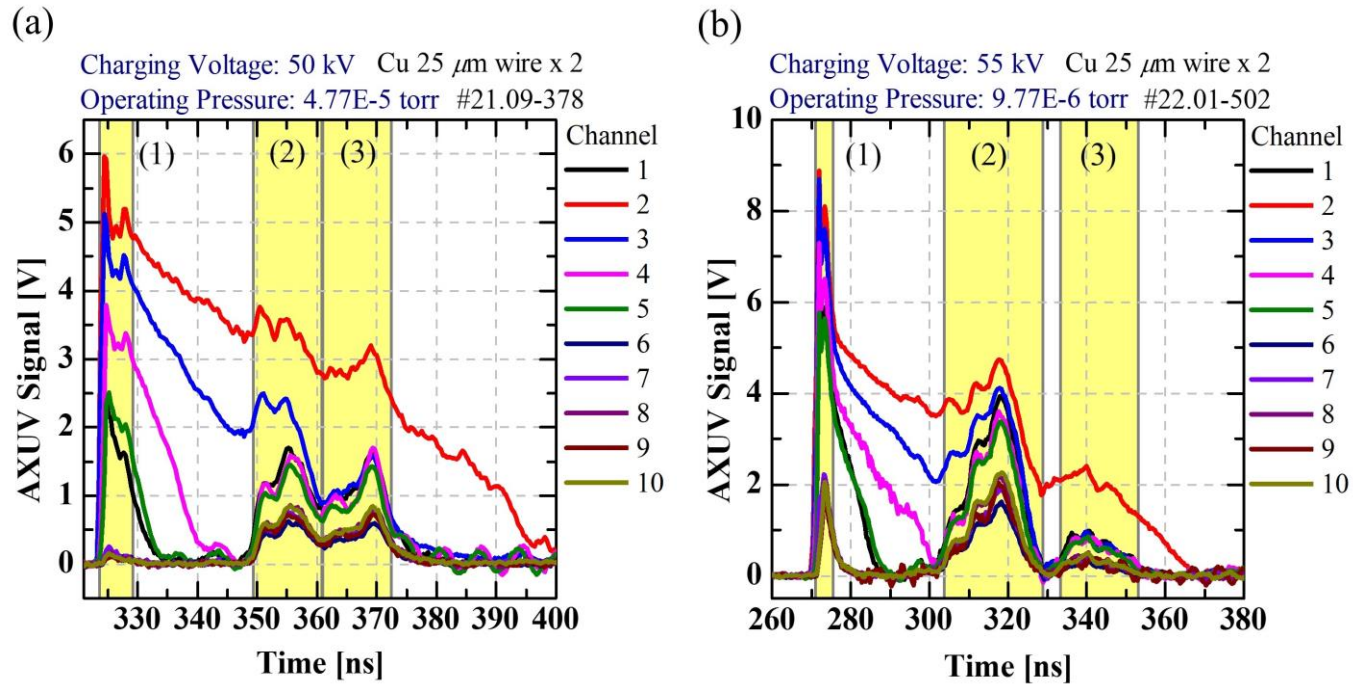


Figure 4.1 Typical x-ray signals of two Cu wires X-pinchs with charging voltages of (a) 50 and (b) 55 kV. The yellow areas indicate ranges of three bursts of x-rays, (1), (2), and (3).

Plasma parameters are estimated by comparing the x-ray power ratios pre-calculated from the FLYCHK code with those calculated from the x-ray signals measured by the filtered AXUV diode array. An example of plasma parameter estimation from the first peak of the 50 kV case is described in Figs. 4.2 and 4.3. Differences in the pre-calculated and measured x-ray power ratios are calculated and plasma parameters with a difference of less than 10% are plotted, as shown in Fig. 4.2. Since the differences in each power ratio show different slopes, an area with small differences in two power ratios can be specified, as shown in Fig. 4.3. Ones are obtained for all fast electron fractions, and the point with the smallest difference is found; the plasma parameters at a specific time are determined from it. The plasma parameter estimation is performed with a time step of 0.32 ns, which is one of x-ray signal measurement.

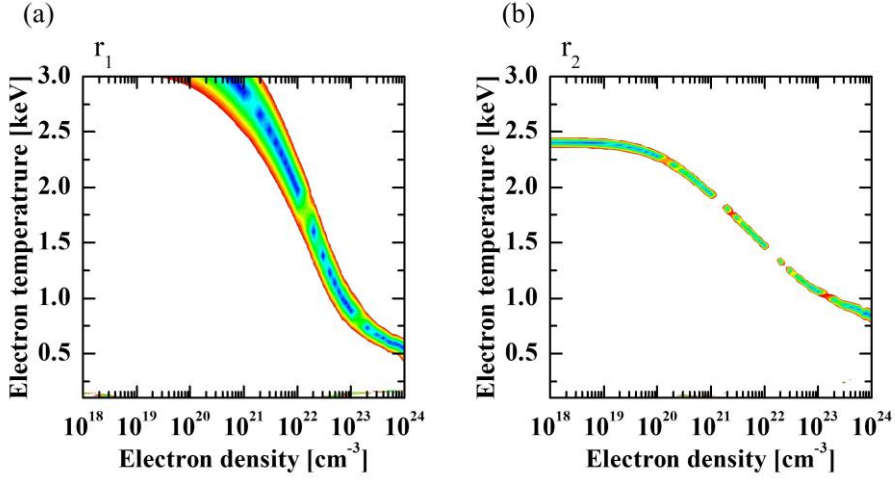


Figure 4.2 An example of a comparison of the x-ray power ratios from the first peak of 50 kV case. (a) and (b) show plasma parameters of the first and the second ratios with errors less than 10%, respectively.

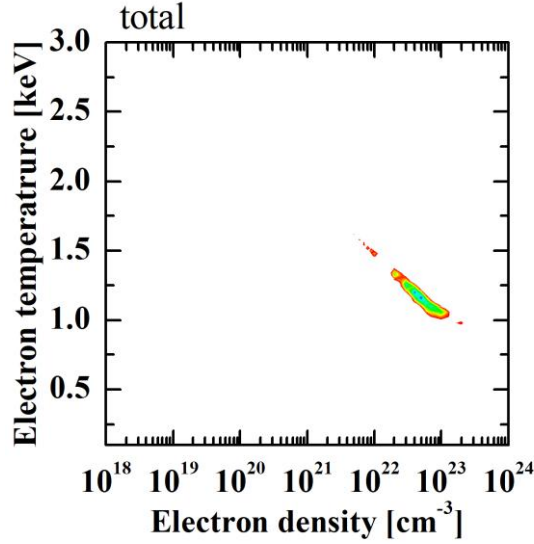


Figure 4.3 An example of a comparison of the x-ray power ratios from the first peak of 50 kV case. It shows plasma parameters with averaged errors of the x-ray power ratios less than 10%.

4.1.1. The results of the first burst

Table 4.1, Figures 4.4 and 4.5 show the estimated plasma parameters of the first burst (1) in the x-ray signals of 50 and 55 kV cases shown in Figs. 4.1. Channels 1, 2, and 10 are plotted together, and the channels measure x-rays with energies of more than 1.6, 0.86, and 4.3 keV, respectively. Channel 10 measures only the continuum and K -shell radiation of the Cu plasma spectrum; we consider its signal to be representative of HXR because the K -shell radiation emitted in the energy range of above 7 keV is much stronger than the continuum radiation in its measurement range. Plasma parameters estimated from peak-integrated powers are also presented to help identify the trend of plasma parameters between x-ray peaks.

Table 4.1 Estimated electron densities, electron temperatures, and fast electron fractions of the first bursts of the 50 kV and the 55 kV cases.

*For 5 ns (1)	50 kV	55 kV
n_e [cm^{-3}]	$\sim 6 \times 10^{21} - 1 \times 10^{23}$	$\sim 7 \times 10^{22} - 1 \times 10^{24}$
T_e [keV]	$\sim 0.65 - 1.49$	$\sim 0.96 - 1.5$
f [%]	$\sim 0 - 3\%$	$\sim 3 - 20\%$

In the 50 kV case, three consecutive x-ray peaks are emitted for about 5 ns. Channels 1 and 2, which can measure low-energy x-rays, produce the largest signal in the first x-ray peak. On the other hand, channel 10, which measures x-rays with relatively higher energy, produces very small signals, thus its signal is multiplied by 10 times in Fig. 4.4. From that, it can be seen that little continuum and K -shell radiations are released. Table 4.2 shows the plasma parameters of the three x-ray peaks which are the same as peak-integrated parameters shown in Fig. 4.4. Electron densities increase rapidly with the rise of the x-ray signals and then slightly increased from 5×10^{22} to $9 \times 10^{22} \text{ cm}^{-3}$. Electron temperatures are estimated to be about 1.16 keV at the first peak and gradually decreased to about 0.67 keV at the last peak. Fast electron fractions are estimated to be around 1%. A few fast electrons are consistent with the low signal of channel 10.

Table 4.2 Estimated electron densities, electron temperatures, and fast electron fractions from peak-integrated x-ray powers of the first burst of 50 kV case

50 kV	1st peak	2nd peak	3rd peak
$n_e \text{ [cm}^{-3}\text{]}$	$\sim 5 \times 10^{22}$	$\sim 9 \times 10^{22}$	$\sim 9 \times 10^{22}$
$T_e \text{ [keV]}$	~ 1.16	~ 0.86	~ 0.67
$f \text{ [%]}$	~ 1	~ 1	~ 0

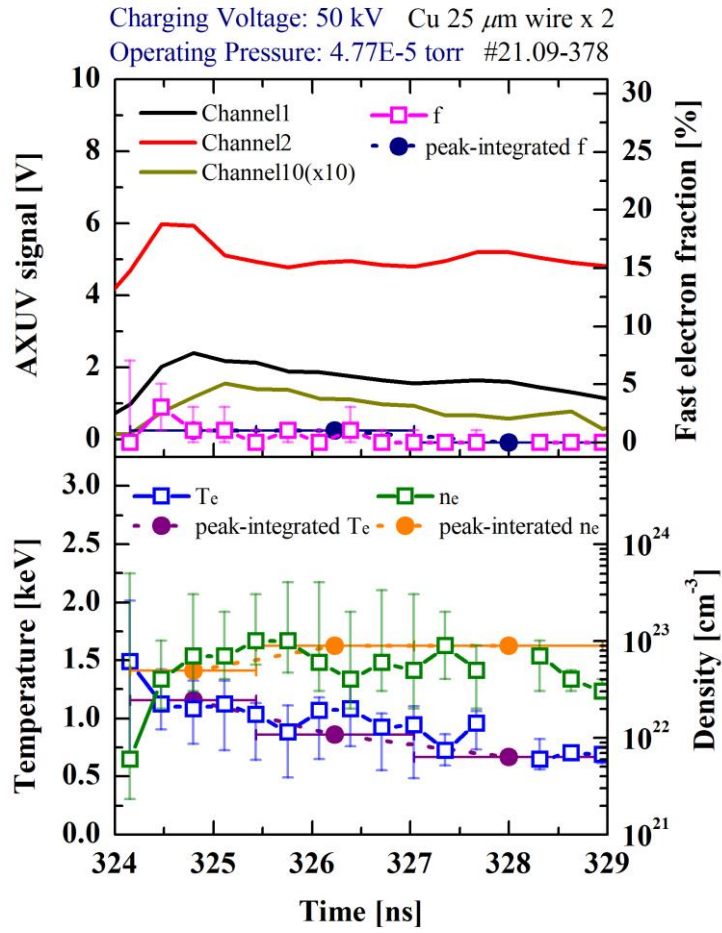


Figure 4.4 The signals of channels 1, 2, and 10 and the time evolution of estimated electron densities, electron temperatures, and fast electron fractions for the first burst of the 50 kV case. Estimated plasma parameters of three x-ray peaks from peak-integrated x-ray powers are plotted together.

In the case of 55 kV, two x-ray peaks stronger than those of the 50 kV case are released, and the intensity of channel 10 is much higher. Plasma parameters are also higher, as shown in Table 4.1. In particular, the fast electron fraction increase from 3% to 20%, as shown in Fig. 4.5; thus, there appears to be strong electron beams. The time-varying characteristics of plasma parameters are also different from those of the 50 kV case. Contrary to the 50 kV case, the electron temperature continues to increase after the first peak, while the electron density decreases, as shown in Fig. 4.5. This may be due to the increase of the energy deposited in the plasma by the higher charging voltage or the generation of electron beams.

The first peak and the second peak show different characteristics. At the first peak, the signals of channels 1 and 2 rise rapidly, while the signal of channel 10 is small and rises slowly. At the second peak, signals rise relatively slowly and the signal of channel 10 peaks. Fast electron fraction is about 12% at the second peak, while it is about 3% at the first peak. The electron temperature decreases rapidly as the fast electron fraction increases at the second peak. This is because the energy deposited on the plasmas decreases as a larger fraction of fast electrons transfer more energy.[24]

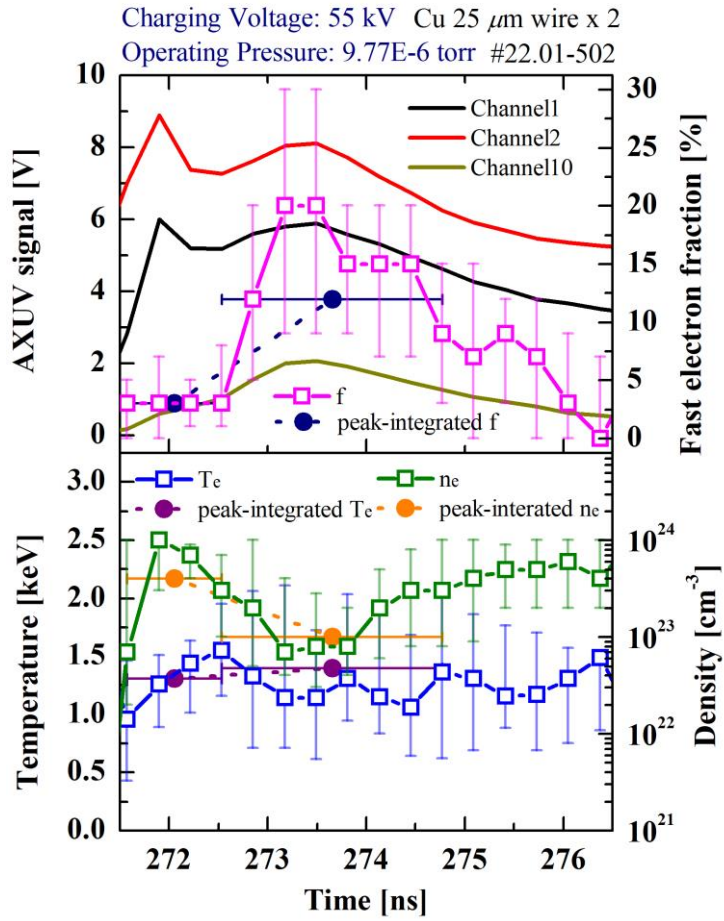


Figure 4.5 The signals of channels 1, 2, and 10 and the time evolution of estimated electron densities, electron temperatures, and fast electron fractions for the first burst of the 55 kV case. Estimated plasma parameters of two x-ray peaks from peak-integrated x-ray powers are plotted together.

Table 4.3 Estimated electron densities, electron temperatures, and fast electron fractions from peak-integrated x-ray powers of the first bursts of the 55 kV case

55 kV	1st peak	2 nd peak
n_e [cm^{-3}]	$\sim 4 \times 10^{23}$	$\sim 1 \times 10^{23}$
T_e [keV]	~ 1.31	~ 1.4
f [%]	~ 3	~ 12

Considering the x-ray signals and estimated plasma parameters, the first burst can be divided into two kinds of x-rays. The x-ray peaks of the 50 kV case and the first x-ray peak of the 55 kV case are composed of strong SXR and weak HXR; they are the first bursts that rise rapidly. Thus, they may be thermal radiations emitted from the HSs at the HS formation phase and their plasma parameters can be said to be HS parameters. On the other hand, the second x-ray peak of the 55 kV case rises relatively slowly and peaks at the same time as the harder x-ray; the fast electron fraction is high and the HXR is relatively strong. Therefore, it may be electron beam-generated x-rays.[6–9, 18, 21] Considering that it is emitted after about 1 ns from the first x-ray peak emitted by HS, the x-rays should be generated by the interaction between electron beams formed after neck disruption and hot dense plasma at the neck disruption phase.[6, 7]

The results of the first burst show the typical dynamics of the

X-pinch[1, 6, 52] In addition, the estimated HS parameters are similar to those measured in previous studies.[22, 24, 53] Consequently, it can be said that the new diagnostics estimates reasonable plasma parameters.

4.1.2. The results of the second burst

The second bursts are emitted 25–30 ns after the first x-ray peak. They show different characteristics from the first bursts, as shown in Figs. 4.6, 4.7, and Table 4.4. The rise of the x-ray signals is slower and emission time is much longer than those of the first bursts. The signal of channel 2 is lower than that of the first burst, but the signal of channel 10 is similar or higher. This means that more HXR is released. Correspondingly, the fast electron fractions rise to 30% and are maintained for several ns. The electron densities are similar to those of the first bursts, but the electron temperatures are much lower. From the time characteristics of the second bursts, it can be inferred that x-rays are emitted by the interaction between cold dense plasma and long electron beams at the minidiode depletion phase. Previous studies have shown that, after the neck structure is completely depleted, the electron beams are accelerated between minidiode; they interact with the anode of minidiode, and generate x-rays.[6, 7]

Several notable features are shown in the time evolution of the plasma parameter. When channels 1 and 10 are generated, the fast electron fraction rises rapidly, and the increase is accompanied by an increase in electron density. Subsequently, minor peaks are observed

in the x-ray signals, and with the occurrence of them, the fast electron fraction repeats decrease and increase rapidly. From the fluctuations of the fast electron fraction, multiple accelerations of electron beams are expected. In addition, it is assumed that the acceleration is correlated with conditions of the bulk plasma in that it is accompanied by the increase of electron density and small fluctuations of electron temperature, as shown in Figs. 4.6 and 4.7. It is also noteworthy that the electron density, electron temperature, and electron beam density increase in proportion to the charging voltage.

Table 4.4 Emission time, estimated electron densities, electron temperatures, electron beam densities, and fast electron fractions of the second bursts of the 50 kV and the 55 kV cases.

(2)	50 kV	55 kV
Emission time [ns]	11	25
n_e [cm^{-3}]	$\sim 10^{21} - 10^{23}$	$\sim 10^{22} - 10^{24}$
T_e [keV]	$\leq 0.1 - 0.2$	$\leq 0.1 - 0.24$
$n_{e\text{-beam}}$ [cm^{-3}]	$\sim 10^{20} - 10^{22}$	$\sim 10^{20} - 10^{23}$
f [%]	$\sim 10 \rightarrow 30 \rightarrow 1$	

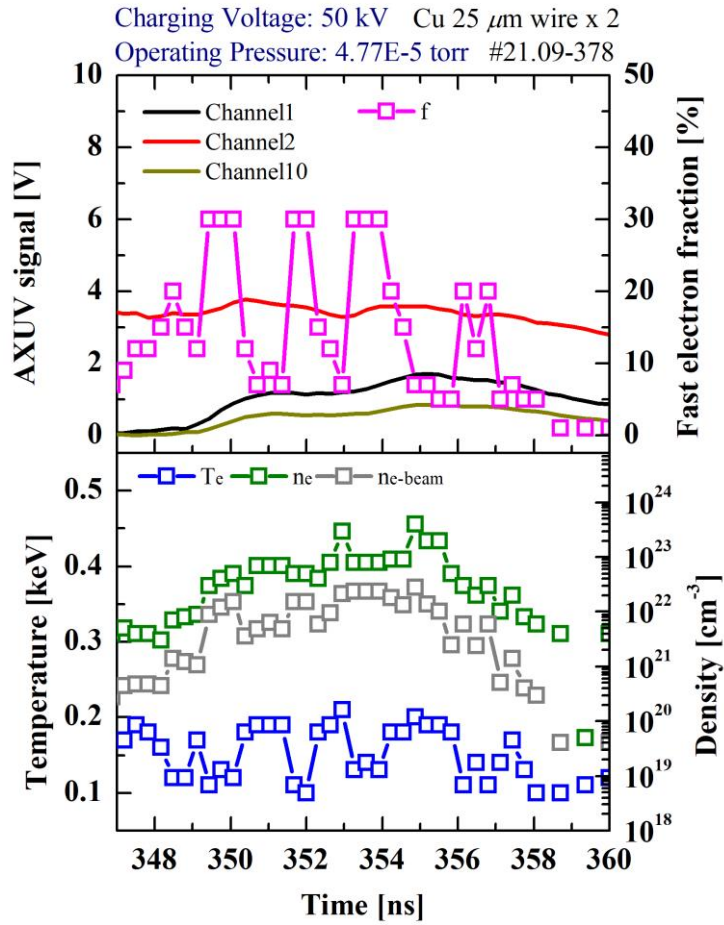


Figure 4.6 The signals of channels 1, 2, and 10 and the time evolution of estimated electron densities, electron temperatures, fast electron fractions, and electron beam densities for the second burst of the 50 kV case.

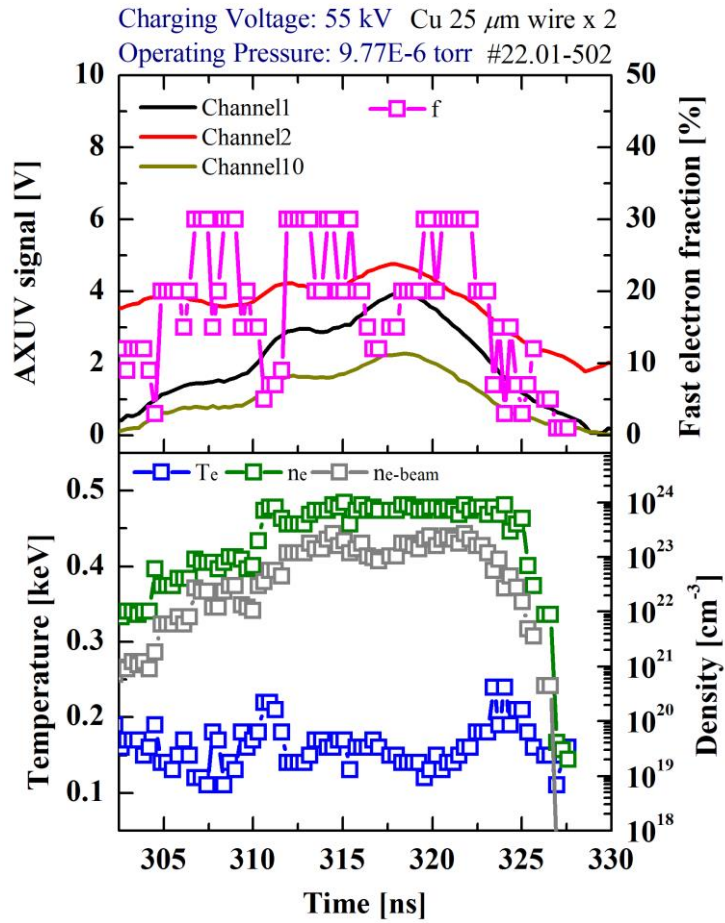


Figure 4.7 The signals of channels 1, 2, and 10 and the time evolution of estimated electron densities, electron temperatures, fast electron fractions, and electron beam densities for the second burst of the 55 kV case.

4.1.3. The results of the third burst

Plasma parameters of the third burst are shown in Figs. 4.8, 4.9, and Table 4.5. The third bursts are emitted for 11–20 ns immediately after the second bursts. The electron temperature is about 0.1 keV, and the electron density is much lower than that of the second burst. Unfortunately, the electron density of the third burst is difficult to be determined. For the first and second bursts, a region with low errors appears as a group by the plasma parameter estimation, as shown in Figs. 4.3, 4.10 and 4.11. For the third burst, a region with low errors appears as two groups, as shown in Figs 4.12 and 4.13. However, the electron density is generally estimated to be about $\sim 10^{21} \text{ cm}^{-3}$, which is sufficient to say that the electron density is much lower than that of the second burst.

The fast electron fraction and electron beam density fluctuate along minor x-ray peaks, and their magnitude is smaller than those of the second burst. On the other hand, the electron density remains almost constant. From the results, it can be deemed that the x-rays are also generated by interaction with long electron beams and cold dense plasma at the minidiode depletion phase. However, unlike the second burst, the conditions of bulk plasma have little change.

Table 4.5 Emission time, estimated electron densities, electron temperatures, electron beam densities, and fast electron fractions of the third bursts of the 50 kV and the 55 kV cases.

(3)	50 kV	55 kV
Emission time [ns]	11	20
n_e [cm^{-3}]	$\sim 10^{21} - 10^{22}$	
T_e [keV]	$\leq 0.1 - 0.16$	
$n_{e\text{-beam}}$ [cm^{-3}]	$< 10^{19} - 10^{21}$	
f [%]	$\sim 1 \rightarrow 7$	

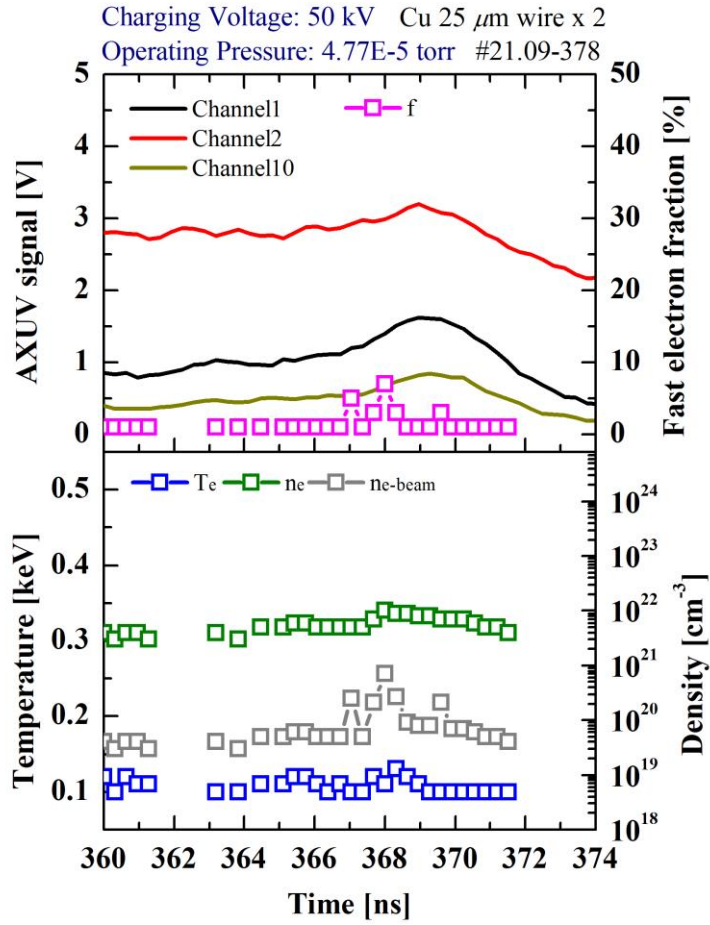


Figure 4.8 The signals of channels 1, 2, and 10 and the time evolution of estimated electron densities, electron temperatures, fast electron fractions, and electron beam densities for the third burst of the 50 kV case.

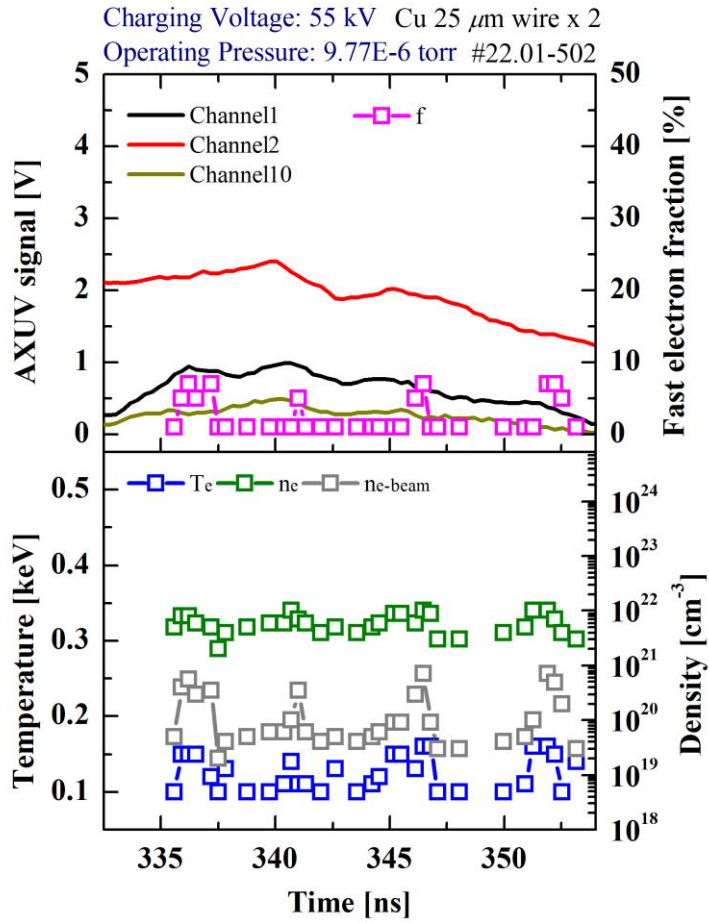


Figure 4.9 The signals of channels 1, 2, and 10 and the time evolution of estimated electron densities, electron temperatures, fast electron fractions, and electron beam densities for the third burst of the 55 kV case.

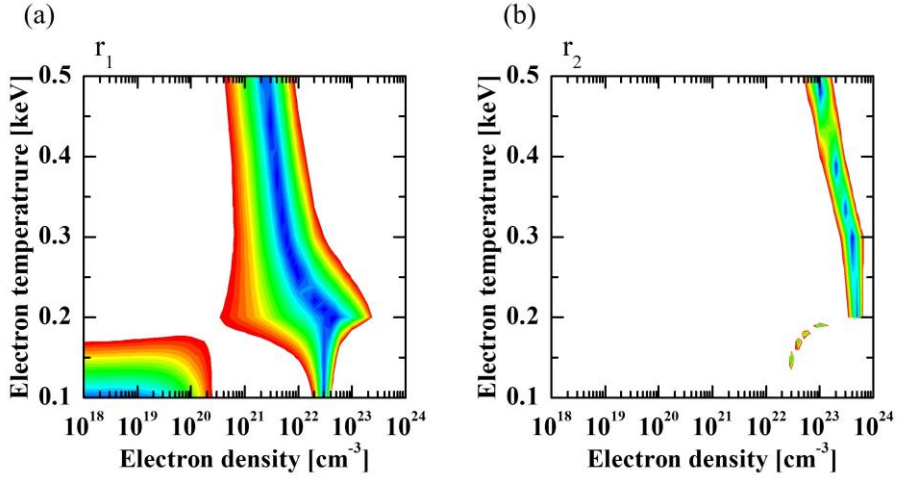


Figure 4.10 An example of a comparison of the x-ray power ratios from the second burst of 50 kV case. (a) and (b) show plasma parameters of the first and the second ratios with errors less than 15%, respectively.

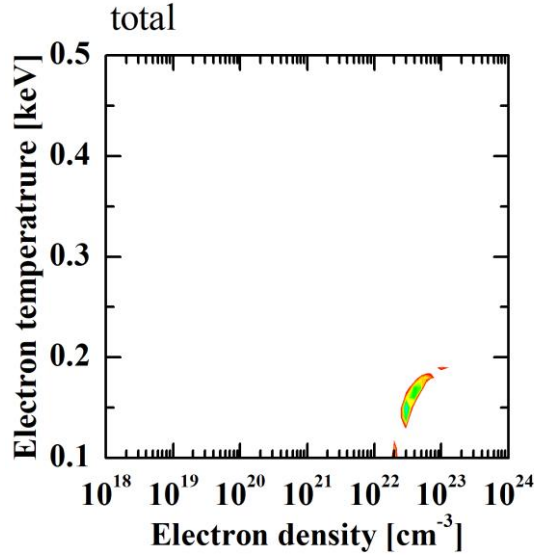


Figure 4.11 An example of a comparison of the x-ray power ratios from the second burst of 50 kV case. It shows plasma parameters with averaged errors of the x-ray power ratios less than 15%.

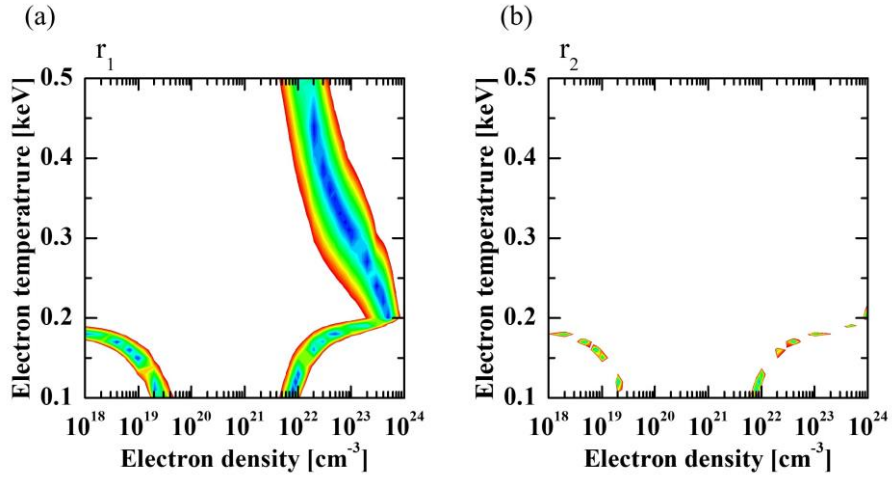


Figure 4.12 An example of a comparison of the x-ray power ratios from the third burst of 50 kV case. (a) and (b) show plasma parameters of the first and the second ratios with errors less than 15%, respectively.

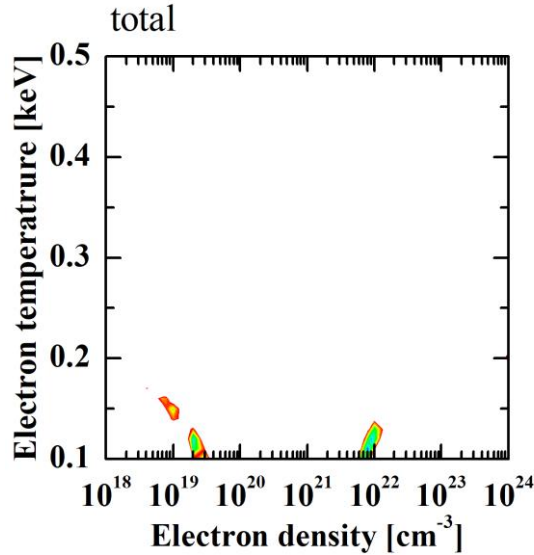


Figure 4.13 An example of a comparison of the x-ray power ratios from the third burst of 50 kV case. It shows plasma parameters with averaged errors of the x-ray power ratios less than 15%.

We analyzed the x-ray peaks of Cu wires slow X-pinch divided into three bursts and obtained the three different conditions of the plasmas emitting each burst. The first burst consists of x-ray peaks emitted at the HS formation and the neck disruption phases. The HS parameters are obtained from the first peaks, with a high electron density of about 10^{23} cm^{-3} and a high electron temperature of more than 1 keV. In the second peak, the fast electron fraction is high due to the short electron beam formed during the neck disruption phase. Both the second and the third burst are expected to be formed by the long electron beam at the minidiode disruption phase; however, they are released from plasmas with different properties. In particular, in the second burst, the electron density increases rapidly similarly to that of HS; on the other hand, the relatively low electron densities remain almost constant in the third burst. The bursts produced by the long electron beams cause the multi bursts and the emission time to increase after the HS bursts. That is, whether or not these x-ray bursts are formed is an important factor in improving the time characteristics of the slow X-pinch. Therefore, we analyze the x-ray burst under different Cu wires loads such as thicker Cu wires and insulated Cu wires in the following sections.

4.2. Thicker Cu wires slow X-pinch

Slow X-pinch experiments are performed using Cu wires with thicknesses of 30 and 40 μm thicker than the previous ones. Figures 4.14 show their x-ray signals with a charging voltage of 55 kV. As Cu wire becomes thicker, the number of x-ray bursts decreases, and the pinch time is delayed. In the case of the 30 μm -thick Cu wires load, two x-ray bursts are released in three shots out of ten shots, as shown in Fig. 4.14(a). For 40 μm -thick Cu wires load, a single x-ray burst is released and the pinch time is approximately 490 ns, close to the current peak time, as shown in Fig. 4.14(b); however, sometimes the x-ray burst is not emitted. The x-ray bursts of each load are analyzed through plasma parameter estimation.

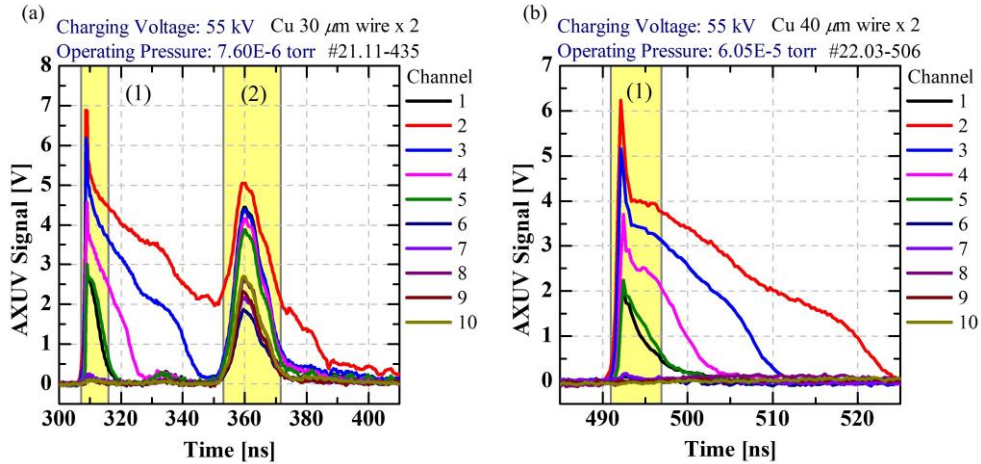


Figure 4.14 Typical x-ray signals of two (a) 30 and (b) 40 μm -thick Cu wires X-pinch with a charging voltage of 55 kV

Figure 4.15 shows the estimated plasma parameters of the first burst from the 30 μm -thick Cu wires X-pinch. The electron density and electron temperature of HS are about $9 \times 10^{22} \text{ cm}^{-3}$ and 1.11 keV, respectively, which are lower than those of the 25 μm -thick Cu wires X-pinch with the same charging voltage. In addition, considering the fast electron fractions remain low, an x-ray peak by a short electron beam does not seem to be formed. Therefore, the time characteristics of the x-ray signals are similar to that of the X-pinch with the 50 kV charging voltage.

Figure 4.16 shows the estimated plasma parameters of the second burst. A rapid increase in fast electron fractions and electron density is observed and their maximum values are similar to those of the 25 μm -thick Cu wires X-pinch. That is, it can be said that this second burst is formed by the same process as the previous ones. However, unlike in the previous cases, a minor x-ray peak is not clearly shown, thus fluctuations of fast electron fraction are also not clearly shown. From the analysis of the second burst, it is confirmed that the x-ray burst corresponding to the third burst in the previous cases is not emitted.

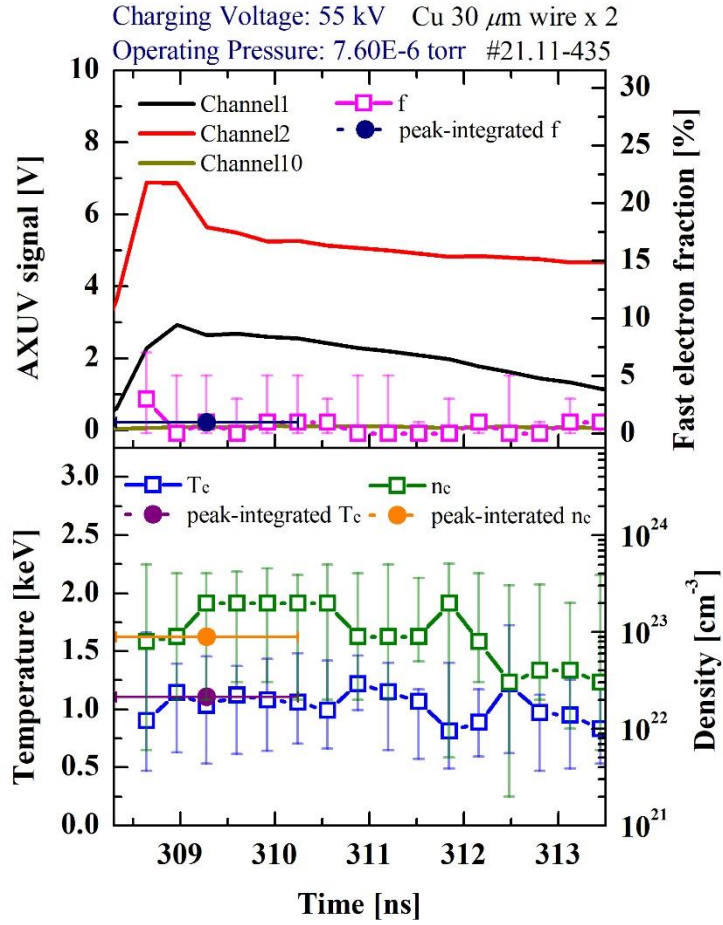


Figure 4.15 The signals of channels 1, 2, and 10 and the time evolution of estimated electron densities, electron temperatures, and fast electron fractions for the first burst of the 30 μm -thick Cu wires X-pinch. Estimated plasma parameters of two x-ray peaks from peak-integrated x-ray powers are plotted together

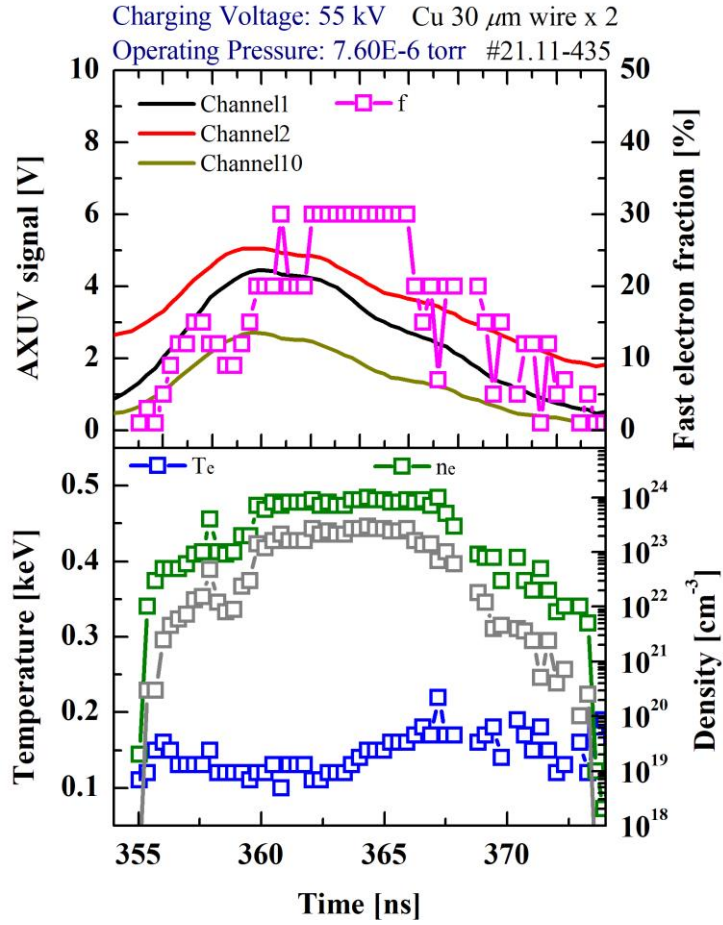


Figure 4.16 The signals of channels 1, 2, and 10 and the time evolution of estimated electron densities, electron temperatures, fast electron fractions, and electron beam densities for the second burst of the 30 μm -thick Cu wires X-pinch.

Figure 4.17 shows the estimated plasma parameters of a single burst from the 40 μm -thick Cu wires X-pinch. The electron density and electron temperature of HS are about $8 \times 10^{22} \text{ cm}^{-3}$ and 0.95 keV, respectively, and fast electron fractions remain low. Among the experiments with the charging voltage of 55 kV, the x-ray signals are measured to be the lowest. In addition, the second and third x-ray bursts are not emitted, and the generation of the x-ray burst by electron beams does not appear.

As a result, with an increase in wire thickness, it is observed that the electron density and electron temperature of HS decreased. In other words, the HS with the highest energy is generated at the 25 μm -thick wire load, which means that it matches the power system best in terms of an energy conversion efficiency. On the contrary, as the thickness of Cu wire increases, the number of the electron beam-generated x-ray peaks and the emission time decrease. As an x-ray source, it can be said that the temporal resolution is improved.

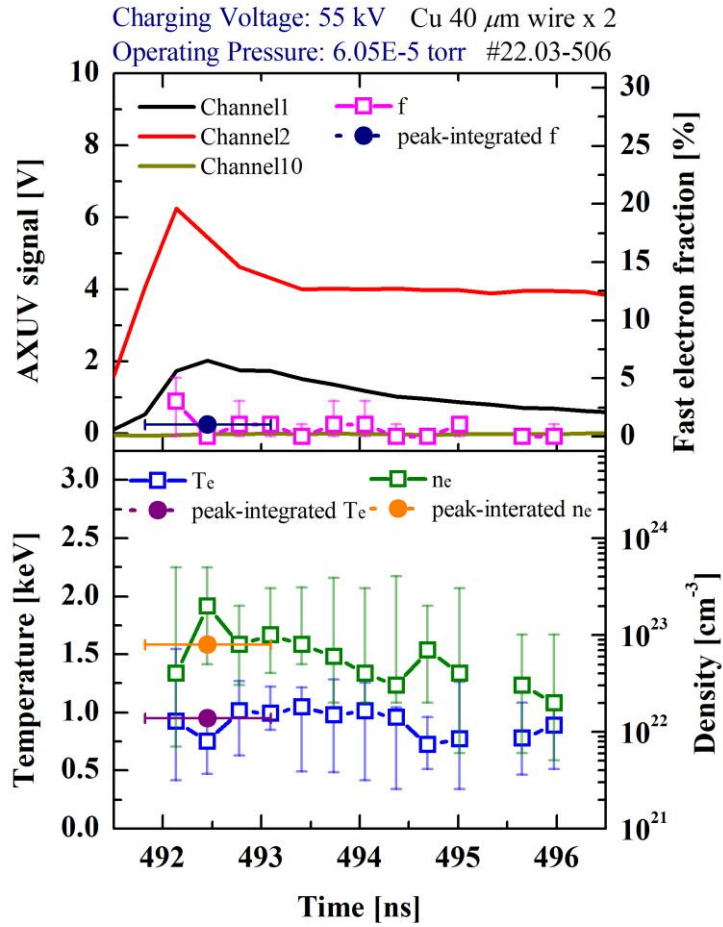


Figure 4.17 The signals of channels 1, 2, and 10 and the time evolution of estimated electron densities, electron temperatures, and fast electron fractions for the first burst of the 40 μm -thick Cu wires X-pinch. Estimated plasma parameters of two x-ray peaks from peak-integrated x-ray powers are plotted together

4.3. Insulated Cu wires X-pinch

The Insulated wires load has the potential to improve the performance of slow X-pinch as an SXR source. Insulated wire load was suggested as a way to improve the quality of implosions that affect x-ray production[54] and mainly studied in single wire explosions[55–58] and Z-pinches.[59, 60] According to the results of single wire explosions, insulated wire load increases the energy deposited on wires during the wire heating phase and reduces wire surface vaporization, resulting in suppressing the core-corona structure, increasing wire expansion velocity, and converting most wire materials into plasma. As a result, the use of the insulated wire increased the symmetry of the implosion, which was expected to increase the quality of the implosion of the Z-pinch. [54–58] When insulated wire array was applied to the Z-pinches, although x-ray power was similar or reduced compared to bare wire array Z-pinches, the multi bursts and the emission time of x-ray pulses were reduced.[54, 59, 60]

Since the reduction of multi bursts and x-ray emission time helps to improve the temporal resolution of the slow X-pinch as an x-ray source, the previous results in Z-pinch make it expected that the use of insulated wires may improve the performance of the slow X-pinch. However, there are few studies on insulated wire load on the X-pinch. Meanwhile, most of the X-pinch load configurations have been studied to suit higher generator currents.[14] If the insulated wire load shows the advantages that appeared in the Z-

pinch experiments, it could be a good option in addition to two or four wires load on a small-scale X-pinch with the low and slow-rise current generator. Therefore, we conduct X-pinch experiments with insulated wires load and compare it with the results of bare Cu wires X-pinch.

Two Cu wires with a thickness of 25 μm with the polyimide insulation are used for the X-pinch load. The thickness of the insulation is an important factor because too thick insulation rather reduces energy deposited on wires. Therefore, we conduct preliminary experiments using Cu wires insulated with thicknesses of 2 μm and 5 μm . As a result, in the case of the 5 μm -thick insulation, an x-ray burst was not emitted with the charging voltage of 55 kV; thus, we choose the former for the wire load. The typical x-ray signals from the insulated Cu wires X-pinch with a charging voltage of 55 kV are shown in Fig. 4.18. Unlike the x-ray signals of the bare Cu wires X-pinch with the same wire thickness, the second and third bursts are not emitted in the insulated Cu wires X-pinch, and only a strong single x-ray peak is emitted. For most shots, x-ray peaks generated by the long electron beam are not emitted, thus the emission of harder x-rays (channels 6–10) and the number of x-ray peaks are reduced as compared with the previous result. Consequently, the electron beam-generated x-rays are suppressed by using the insulated wires load.

Plasma parameters estimated in the yellow area of Fig. 4.18 are shown in Fig. 4.19. The electron density of the HS is about $3 \times$

10^{23} cm^{-3} , the electron temperature is about 1.18 keV, and the fast electron fraction is about 1%. The electron density is similar to that of 25 μm Cu wires load with the charging voltage of 55 kV, but the electron temperature and fast electron fraction are similar to those of the 50 kV case. Although the charging voltage is 55 kV, the time-varying characteristics of electron temperature and electron density are similar to those of the 50 kV case. Therefore, the time-varying characteristics are greatly affected by the generation of short electron beams, while they are not affected by wire insulation. Consequently, the wire insulation makes a significant change in x-ray emission by the long electron beam in the minidiode depletion phase rather than x-ray emission in the HS formation and the neck disruption phase.

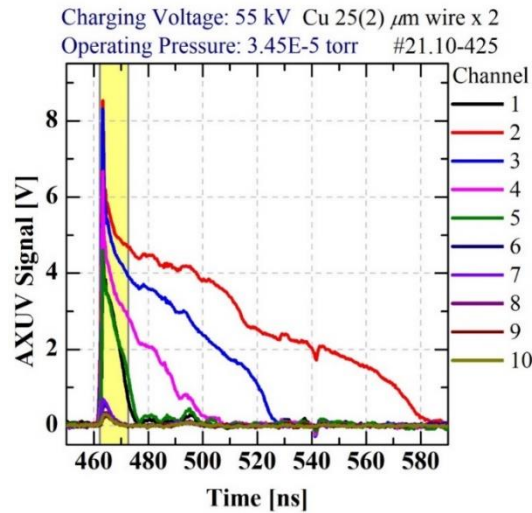


Figure 4.18 Typical x-ray signals of the two insulated Cu wires X-pinch with a charging voltage of 55 kV. The yellow area indicates a range of the first burst.

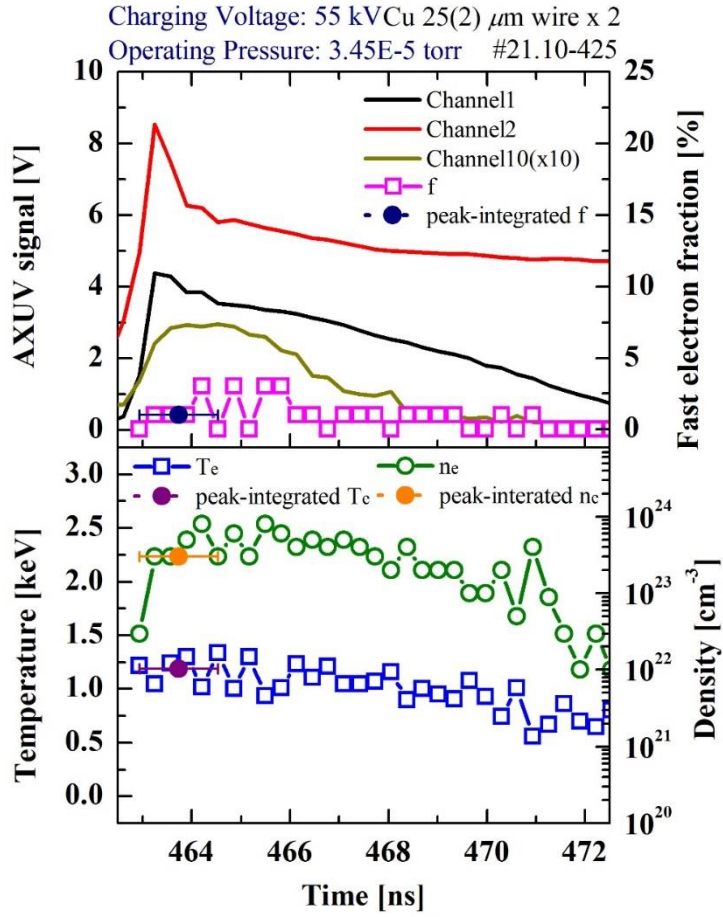


Figure 4.19 The signals of channels 1, 2, and 10 and the time evolution of estimated electron densities, electron temperatures, and fast electron fractions for the first burst of the insulated Cu wires X-pinch. Estimated plasma parameters of the x-ray peak from peak-integrated x-ray powers are plotted together.

4.4. Summary and Discussion

We analyze the x-rays emitted from the two 25 μm -thick Cu wires X-pinchs and classify them into three bursts. In the first burst, 1–3 x-ray peaks occur for about 5 ns, and they are divided into thermal radiations at the HS formation phase and x-rays generated by short electron beams at the neck disruption phase. In the case of 50 kV, only the x-ray peaks expected to be emitted from HS exist; in the case of 55 kV, the first x-ray peak is emitted by HS and the second x-ray peak is generated by the short electron beam. The electron density, electron temperature, and fast electron fraction of HS are estimated higher at 55 kV case and they show different time-varying characteristics by the charging voltages. The estimated electron density and electron temperature of HS are similar to those measured in conventional X-pinchs.[23, 24, 26, 27] The electron beam-generated x-rays are generated after about 1 ns from the emission of the first x-ray peak. Considering that strong electron beams in the first burst are formed only in the case of 55 kV, the formation of electron beams is affected by the input power. Therefore, the characteristics of HS, the generation of electron beams, and input power may be correlated. The electron beam-generated x-rays of the first burst are inferred to be emitted by an interaction of short electron beams with hot dense plasma after disruption of the neck structure[6] In conclusion, the properties of the first burst are similar to those obtained in the study of conventional X-pinchs. In other words, the HS parameters and the

emission properties of the main x-ray burst of the SNU X-pinch with the slow-rise current generator are similar to those of conventional X-pinch.

The second and third bursts have a relatively high proportion of harder x-rays and are released for a longer time than the first burst. Both are inferred to be emitted by the interaction between cold plasma and electron beams generated at the minidiode depletion phase; however, there are significant differences in the time evolution of plasma parameters. The electron density of the second burst rises to a level similar to that of HS as fast electron fractions increase. Furthermore, fast electron fractions fluctuate from up to 30% to less than 10%. Namely, the electron beams undergo multiple accelerations and the parameters of the bulk plasma are affected by them. On the other hand, the electron density of the third burst is about 10^{21} cm^{-3} , which is much lower than that of the second burst. Fast electron fractions are also about 1% and their magnitude of fluctuation is much smaller; the parameters of bulk plasma remain almost constant, unlike those of the second burst. The difference may occur because the energy of electron beams of the third burst is not high enough to cause the parameters of the bulk plasma to rise. Therefore, the third burst may be emitted by the interaction between the remaining plasma and the relatively low-energy electron beam after the second burst. The characteristics shown in the x-ray signals of the second and third bursts are consistent with those of the long electron beam introduced in the previous study.[6] However, unlike the results of the previous study, they are divided into two

bursts. In particular, the increase in electron density with the acceleration of the electron beam is a remarkable result.

The X-pinch experiments with thicker Cu wires and insulated Cu wire loads are conducted and the results are compared. Table 4.6 shows the HS parameters, pinch time, and the kinds of x-ray bursts obtained from X-pinch experiments with the charging voltage of 55 kV. 25 μm -thick Cu wires X-pinch produce HS with the highest electron density and electron temperature. The thicker the wire, the less the electron beam generated x-ray bursts; the 40 μm -thick Cu wires X-pinch emits only the x-ray burst by HS. Insulated Cu wires X-pinch produce HS with parameters similar to those of the bare Cu wires X-pinch with the same wire thickness; however, its fast electron fraction is significantly less. It also releases only the first x-ray burst, like the 40 μm -thick Cu wires X-pinch. It is noteworthy that its pinch time is similar to that of the 40 μm -thick Cu wires X-pinch. Given that its HS parameters are similar to those of 25 μm -thick Cu wires X-pinch, the generation of x-ray burst by long electron beam may be associated with pinch time rather than with the HS formation process.

The mechanism of the formation of long electron beams and the rapid increase in electron density in the second burst is unclear. Indirect evidence for the rapid increase in the electron density is found in the current signal. As shown in Fig. 4.20, the current fluctuates at the time when the late-time x-ray peaks are emitted. This current fluctuation can be caused by rapid changes in plasma impedance, which is affected by electron temperature and electron

density. Therefore, the rapid increase in electron density by the electron beam may cause the current to fluctuate. However, the current signal is measured on the capacitor bank side, so other external factors can make the fluctuation. Thus, other evidence is still needed.

Table 4.6 HS parameters, pinch times, and kinds of x-ray bursts from different Cu wire loads with the charging voltage of 55 kV

Cu wire load [μm]	25	30	40	25 (+ 2)
n_e [cm^{-3}]	$\sim 4 \times 10^{23}$	$\sim 9 \times 10^{22}$	$\sim 8 \times 10^{22}$	$\sim 3 \times 10^{23}$
T_e [keV]	~ 1.31	~ 1.11	~ 0.95	~ 1.18
f [%]	~ 3	~ 1	~ 1	~ 1
Pinch time [ns]	272	308	492	463
X-ray bursts	1 st + 2 nd + 3 rd	1 st + 2 nd	Only 1 st	Only 1 st

We guess a possible scenario for the electron density increase from the results of this study. The First is the additional ionization of remaining materials or plasmas by the electron beam. In the X-pinch, electron beams with energy ranging from tens of keV to 1 MeV can be generated.[61] The high-energy electron beams may collide with remaining wire materials or ablated plasmas diffused from an anode and cause additional ionization, thereby forming a high-density plasma channel again. In particular, due to the slow process of the slow X-pinch, the time for diffusing ablated plasmas from an anode

is sufficient; thus, it fills a space where the electron beams proceed.[16] Second, due to the slow rise in current, high current is still being supplied even though tens of ns have passed since the pinch time, as shown in Fig. 4.20. Thus, late-time pinching or re-compression is likely to occur because of the current reconnection by high-energy electron beam and sufficient current. This late-time pinching has also been mentioned in previous studies.[8, 9] The scenario can explain why the long electron beam generated x-ray burst is not emitted in the 40 μm -thick and insulated Cu wires X-pinch. A reason inferred from x-ray signals is a delay of a pinch time. The first x-ray peak is emitted at about 272 ns in the 25 μm -thick Cu wires X-pinch with the charging voltage of 55 kV, whereas ones are released at about 492 and 463 ns in the 40 μm -thick and insulated Cu wires X-pinch, as shown in Table 4.6. It is possible that there is not enough time and current to form the long electron beam and reconnect a dense plasma channel, because they are pinched at a time when the current rise is almost finished. Therefore, plasma re-compression may not occur either. However, since it is difficult to determine a reason only with the x-ray signals, research comparing the post-pinch process of insulated and bare wires load will be conducted through x-ray and optical images in the future.

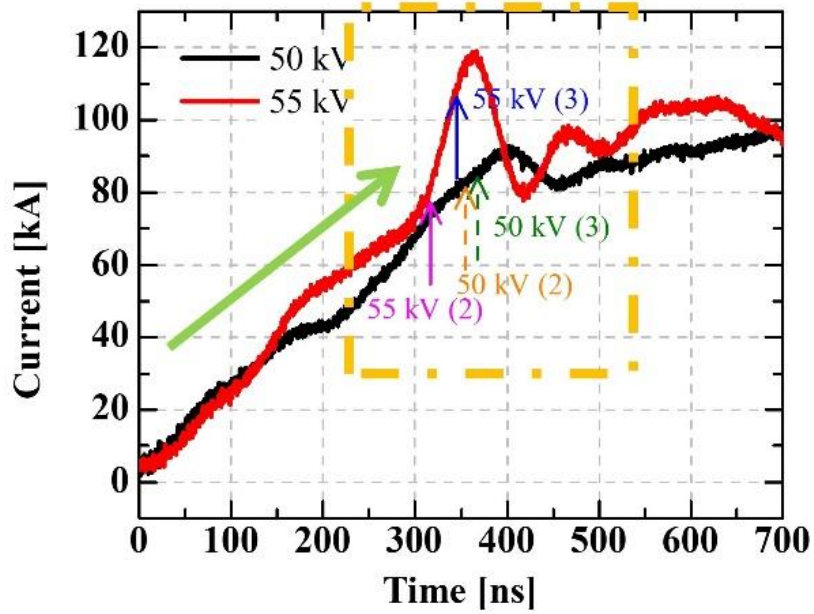


Figure 4.20 Current signals of the 50 (black line) and 55 kV (red line) charging voltage cases. Dash and solid arrows mark the second and the third bursts of the 50 and 55 kV cases, respectively.

Chapter 5. Conclusions and Future work

5.1. Conclusions

In this study, the fast time-resolved x-ray diagnostic system is developed for slow X-pinch dynamics research. The diagnostic system consists of the 10-channel filtered AXUV diode array for time-resolved spectrum measurement and the method for estimating plasma parameters from the discrete spectrum. Cu wires X-pinch experiments are conducted on the SNU X-pinch, and x-ray peaks are analyzed by using the developed diagnostic system; electron density, electron temperature, and fast electron fraction are estimated. The characteristics of slow X-pinch plasma are studied through these plasma parameters. These will be provided as reference data for the numerical study[44] and other diagnostic systems[43, 62] under development for an X-pinch study at Seoul National University. Moreover, it is also used to characterize SNU X-pinch as a point x-ray source, as shown in Table 5.1. Consequently, fast time-resolved x-ray diagnostics developed in this study will play an important role as fundamental diagnostics.

The experimental results obtained in Chapter 4 show that the generation of the long electron beam is an important process in the slow X-pinch. The long electron beam is also the main source of HXR. In the case of the 50 kV and 55 kV, the energies of HXRs above 7 keV are 11.2 mJ and 32.9 mJ, respectively, which are sufficient for x-ray radiography[12]; 79.3% and 75.8% of HXRs are emitted by the second and third bursts, respectively. Thus, long electron beam-

generated x-rays can be utilized as a HXR source for x-ray radiography for targets requiring energetic x-rays such as biological samples.[13, 21] However, for utilizing SNU X-pinch as an SXR source, the electron beam generated x-rays have negative effects such as background emission, lowering s spatial resolution, and increasing the number of x-ray peaks.[6, 12] Therefore, to improve the SNU X-pinch as an SXR source, the second and third bursts should be weakened. In other words, x-rays caused by the electron beam occurring after the main x-ray peak should be suppressed. On the other hand, x-ray peaks by long electron beams do not occur in the insulated Cu wires X-pinch. The insulated Cu wires load mitigates the disadvantage of a slow X-pinch. Temporal resolution is improved due to a decrease in the number of x-ray peaks. Total x-ray emission time (channel 2) is still long, but x-ray emission time is significantly reduced when x-rays of more than 1.6 keV (channel 1, 5–10) are used, as shown in Fig. 4.18. Moreover, the insulated wires load reduces the HXR significantly, which is an advantage as an SXR source. As a result, the bare Cu wire load can be used as an HXR source, while the insulated Cu wire load is a better option as an SXR source for the slow X-pinch. In addition, the conversion efficiency by x-ray energy also varies depending on the thicknesses of the Cu wire load, as shown in Table 5.1; a proper wire load can be selected according to the required x-ray energy. Therefore, these results allow SNU X-pinch to be utilized in various applications.

Table 5.1 Conversion efficiencies from a total input energy to x-ray energy with different energy ranges.

X-ray energy	25 μm (50 kV)	25 μm (55 kV)	30 μm	40 μm	25 + 2 μm
> 0.9 keV	4.05.E-04	4.00.E-04	3.85.E-04	1.35.E-04	5.83.E-04
> 1.6 keV	9.00.E-05	1.25.E-04	9.67.E-05	2.70.E-05	1.18.E-04
> 7.0 keV	7.40.E-06	2.10.E-05	1.49.E-05	3.52.E-09	9.75.E-07

5.2. Future work

As the next step of this study, we plan to research long electron beam generation and post-pinch dynamics. At Seoul National University, several diagnostics are being developed for the SNU X-pinch, and these additional diagnostics will be used for future work. The schematic view of the diagnostics configuration is shown in Fig. 5.1. First, there are additional filtered XRDs to supplement the x-ray diagnostic system developed in this study. These XRDs are collimated along the axis to measure the time evolution of HXR at a particular location. Locations, where HXR is emitted with time will be confirmed by comparing x-ray signals measured by the collimated XRDs and the filtered AXUV diode array. The second is an x-ray imaging device using a microchannel plate (MCP) and an intensified charge-coupled device (ICCD). The x-ray imaging device obtains an x-ray image for a short time. This will measure a spatial distribution of x-rays in an X-pinch load. The third is Schlieren and interferometer using 532 nm pulsed laser. The spatial distribution of the X-pinch plasma will be measured by obtaining the optical image at the time of the late-time x-ray peak. Electron density can be measured using an interferometer; unfortunately, the electron density estimated in this study is beyond its measurable density range. Thus, optical voltage and current sensors for local field measurement will be installed near the X-pinch load to confirm the rapid increase in electron density.[62] The impedance of plasma will be calculated through the measurement of voltage and current on an

X-pinch load, and the rapid change in the plasma impedance will be confirmed. This will be cross-check data for X-pinch plasma dynamics identified from the estimated plasma parameters. We expect these diagnostics to provide important information for post-pinch process and electron beam generation research. Factors affecting the generation of electron beams can also be identified in connection with the insulated Cu wires X-pinch study. In conclusion, future work is expected to present new factors for optimization of slow X-pinch as a point x-ray source.

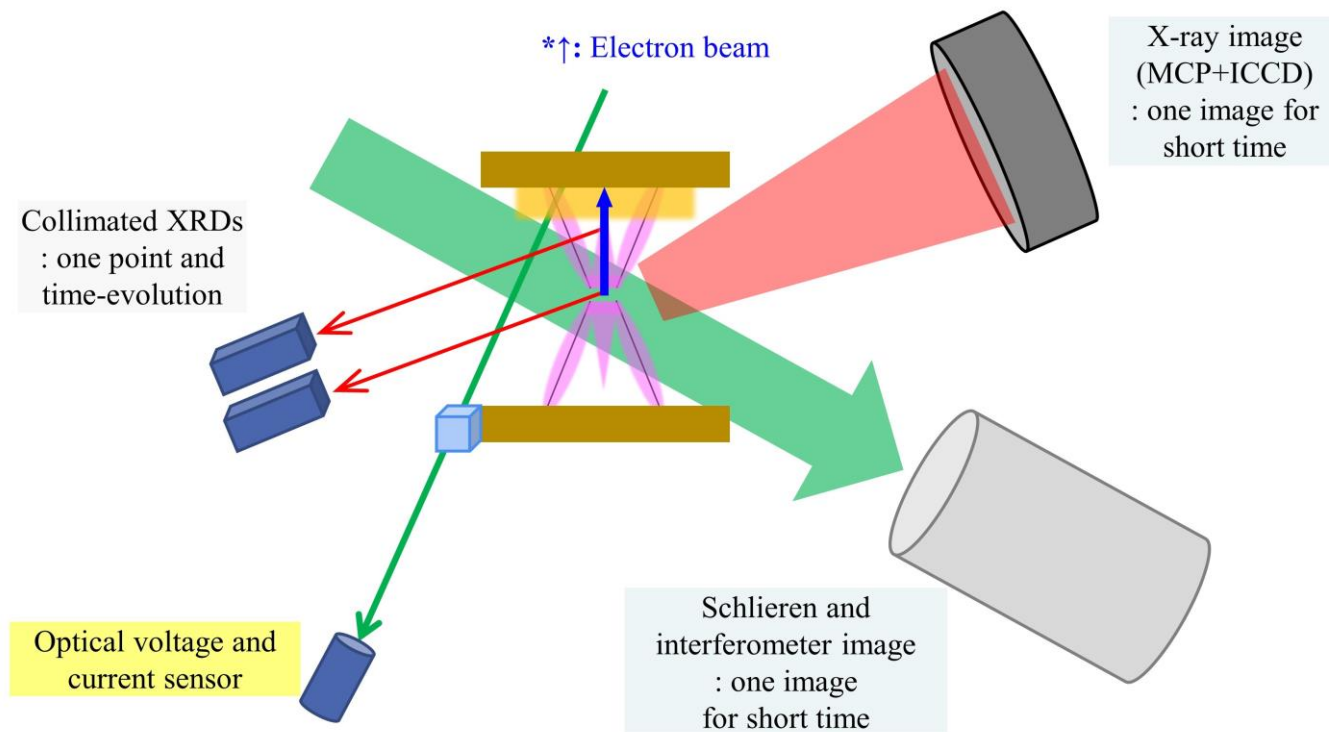


Figure 5.1 Schematic view of a configuration of diagnostics for future work

Bibliography

- [1] S. Pikuz, T. Shelkovenko, and D. Hammer, "X-pinch. Part I," *Plasma Physics Reports*, vol. 41, no. 4, pp. 291–342, 2015.
- [2] S. Pikuz, T. Shelkovenko, D. Sinars, D. Hammer, S. Lebedev, S. Bland, Y. Skobelev, J. Abdallah, C. Fontes, and H. Zhang, "Spatial, temporal, and spectral characteristics of an X pinch," *Journal of Quantitative Spectroscopy and Radiative Transfer*, vol. 71, no. 2–6, pp. 581–594, 2001.
- [3] F. Cochran and J. Davis, "Evolution of an X-pinch plasma," *Physics of Fluids B: Plasma Physics*, vol. 2, no. 6, pp. 1238–1246, 1990.
- [4] L. E. Aranchuk, J. Larour, and A. S. Chuvatin, "Experimental study of X-pinch in a submicrosecond regime," *IEEE transactions on plasma science*, vol. 33, no. 2, pp. 990–996, 2005.
- [5] G. Collins IV, M. Valdivia, S. Hansen, F. Conti, L. Carlson, D. Hammer, A. Elshafiey, J. Narkis, and F. Beg, "Direct comparison of wire, foil, and hybrid X-pinch on a 200 kA, 150 ns current driver," *Journal of Applied Physics*, vol. 129, no. 7, p. 073301, 2021.
- [6] T. Shelkovenko, S. Pikuz, A. Mingaleev, A. Agafonov, V. Romanova, A. Ter-Oganes'yan, S. Tkachenko, I. Blesener, M. Mitchell, and K. Chandler, "Accelerated electrons and hard X-ray emission from X-pinch," *Plasma physics reports*, vol. 34, no. 9, pp. 754–770, 2008.
- [7] T. Shelkovenko, S. Pikuz, B. Song, K. Chandler, M. Mitchell, D. Hammer, G. Ivanenkov, A. Mingaleev, and V. Romanova, "Electron-beam-generated x rays from X pinches," *Physics of plasmas*, vol. 12, no. 3, p. 033102, 2005.
- [8] V. Kantsyrev, A. Safronova, V. Ivanov, D. Fedin, R. Mancini, A. Astanovitsky, B. LeGalloudec, S. Batie, D. Brown, and V. Nalajala, "Radiative properties of asymmetric and symmetric X-pinch with two and four wires recently produced on the UNR 1 MA Zebra generator," *Journal of Quantitative Spectroscopy and Radiative Transfer*, vol. 99, no. 1–3, pp. 349–362, 2006.
- [9] V. Kantsyrev, D. Fedin, A. Shlyaptseva, M. Mitchell, B. Song, S. Pikuz, T. Shelkovenko, K. Chandler, D. Hammer, and L. Maxson, "Studies of energetic electrons with space and time resolution in Mo and WX-pinch from measurements of x rays > 9 keV," *Review of scientific instruments*, vol. 75, no. 10,

- pp. 3708–3710, 2004.
- [10] V. Kantsyrev, D. Fedin, A. Shlyaptseva, S. Hansen, D. Chamberlain, and N. Ouart, "Energetic electron beam generation and anisotropy of hard x-ray emission from 0.9 to 1.0 MA high-ZX pinches," *Physics of Plasmas*, vol. 10, no. 6, pp. 2519–2526, 2003.
 - [11] A. Robledo, I. Mitchell, R. Aliaga–Rossel, J. Chittenden, A. Dangor, and M. Haines, "Time-resolved energy measurement of electron beams in fiber Z-pinch discharges," *Physics of Plasmas*, vol. 4, no. 2, pp. 490–492, 1997.
 - [12] T. Shelkovenko, S. Pikuz, and D. Hammer, "A review of projection radiography of plasma and biological objects in X-pinch radiation," *Plasma Physics Reports*, vol. 42, no. 3, pp. 226–268, 2016.
 - [13] B. M. Song, T. Shelkovenko, S. Pikuz, M. Mitchell, K. Chandler, and D. Hammer, "X pinch x-ray radiation above 8 keV for application to high-resolution radiography of biological specimens," *IEEE Transactions on Nuclear Science*, vol. 51, no. 5, pp. 2514–2519, 2004.
 - [14] T. Shelkovenko, S. Pikuz, I. Tilikin, M. Mitchell, S. Bland, and D. Hammer, "Evolution of X-pinch loads for pulsed power generators with current from 50 to 5000 kA," *Matter and Radiation at Extremes*, vol. 3, no. 6, pp. 267–277, 2018.
 - [15] G. Collins IV, M. Valdivia, T. Zick, R. Madden, M. Haines, and F. Beg, "Study of X-pinch dynamics using a low current (25 kA) and slower current (400 ns) pulse," *Physics of Plasmas*, vol. 20, no. 4, p. 042704, 2013.
 - [16] C. Christou, A. Dangor, and D. Hammer, "Characterization of wire X pinches driven by a microsecond-long capacitive discharge," *Journal of Applied Physics*, vol. 87, no. 12, pp. 8295–8303, 2000.
 - [17] S. C. Andola, J. Batra, A. C. Jaiswar, A. K. Saxena, and T. C. Kaushik, "Investigations on slow current driven X-pinch as soft X-ray source for radiographic applications," *High Energy Density Physics*, vol. 35, 2020, doi: 10.1016/j.hedp.2019.100732.
 - [18] R. Appartaim and B. Maakuu, "X-pinch x-ray sources driven by a 1 μ s capacitor discharge," *Physics of Plasmas*, vol. 15, no. 7, p. 072703, 2008.
 - [19] R. Appartaim, "X-rays from a microsecond X-pinch," *Journal of Applied Physics*, vol. 114, no. 8, p. 083304, 2013.
 - [20] G. Jaar and R. Appartaim, "Axial plasma jet characterization on a microsecond x-pinch," *Journal of Applied Physics*, vol. 123,

- no. 21, p. 213301, 2018.
- [21] C. Pavez, A. Sepúlveda, N. Cabrini, J. A. Pedreros, G. Avaria, P. I. S. Martín, and L. Soto, "Energetics X-Ray Burst Observation in the Collapse of an X-Pinch Conducted in a Small Capacitive Generator of Low Impedance," *IEEE Transactions on Nuclear Science*, vol. 46, no. 11, pp. 3829–3836, 2018.
 - [22] S. Pikuz, T. Shelkovenko, K. Chandler, M. Mitchell, D. Hammer, I. Y. Skobelev, A. Shlyaptseva, and S. Hansen, "X-ray spectroscopy for high energy-density X pinch density and temperature measurements," *Review of scientific instruments*, vol. 75, no. 10, pp. 3666–3671, 2004.
 - [23] D. Sinars, S. Pikuz, T. Shelkovenko, K. Chandler, D. Hammer, and J. Apruzese, "Time-resolved spectroscopy of Al, Ti, and Mo X pinch radiation using an X-ray streak camera," *Journal of Quantitative Spectroscopy and Radiative Transfer*, vol. 78, no. 1, pp. 61–83, 2003.
 - [24] A. Shlyaptseva, S. Hansen, V. Kantsyrev, D. Fedin, N. Ouart, K. Fournier, and U. Safronova, "Advanced spectroscopic analysis of 0.8–1.0-MA Mo x pinches and the influence of plasma electron beams on L-shell spectra of Mo ions," *Physical Review E*, vol. 67, no. 2, p. 026409, 2003.
 - [25] T. Shelkovenko, S. Pikuz, I. Tilikin, A. Elshafiey, and D. Hammer, "Time-resolved investigation of subnanosecond radiation from Al wire hybrid X pinches," *Physical Review E*, vol. 102, no. 6, p. 063208, 2020.
 - [26] T. Shelkovenko, S. Pikuz, D. Sinars, K. Chandler, and D. Hammer, "Time-resolved spectroscopic measurements of ~ 1 keV, dense, subnanosecond X-pinch plasma bright spots," *Physics of Plasmas*, vol. 9, no. 5, pp. 2165–2172, 2002.
 - [27] S. Pikuz, D. Sinars, T. Shelkovenko, K. Chandler, D. Hammer, G. Ivanenkov, W. Stepniewski, and I. Y. Skobelev, "High energy density Z-pinch plasma conditions with picosecond time resolution," *Physical review letters*, vol. 89, no. 3, p. 035003, 2002.
 - [28] D. Fehl, F. Biggs, G. A. Chandler, and W. A. Stygar, "Spectral resolution for a five-element, filtered, x-ray detector array using the method of Backus and Gilbert," *Review of Scientific Instruments*, vol. 71, no. 8, pp. 3072–3079, 2000.
 - [29] D. Fehl, W. Stygar, G. Chandler, M. Cuneo, and C. Ruiz, "X-ray flux from filtered arrays of detectors without unfolding," *Review of scientific instruments*, vol. 76, no. 10, p. 103504, 2005.

- [30] S. Tianming, Y. Jiamin, and Y. Rongqing, "Recover soft x-ray spectrum using virtual flat response channels with filtered x-ray diode array," *Review of Scientific Instruments*, vol. 83, no. 11, p. 113102, 2012.
- [31] C. Sorce, J. Schein, F. Weber, K. Widmann, K. Campbell, E. Dewald, R. Turner, O. Landen, K. Jacoby, and P. Torres, "Soft X-ray power diagnostic improvements at the Omega Laser Facility," *Review of Scientific Instruments*, vol. 77, no. 10, p. 10E518, 2006.
- [32] E. Dewald, K. Campbell, R. Turner, J. Holder, O. Landen, S. Glenzer, R. Kauffman, L. Suter, M. Landon, and M. Rhodes, "Dante soft x-ray power diagnostic for National Ignition Facility," *Review of Scientific Instruments*, vol. 75, no. 10, pp. 3759–3761, 2004.
- [33] J. Bourgade, B. Villette, J. Bocher, J. Boutin, S. Chiche, N. Dague, D. Gontier, J. Jadaud, B. Savale, and R. Wrobel, "DMX: An absolutely calibrated time-resolved broadband soft X-ray spectrometer designed for MJ class laser-produced plasmas," *Review of Scientific Instruments*, vol. 72, no. 1, pp. 1173–1182, 2001.
- [34] K. Campbell, F. Weber, E. Dewald, S. Glenzer, O. Landen, R. Turner, and P. Waide, "Omega Dante soft x-ray power diagnostic component calibration at the National Synchrotron Light Source," *Review of scientific instruments*, vol. 75, no. 10, pp. 3768–3771, 2004.
- [35] L. E. Aranchuk and J. Larour, "Absolute Spectral Radiation Measurements From 200–ns 200–kA X -Pinch in 10–eV–10–keV Range With 1–ns Resolution," *IEEE transactions on plasma science*, vol. 37, no. 4, pp. 575–579, 2009.
- [36] R. Zhang, H. Luo, X. Zou, H. Shi, X. Zhu, S. Zhao, X. Wang, S. Yap, and C. San Wong, "Energy spectrum measurement of X-ray radiation from a compact x-pinch device," *IEEE Transactions on Plasma Science*, vol. 42, no. 10, pp. 3143–3147, 2014.
- [37] Z. Li, X. Jiang, S. Liu, T. Huang, J. Zheng, J. Yang, S. Li, L. Guo, X. Zhao, and H. Du, "A novel flat-response x-ray detector in the photon energy range of 0.1–4 keV," *Review of Scientific Instruments*, vol. 81, no. 7, p. 073504, 2010.
- [38] G. Chandler, C. Deeney, M. Cuneo, D. Fehl, J. McGurn, R. Spielman, J. Torres, J. McKenney, J. Mills, and K. Struve, "Filtered x-ray diode diagnostics fielded on the Z accelerator for source power measurements," *Review of scientific instruments*, vol. 70, no. 1, pp. 561–565, 1999.

- [39] J. Li, X.-B. Huang, S.-Q. Zhang, L.-B. Yang, W.-P. Xie, and Y.-K. Pu, "Investigation of spectra unfolded for a filtered x-ray diode array with improved smoothness," *Review of Scientific Instruments*, vol. 80, no. 6, p. 063106, 2009.
- [40] H.-K. Chung, M. Chen, W. Morgan, Y. Ralchenko, and R. Lee, "FLYCHK: Generalized population kinetics and spectral model for rapid spectroscopic analysis for all elements," *High energy density physics*, vol. 1, no. 1, pp. 3–12, 2005.
- [41] N. Cabrini, C. Pavez, G. Avaria, P. San Martín, F. Veloso, B. Zúñiga, A. Sepúlveda, and L. Soto, "Wire array experiments in a low impedance and low current generator," in *Journal of Physics: Conference Series*, 2015, vol. 591, no. 1: IOP Publishing, p. 012026.
- [42] A. Sepúlveda, C. Pavez, J. Pedreros, G. Avaria, P. San Martín, and L. Soto, "Dynamic Characteristics of X-pinch Experiments Conducted in a Small Capacitive Generator: Refractive Optical Observations," in *Journal of Physics: Conference Series*, 2016, vol. 720, no. 1: IOP Publishing, p. 012037.
- [43] J. Ryu, S. Ham, J. Lee, J. Park, S. Park, Y. Choi, H. Woo, K. Lee, Y.-C. Ghim, and Y. Hwang, "A modular X-pinch device for versatile X-pinch experiments at Seoul National University," *Review of Scientific Instruments*, vol. 92, no. 5, p. 053533, 2021.
- [44] S.-M. Byun, Y.-S. Na, K.-J. Chung, D.-K. Kim, S. Lee, C. Lee, J. Lee, and J. Ryu, "Numerical study of plasma evolution X-pinch in two- and three-dimensional geometry using a MHD code, STHENO," *Journal of the Korean Physical Society*, vol. 79, no. 9, pp. 818–827, 2021.
- [45] T. Shelkovenko, S. Pikuz, I. Tilikin, S. Bland, D. Lall, N. Chaturvedi, and A. Georgakis, "X-pinch X-ray emission on a portable low-current, fast rise-time generator," *Journal of Applied Physics*, vol. 124, no. 8, p. 083303, 2018.
- [46] J. F. Seely, C. N. Boyer, G. E. Holland, and J. L. Weaver, "X-ray absolute calibration of the time response of a silicon photodiode," *Applied optics*, vol. 41, no. 25, pp. 5209–5217, 2002.
- [47] M. Cho, J. Sohn, H.-K. Chung, B. Cho, and S. Hahn, "Analysis on the FLYCHK opacity of X-pinch wire materials," *Journal of the Korean Physical Society*, vol. 78, no. 11, pp. 1072–1083, 2021.
- [48] K. Akli, M. Key, H. Chung, S. Hansen, R. Freeman, M. Chen, G. Gregori, S. Hatchett, D. Hey, and N. Izumi, "Temperature sensitivity of Cu K α imaging efficiency using a spherical

- Bragg reflecting crystal," *Physics of Plasmas*, vol. 14, no. 2, p. 023102, 2007.
- [49] C. Huntington, C. Kuranz, G. Malamud, R. Drake, H.-S. Park, and B. Maddox, "Spectral analysis of x-ray emission created by intense laser irradiation of copper materials," *Review of Scientific Instruments*, vol. 83, no. 10, p. 10E114, 2012.
 - [50] M. Šmíd, O. Renner, F. B. Rosmej, and D. Khaghani, "Investigation of x-ray emission induced by hot electrons in dense Cu plasmas," *Physica Scripta*, vol. 2014, no. T161, p. 014020, 2014.
 - [51] S. Hansen and A. Shlyaptseva, "Effects of the electron energy distribution function on modeled x-ray spectra," *Physical Review E*, vol. 70, no. 3, p. 036402, 2004.
 - [52] G. Ivanenkov, W. Stepniewski, and S. Y. Gus'kov, "MHD processes during the cascade development of the neck and hot spot in an X-pinch," *Plasma Physics Reports*, vol. 34, no. 8, pp. 619–638, 2008.
 - [53] S. Pikuz, T. Shelkovenko, and D. Hammer, "X-pinch. Part II," *Plasma physics reports*, vol. 41, no. 6, pp. 445–491, 2015.
 - [54] J. Wu, X. Li, M. Li, Y. Li, and A. Qiu, "Review of effects of dielectric coatings on electrical exploding wires and Z pinches," *Journal of Physics D: Applied Physics*, vol. 50, no. 40, p. 403002, 2017.
 - [55] D. Sinars, T. Shelkovenko, S. Pikuz, M. Hu, V. Romanova, K. Chandler, J. Greenly, D. Hammer, and B. Kusse, "The effect of insulating coatings on exploding wire plasma formation," *Physics of Plasmas*, vol. 7, no. 2, pp. 429–432, 2000.
 - [56] K. Wang, "Nanosecond electrical explosion of bare and dielectric coated tungsten wire in vacuum," *Physics of Plasmas*, vol. 24, no. 2, p. 022702, 2017.
 - [57] Y. Li, L. Sheng, J. Wu, X. Li, J. Zhao, M. Zhang, Y. Yuan, and B. Peng, "Influence of insulating coating on aluminum wire explosions," *Physics of Plasmas*, vol. 21, no. 10, p. 102513, 2014.
 - [58] Y. Shi, Z. Shi, K. Wang, Z. Wu, and S. Jia, "Factors affecting the exploding characteristics of tungsten wires with negative-polarity current," *Physics of Plasmas*, vol. 24, no. 1, p. 012706, 2017.
 - [59] M. Li, L. Sheng, L. Wang, Y. Li, C. Zhao, Y. Yuan, X. Zhang, M. Zhang, B. Peng, and J. Zhang, "The effects of insulating coatings and current prepulse on tungsten planar wire array Z-pinch," *Physics of Plasmas*, vol. 22, no. 12, p. 122710, 2015.

- [60] L. Sheng, B. Peng, Y. Li, Y. Yuan, M. Li, M. Zhang, C. Zhao, J. Zhao, and L. Wang, "Experimental study of surface insulated-standard hybrid tungsten planar wire array Z-pinches at "QiangGuang-I" facility," *Physics of Plasmas*, vol. 23, no. 1, p. 012704, 2016.
- [61] M. Wallace, B. Hammel, S. Haque, P. Neill, and R. Presura, "The energy distribution of the electron beams in z-pinches with different load geometries," *Physics of Plasmas*, vol. 25, no. 11, p. 113101, 2018.
- [62] S. Choi, D.-G. Lee, H. Woo, S. Hong, S. Ham, J. Ryu, K.-J. Chung, Y. Hwang, and Y.-c. Ghim, "Data analysis scheme for correcting general misalignments of an optics configuration for a voltage measurement system based on the Pockels electro-optic effect," *Review of Scientific Instruments*, vol. 92, no. 4, p. 043105, 2021.

Abstract in Korean

SNU X-pinch를 위한 초고속 X-선 진단계

함 승 기

에너지시스템공학부

서울대학교 대학원

X-핀치에서 생성되는 고에너지밀도 플라즈마의 특성 덕분에 X-핀치는 높은 시간 및 공간 분해능의 X-선원으로써 뛰어난 장점을 가진다. 기존의 X-핀치 연구에 따르면, X-핀치가 방출 시간이 짧고 강한 X-선 펄스를 방출하기 위해서는 그것의 전류 발생기가 1 kA/ns 이상의 전류 상승률을 충족해야 한다. 하지만 여러 연구들에서 1 kA/ns 미만의 전류 상승률을 가진 느린 X-핀치도 강한 X-선 펄스를 생성할 수 있다는 것을 확인했다. 느린 X-핀치는 비교적 작은 사이즈와 낮은 비용 그리고 간단한 구조의 커패시터 뱅크를 사용한다는 점에서 부피가 크고 비싼 전류 발생기를 사용하는 기존의 X-핀치에 비해 연구실 수준의 연 X-선원으로써 장점이 있다. 반면에 느린 X-핀치는 더 빈번한 다중 방출과 긴 X-선 방출 시간, 큰 지터라는 단점들을 가지고 있다. 이러한 단점들을 개선하기 위해서는 느린 X-핀치에서 방출되는 X-선 펄스들과 그것들을 방출하는 X-핀치 플라즈마의 상태에 대한 분석이 필요하다. 따라서 약 수십에서 수백 나노 초의 X-선 방출 시간과 큰 시간 지터를 가진 느린 X-핀치의 다중 방출을 분석하기에 적합한 Filtered absolute extreme ultraviolet (AXUV) 다이오드 어레이를 개발했다. 그리고 측정된 X-선 스펙트럼을 FLYCHK 코드를

활용하여 분석하여 구리 세션 X-핀치 플라즈마의 변수 추정을 시도하였다. 특히, 느린 X-핀치의 과정에서 다중 방출과 X-선 방출 시간의 증가에 기여하는 늦은 시간의 X-선 펄스에 대한 분석을 진행했다.

Filtered AXUV 다이오드 어레이는 1-10 keV의 에너지 영역에서 X-선 스펙트럼의 시간 변화를 측정할 수 있도록 설계되었다. 검출기로 사용된 AXUV-HS5은 0.7 나노 초의 빠른 상승 시간과 넓은 에너지 검출 영역, 그리고 높은 접근성이라는 장점을 가지고 있다. 우리는 가상 채널로부터 낮은 파장 분해능의 불연속 스펙트럼을 재구성하는 least-squares (LS) 방법을 사용했다. Geant4 전산 모사는 평탄한 가상 채널을 만들기 위한 적절한 필터 조합을 설계하기 위해 활용되었다. 또한, Geant4 전산 모사에서 형성된 스펙트럼의 재구성을 통해 가상 채널들의 성능 평가가 진행됐다. 결과적으로, filtered AXUV 다이오드 어레이는 10% 이내의 평균 오차로 X-선 스펙트럼을 재구성한다는 것을 확인하였다.

서로 다른 변수의 플라즈마들은 서로 다른 X-선 스펙트럼을 방출하기 때문에 그것들의 분석을 통해 플라즈마 변수를 계산 할 수 있다. 분석 과정에서 필요한 가상의 스펙트럼을 얻기 위해 우리는 FLYCHK 코드를 X-선 분광 분석 모델을 위한 도구로 활용했다. 다른 전자 온도와 전자밀도, 고속 전자 비율을 가진 구리 플라즈마 스펙트럼 FLYCHK 코드를 이용해 계산했다. 그리고 스펙트럼 분석을 통해 각 다른 구리 선 방사선들을 포함하여 각 변수에 따라 다르게 변화하는 세 개의 파장 영역을 설정했다. 측정한 스펙트럼과 계산된 가상 스펙트럼의 정량적인 비교를 위해 세 개의 파장 영역에서 두 개의 X-선 파워 비율들이 계산되었다.

25 μm 두께의 구리 세션 X-핀치 실험은 SNU X-핀치 장치에서

50 kV 와 55 kV의 두 충전 전압 경우에서 수행되었다. Filtered AXUV 다이오드 어레이로 측정된 X-선 신호들에서 세 가지 종류의 X-선 버스트들이 관찰되었고 이 세 가지 버스트들에 대한 플라즈마 변수 분석이 수행됐다. 첫번째 버스트는 기존의 X-핀치와 비슷한 X-선 방출 특성을 보였다. 핫 스팟에서 방출되는 열 방사선이 첫번째 버스트에서 나타났고 열 방사선으로부터 추정된 핫 스팟의 전자 밀도와 전자 온도는 각각 10^{23} cm^{-3} 과 1 keV 정도 였다. 충전 전압이 55 kV인 경우에는 짧은 전자 빔에 의한 X-선 방출이 관찰되었고, 이때 고속 전자 비율이 최대 20%까지 상승한다. 두번째와 세번째 버스트는 긴 전자빔과 낮은 온도의 플라즈마의 상호 작용에 의해 상대적으로 긴 시간 동안 방출된다. 두번째 버스트에서는 전자빔의 형성이 플라즈마의 전자 밀도의 상승을 동반하였고, 이 때 전자 밀도는 핫 스팟의 전자 밀도와 비슷한 수준까지 상승하였다. 반면, 세번째 버스트에서는 전자 밀도의 상승이 발생하지 않았고 전자 밀도가 두번째 세트의 경우 보다 매우 낮게 추정되었다. 추가적으로 더 두꺼운 구리 세션 X-핀치 실험들이 수행되었고 그 결과들을 비교했다. 와이어 두꺼워지면서 핫 스팟의 파라미터들과 긴 전자빔에 의한 X-선 버스트가 감소하고 핀칭 시점이 지연되었다. 그리고 40 μm 두께의 구리 세션 X-핀치에서는 단일 X-선 펄스가 방출됐다.

절연 세션 부하의 사용은 긴 전자빔에 의한 X-선 방출을 억제하였다. 절연 구리 세션 X-핀치는 강한 단일 X-선 펄스를 생성하였고 이 때, 핫 스팟의 전자 밀도와 전자 온도는 일반 구리 세션 X-핀치의 경우와 비슷하게 추정되었다. 그리고 X-선 다중 방출과 경 X-선의 방출이 감소하였다. 일반적인 구리 세션과 절연 구리 세션 X-핀치의 결과 비교를 통해, 긴 전자빔에 의한 X-선 버스트의 방출은 핫 스팟 형성보다는 핀치 시점과 연관되어 있을 것으로 예상했다. 또한, 본

연구의 실험 결과와 선행 연구들을 토대로 우리는 긴 전자빔에 의해 전자 밀도가 증가하는 것에 대한 가능성 있는 시나리오를 제시하였고 그 시나리오는 고에너지 전자빔들에 의한 추가적인 이온화와 전류 재연결을 포함한다.

본 연구를 통해, 긴 전자빔의 형성은 느린 X-핀치의 X-선 방출에서 중요한 역할을 한다는 것을 확인했고, 그렇기 때문에 그것의 역학에 대한 연구는 느린 X-핀치의 성능 개선에 중요한 단서를 제공할 것이다. 따라서 우리는 시준된 X-선 다이오드와 X-선 및 가시광 이미징 시스템, 가시광을 이용한 전압 및 전류 센서를 추가적인 연구를 위한 진단계로 제시하였다. 이 추가적인 진단계를 이용한 연구를 통해 느린 X-핀치의 최적화를 위한 새로운 요소를 제시할 수 있을 것으로 기대한다.

주요어 : 고에너지밀도 플라즈마, X-선원, 느린 X-핀치, 고시간분해 X-선 진단계, 플라즈마 변수 추정, 전자빔.

학 번 : 2016-21312